POLITECNICO
MILANO 1863

SCUOLA DI INGEGNERIA INDUSTRIALE
E DELL'INFORMAZIONE

Characterization of a DECTRIS EIGER2 X CdTe 1M-W detector for medical imaging

Tesi di Laurea Magistrale in
Nuclear Engineering - Ingegneria Nucleare

Author: **Camilla Giaccaglia**

Student ID: 945736
Advisor: Prof. Carlo Ettore Fiorini
Co-advisors: Dr. Luca Fardin
Academic Year: 2021-22

Abstract

In recent years, position- and energy- sensitive semiconductor detectors have proven very promising in various synchrotron applications, including high-energy physics, astronomy and medical imaging. Their success stems from the fact that they offer unique detector performances in terms of noise, dynamic range and readout speed. In 2019, the world leading developer and manufacturer of Hybrid Photon Counting (HPC) X-ray detectors, DECTRIS, has launched the EIGER2 X series for 4th generation synchrotron facilities. Their main applications include X-ray diffraction, X-ray scattering and spectroscopy. The ID17 beamline of the European Synchrotron Radiation Facility (ESRF), dedicated to biomedical research, purchased the EIGER2 X CdTe 1M-W for a different application: biomedical imaging, including Computed Tomography (CT) experiments and the K-Edge Subtraction (KES) technique. The goal of this thesis work is therefore to perform a detailed characterization of this cutting-edge technology for this new application.

In particular, the characterization will focus on the determination of the performances of the detector in terms of linearity, Modulation Transfer Function (MTF), Normalized Noise Power Spectrum (NNPS) and Detective Quantum Efficiency (DQE). The standard protocols to determine these quantities were adapted to the peculiarities of synchrotron radiation and of Cadmium-Telluride (CdTe) sensors. The stability of the detector at its startup and during a typical CT experiment was investigated. In this work an innovative fit model for the Edge Spread Function (ESF), developed by the Detector Group of the ESRF, was tested. It extends the typical sigmoid fitting models found in literature by considering the physical dimension of the pixel and the effect of fluorescence photons on the spatial distribution of the charge released by the photon-sensor interaction. This model has led to very promising results.

The results obtained provided an insight into the limitations of the detector in view of medical imaging applications. It was observed that it is advisable to operate at relatively low fluxes, on the order of 1M counts/pixel/s. At higher fluxes a degradation in NPS and DQE is observed. The global stability of the detector during prolonged irradiation is compatible with CT experiments while the local variability may however affect image quality and quantitative measurements, such as KES results.

Keywords: EIGER2 characterization; Hybrid Photon Counting Detector; Medical Imaging; Synchrotron Radiation

Abstract in lingua italiana

Negli ultimi anni, i rivelatori a semiconduttore sensibili alla posizione e all'energia si sono dimostrati molto promettenti in varie applicazioni di sincrotrone, tra cui la fisica delle alte energie, l'astronomia e l'imaging medico. Il loro successo deriva dal fatto che offrono prestazioni uniche in termini di rumore, range dinamico e velocità di lettura. Nel 2019, DECTRIS, lo sviluppatore e produttore leader mondiale di rivelatori di raggi X Hybrid Photon Counting (HPC) ha lanciato la serie EIGER2 X per i sincrotroni di quarta generazione. Le sue principali applicazioni includono la diffrazione e lo scattering dei raggi X e la spettroscopia. La beamline ID17 dell'European Synchrotron Radiation Facility (ESRF), dedicata alla ricerca biomedica, ha acquistato l'EIGER2 X CdTe 1M-W per un'applicazione diversa: l'imaging biomedico, includendo esperimenti di tomografia computerizzata (CT) e la tecnica di sottrazione del K-Edge (KES). L'obiettivo di questo lavoro di tesi è quindi quello di eseguire una caratterizzazione dettagliata di questa tecnologia all'avanguardia per questa nuova applicazione.

In particolare, la caratterizzazione si concentrerà sulla determinazione delle prestazioni del rivelatore in termini di linearità, Modulation Transfer Function (MTF), Normalized Noise Power Spectrum (NNPS) e Detective Quantum Efficiency (DQE). I protocolli standard per determinare queste quantità sono stati adattati alle peculiarità della radiazione di sincrotrone e dei sensori al Tellurio di Cadmio (CdTe). Si è inoltre studiata la stabilità del rivelatore al suo avvio e durante un tipico esperimento CT. In questo lavoro è stato testato un nuovo modello di fit all'avanguardia per la Edge Spread Function (ESF), sviluppato dal Detector Group dell'ESRF. Esso si estende oltre i tipici modelli di fit sigmoidali trovati in letteratura considerando la dimensione fisica del pixel e l'effetto dei fotoni di fluorescenza sulla distribuzione spaziale della carica rilasciata dall'interazione fotone-sensore. Questo modello ha portato a risultati molto promettenti.

I risultati ottenuti hanno fornito una visione dei limiti del rivelatore in vista delle applicazioni di imaging medico. È stato osservato che è consigliabile operare a flussi relativamente bassi, dell'ordine di 1M conteggi/pixel/s. A flussi più elevati si osserva una degradazione di NPS e DQE. La stabilità globale del rivelatore durante l'irradiazione prolungata è compatibile con gli esperimenti di CT, mentre la variabilità locale può comunque

influenzare la qualità dell'immagine e le misure quantitative, come i risultati di KES.

Parole chiave: Caratterizzazione EIGER2; Hybrid Photon Counting Detector; Imaging Medico; Radiazione di Sincrotrone

Contents

Introduction

Motivation for the study

ID17 is a beamline of the European Synchrotron Radiation Facility (ESRF) dedicated to biomedical research. It was built with the primary goal to develop clinical trials in human coronary angiography, which were conducted from 2000 to 2003. Its activities later on expanded to include cerebral computed tomography and a clinical trial to treat brain tumours with Synchrotron Stereotactic Radiation Therapy (SSRT). Its activities include nowadays biomedical imaging, radiation biology and a preclinical program in Microbeam Radiation Therapy (MRT), which can be run both in-vivo and in-vitro in two experimental end-stations. Imaging is mainly performed with monochromatic radiation in an end-station built about 150 m from the X-ray source: this distance is necessary to obtain a beam size compatible with a human patient, due to the small angular divergence of the synchrotron radiation. To comply with the rigid safety protocols connected to the SSRT clinical trials, the hardware and software of this section of the beamline had to be effectively frozen in 2017. In December 2018, the long shutdown of the synchrotron, which led to the ESRF's Extremely Brilliant Source (EBS) upgrade, began. As a result, the beamline is currently undergoing a program of upgrade of the instrumentation, to meet the most recent requirements in biomedical imaging applications.

The main detector used for coronary angiography was a high purity germanium detector, operated at liquid nitrogen temperature. It was a dual line detector, with two rows of 432 pixels of size 300 µm x 10 mm. After the end of the coronary angiography clinical trial, it was used for in-vivo functional lung imaging, in which a technique called K-Edge Subtraction imaging (KES) allowed to study lung ventilation in several disease models. In this technique two beams, with energy slightly above and below the K-edge of a contrast medium were detected and compared, to quantitatively determine and follow in time the concentration of the contrast medium, such as xenon flowing into the airways. The progressive obsolescence of the electronics driving the germanium detector and the need for higher spatial resolution, lead the ID17 team to purchase a new detector, the EIGER2 X 1M-W by Dectris (Dectris, Baden, Switzerland). It is a direct-conversion single photon

counting Cadmium-Telluride (CdTe) detector with 75 x 75 µm^2 pixel size. It can be operated at room temperature, reaching a maximum frame rate of 2 kHz, compatible with time resolved biomedical imaging. This detector will effectively replace the germanium detector in its imaging applications. The single photon counting technology, resulting in noise-free images, and its high detection efficiency up to 80 keV will open new applications in low-dose in-vivo computed tomography. The EIGER2 X detectors were recently developed for 4th generation synchrotron facilities, such as the ESRF. Their main applications include X-ray diffraction, X-ray scattering and spectroscopy. A detailed characterization of the EIGER2 X 1M-W for biomedical imaging is still missing and is of fundamental importance for the beamline before making this cutting-edge technology available to the user community of the ESRF. The goal of this thesis work is to characterize the detector for medical imaging applications. In particular, the characterization will focus on the determination of the performances of the detector in terms of linearity, Modulation Transfer Function (MTF), Normalized Noise Power Spectrum (NNPS) and Detective Quantum Efficiency (DQE) and on the determination of the detector stability at its startup and during a typical Computed Tomography (CT) experiment.

Outline of the thesis

The presentation of the thesis work is organised as follows:

- In **Chapter 1** the basic concepts of synchrotron radiation and the structures built to generate and exploit it are explained. Special attention is paid to the ESRF and the ID17 biomedical beamline, where the experimental research to develop this thesis was conducted.
- **Chapter 2** opens with the physics of semiconductor detectors, focusing in particular on signal formation, charge transport and the main factors leading to the degradation of the recorded counts and the energy spectrum. It then focuses on the technology of hybrid pixel detectors, illustrating their principle of operation. Finally, the EIGER2 X CdTe 1M-W detector, the subject of this characterisation, is presented in detail. Its general structure, in terms of sensor and ASIC readout, operating conditions and computing infrastructure are reported.
- **Chapter 3** is intended to be a theoretical discussion of the main concepts necessary for a complete understanding of the experimental measurements performed in this thesis work. In the first part of this chapter the fundamental concepts necessary to characterise an imaging detector in terms of its performance are provided. In particular, the concepts of linearity, MTF, NPS and DQE are explained. In the second

part of this chapter, the basic principles of CT and KES, the main applications for which the EIGER2 was purchased, are presented.

- In **Chapter 4** the experimental set-up and the methods exploited to perform the measurements related to the characterization of the EIGER2 detector are reported. The chapter has been divided into two main parts: the determination of the performances of the detector in terms of linearity, MTF, NNPS and DQE and the determination of the detector stability at its startup and during a typical CT experiment.
- **Chapter 5** presents the results obtained concerning the characterisation of the detector. It maintains the structure of the previous chapter on instrumentation and methods. Thus, the results relating to linearity, MTF, NNPS and DQE are initially presented. The results of the stability study of the detector at its startup and during a typical CT experiment are then reported.
- In **Chapter 6** the detailed discussion of the results is presented.
- In **Chapter 7** conclusions are drawn. In particular, the results of the thesis work are discussed in their entirety and general indications are given for possible further developments.

1 | Synchrotron radiation and ID17

Since their discovery in 1895 X-rays have played a crucial role in many different fields such as physics, chemistry and biology. The most commonly exploited X-ray sources are X-ray tubes, due to their simplicity, robustness and low cost. However, they are limited in terms of the intensity they can provide. An alternative way to generate X-ray radiation with improved properties are Synchrotron Radiation (SR) sources, able to provide tunable X-ray photon beams with increased intensity and beam quality.

In this chapter the fundamentals of SR and the facilities built to generate and exploit it are illustrated. Special attention is devoted to the ESRF and to the biomedical ID17 beamline, where the experimental research to develop this thesis work was carried out.

1.1. Synchrotron radiation

Whenever a relativistic charged particle, electron or positron, passes through a magnetic field, its path is bent and a sharply collimated radiation is emitted tangentially to the curved trajectory of the accelerated particles. Such electromagnetic waves are the so-called SR. The latter is emitted in a narrow cone with a natural opening angle of about $2/\gamma$ ($\gamma = 1/\sqrt{1 - {v_e}^2/c^2} = 1/\sqrt{1-\beta^2}$, where β is the ratio between the electron velocity v_e and the speed of light c). The beam geometry is shown in Figure 1.1.

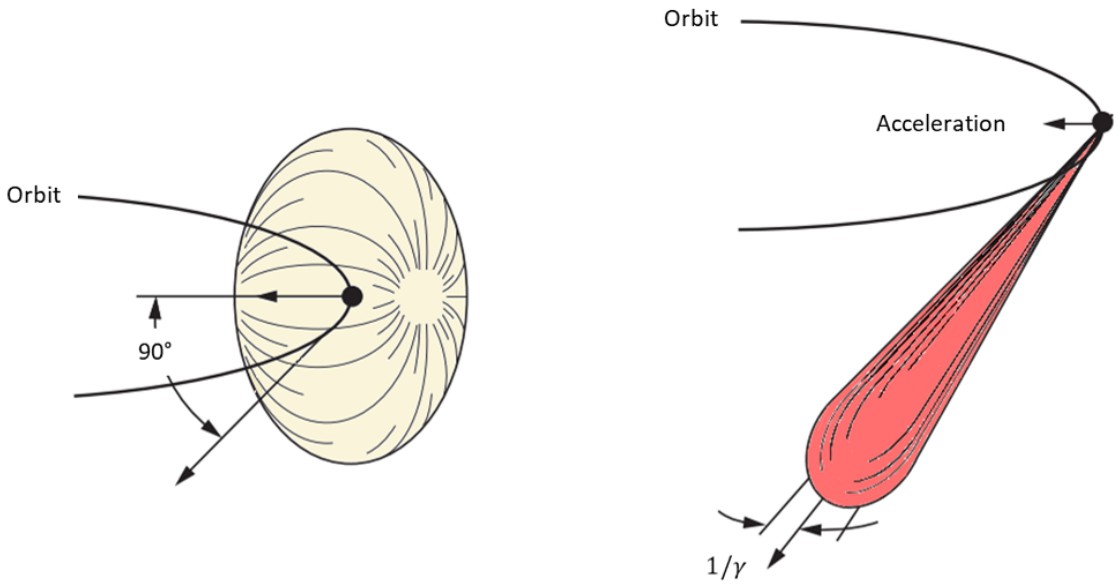

(a) (b)

Figure 1.1: Conceptual representation of the radiation pattern from a charged particle undergoing circular acceleration at (a) subrelativistic and (b) relativistic velocities. Modified from [1].

This phenomenon was first observed in 1947 at the 70 MeV General Electric electron synchrotron [2]. Although it was initially considered pure energy loss in particle accelerators, its unique characteristics in terms of broad spectrum, brightness, coherence and polarization were soon understood, leading in the 80's to the construction of fully dedicated SR facilities all around the world.

Synchrotron radiation facilities consist of three main sections: an electron source, a LINear ACcelerator (LINAC), a circular accelerator (booster) and a storage ring. The general layout is represented in Figure 1.2.

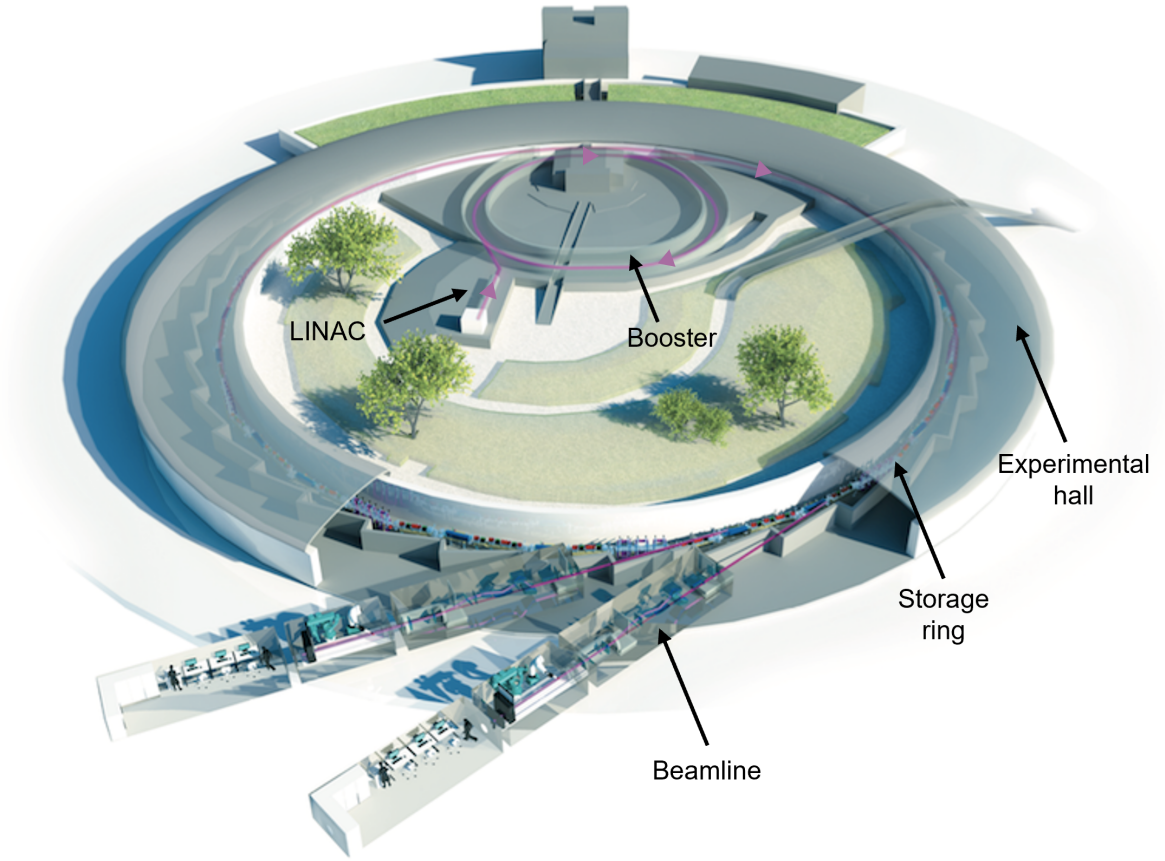

Figure 1.2: Scheme of a synchrotron radiation facility. Electrons are injected and accelerated into the LINAC until they reach the energy of the order of 100-200 MeV. Once they are accelerated in the booster, up to the storage ring energy, they are injected in the storage ring, where dedicated bending magnets and insertion devices are utilized to produce synchrotron radiation. The beamlines and the experimental hall are highlighted. Adapted from [3].

Electrons are produced in bunches by means of an electron gun by heating a cathode. They are first accelerated in the LINAC until they reach an energy of the order of 100-200 MeV and subsequently transmitted into the booster where their energy is "ramped" to the final one, typically between 1.5 and 8 GeV. From the booster the electrons are injected into the storage ring, where they run in ultra-high vacuum (less than 10^{-8} mbar) to minimize the probability of collision with residual gas. In the storage ring is installed a periodic sequence of magnets, called *magnetic lattice*, which forces the electrons into a closed orbit. The first component of a magnetic lattice is a dipole, called *bending magnet*, which bends the electron beam forcing it into a circular orbit. However, since electrons have different positions inside the beam, they follow different circular orbits. In order to focus the beam, in the straight sections in between the bending magnets, quadrupoles

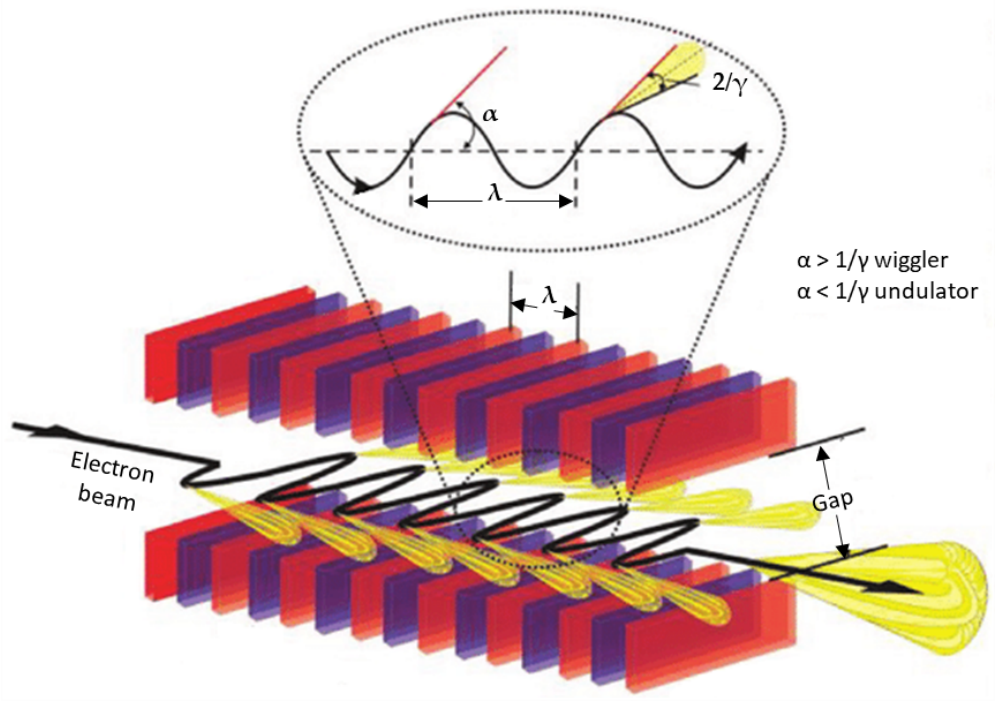

Figure 1.3: Layout of radiation beam emission from permanent multipole wiggler/undulator insertion devices. The brightness spectrum of the emitted radiation is shown. Modified from [4].

and sextupoles are inserted. Magnetic quadrupoles provide a focusing action that keep the electron beam transverse dimensions small, while sextupoles are used to compensate for chromatic aberrations produced by quadrupoles.

SR is emitted when electrons are radially accelerated by bending magnets and Insertion Devices (IDs). The latter, which are installed in straight sections of the storage ring, can be either wigglers and undulators (see Figure 1.3). They consist of a sequence of dipole magnets of alternate polarity in which the electrons are forced to oscillate around a straight-line trajectory.

- In the case of **wigglers**, the electron oscillations are wider than the natural opening angle of the radiation and hence the beam emitted by the device is the incoherent sum of the radiation cones produced by the single oscillations. The X-ray spectrum exhibits a continuous distribution.
- Instead, in **undulators** the beams emitted by poles can interfere coherently, producing a narrow beam. This leads to a spectrum with strong peaks at a specific energy and its harmonics.

Due to the relativistic speed of the electrons, the radiation is emitted with vertical angular

divergence. The horizontal divergence is larger and depends on the length of the arc described. The resulting radiation is described as *fan beam*.
As a result of the emission of electromagnetic radiation, the electron energy in the storage ring decreases at each revolution. With the purpose of replenish electrons energy losses, radiofrequency cavities, accelerators based on an oscillating electric field, are installed.

The radiation emitted by the bending magnets or by the IDs is channeled to the experimental stations in-vacuum *beamlines*. As there are several beam channels throughout the storage ring, a large number of experiments can be performed simultaneously. Each beamline performs a specific research exploiting the X-ray beam and usually they are composed of an optical hutch(es), an experimental hutch(es) and control room(s).

1.2. The European Synchrotron Radiation Facility (ESRF)

The European Synchrotron Radiation Facility is a joint research facility located in Grenoble (France). Built by the collaboration of 11 countries, it became operational in 1994, reaching 22 European and extra-European funding state members. At the end of 2018, the ESRF underwent a 20-month shutdown to replace the storage ring with an improved X-ray source known as ESRF-EBS, thus becoming the first high-energy 4th generation machine [5]. In particular, the ESRF consists of: i) a 16 meter long LINAC to accelerate the electron beam up to 200 MeV, ii) a 300 meters of circumference booster to accelerate electron bunches up to 6 GeV and a iii) 844 meters circumference storage ring, consisting of 32 magnetic cells, where electron bunches circulate giving rise to a current up to 200 mA (Figure 1.4).

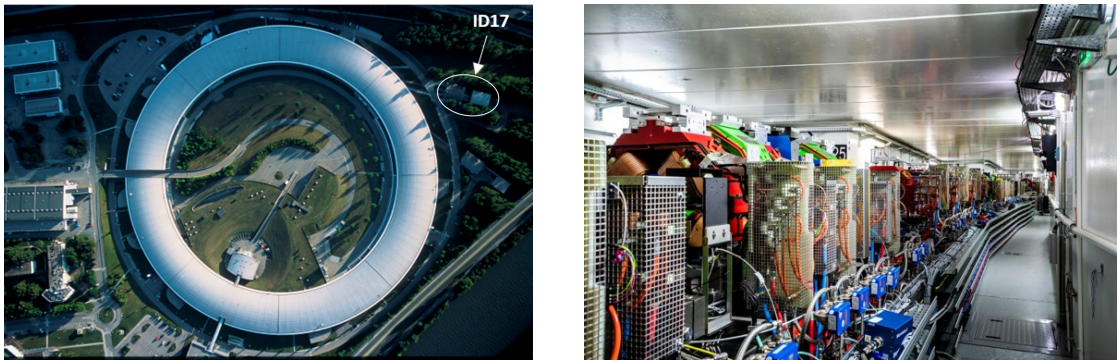

(a) (b)

Figure 1.4: Top view of the ESRF-EBS building with the ID17 beamline highlighted (a), and a section of the magnetic lattice of the storage ring (b). Modified from [6, 7].

In 2016, the ESRF introduced the top-up mode, which is a new way of injecting periodically electrons into the storage ring. This is necessary since the emission of radiation and the interactions between electrons in a single bunch causes a decrease of the storage ring current. The new mode sees the accelerators refilled with electrons every 30/60 minutes rather than every 4 to 12 hours as previously. This leads to a much higher integrated current over a 24-hour period, providing users with improved beam stability, low vertical emittance in all filling modes [8], and near-constant beam current (approximately 5% variation in one hour).

Forty-two beamlines are developed all along the storage ring with the aim of advancing research in various fields such as physics, engineering, chemistry, crystallography, earth science, biology, material and surface science. The experimental research necessary to develop this thesis was carried out at the ID17 biomedical beamline.
In the following section, a general description of the ID17 beamline is provided.

1.3. The ID17 beamline

The ID17 beamline is dedicated to preclinical and clinical biomedical research, in particular in the two fields of imaging and radiation therapy. Several studies have been carried out over time: neuroimaging [9], lung imaging [10], imaging of cartilage [11] and preclinical investigation of radiation therapy with micro-beams [12].

In order to get an overview of the beamline, a brief description of both experimental stations constituting the beamline will be made first. The focus will then be on the radiation source exploited in this beamline and on the second experimental station, where the experimental measurements necessary for the development of the thesis were carried out.

1.3.1. Beamline design

ID17 is one of the longest beamlines at the ESRF and it is constituted of two medical research stations: one experimental station is located in the experimental hall, while the other is external to the storage ring building, in the so-called *satellite building*. Each station is characterized by an optical hutch, an experimental hutch and a control room. The general layout of the whole beamline is shown in Figure 1.5.
In particular, it consists of:

- A **first Optics Hutch** (OH1), located just after the front-end, contains all the optical instrumentation for the spectral and geometrical definition of the X-ray

beam.

- A **first Experimental Hutch** (EH1, or MRT hutch), located at about 40 m from the source, exploits a polychromatic beam. It is mainly devoted to applications requiring a high flux, such as MRT experiments, as described in detail in the works of Bräuer-Krisch et al. [13] and Martínez-Rovira [14] and imaging experiments with polychromatic beam [15]. A first control room is located besides this experimental hutch, which hosts computers to control the instrumentation and run the scans.
- A long ultra-high vacuum tube in a 100 m **tunnel** connects the MRT hutch with the satellite building located outside the storage ring hall. The tube is shielded with 20 mm of lead, and it is enclosed in a concrete tunnel to avoid any radiation hazard.
- A **second Optics Hutch** (OH2), where a set of slits, absorbers, beam monitors and the main monochromators (see Section 1.3.3) are installed. Hence, the beam is opportunely monochromatized and its intensity and transverse dimensions are tuned in order to achieve the desired beam properties for imaging.
- A **second experimental Hutch** (EH2), located at about 150 meters from the source, exploits monochromatic X-rays, mainly for imaging data acquisition. A second control room is located close to this hutch.

The two experimental hutches can not be used simultaneously: when the second experimental hutch is used, a vacuum tube is installed in the first experimental hutch, so that radiation propagates from the source to the second optics hutch in the satellite building.

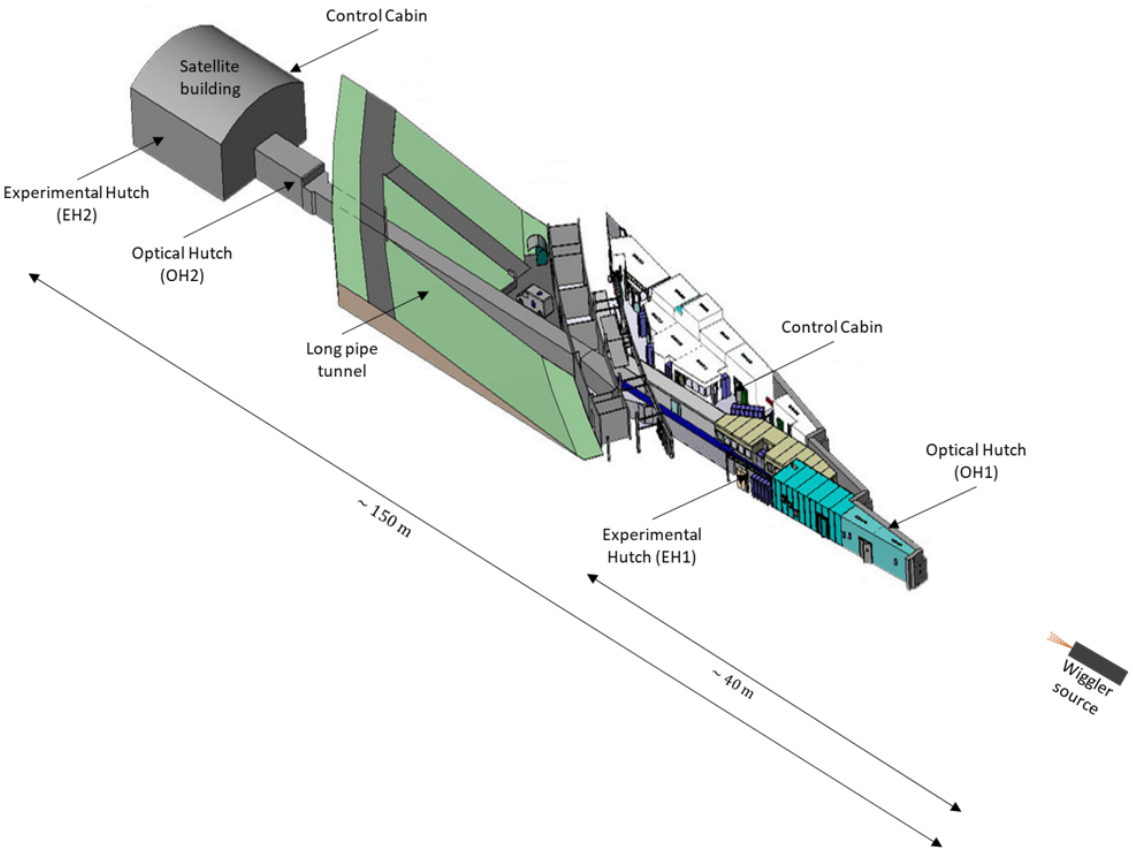

Figure 1.5: Layout of the ID17 biomedical beamline. It is constituted of two medical research stations connected by a long vacuum tube inside a tunnel. An experimental station for radiotherapy is located in the experimental hall at about 40 m from the wiggler source. Imaging experiments take place in the satellite building, located around 150 m from the source point. Each experimental station is constituted of an optical hutch, an experimental hutch and a control cabin. Representation not in scale. Modified from [16].

1.3.2. X-ray source

The ID17 source consists of two multipole wigglers, with adjustable vertical gap between the magnets. The first wiggler (w150), characterized by 21 poles and a magnetic field period of 15 cm, can reach a maximum magnetic field of 1.6 T and a maximum critical energy of 38.6 keV. The maximum critical energy of the radiation emitted by a dipole is defined as the energy which divides the power spectrum into two equal parts. A second wiggler (w125) is exploited in those experiments where higher fluxes are needed. It is a 22-pole wiggler with a period of 12.5 cm and a maximum magnetic field of 1.8 T at a gap of 11 mm. In particular, for imaging purposes, only the first wiggler is used.

1.3.3. Second experimental station

As already explained, the second experimental station, located at the satellite building, is divided in optical hutch and experimental hutch.
The optical hutch is located at the end of the 100 m vacuum tube and a schematic representation of its layout is provided in Figure 1.6.

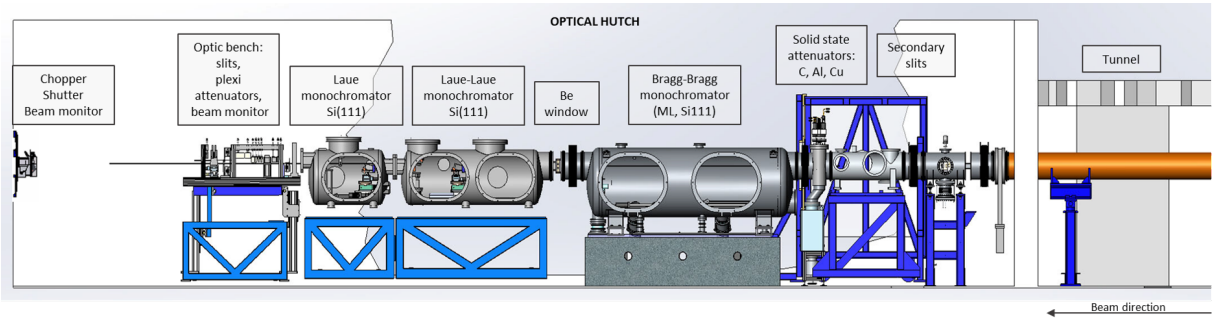

Figure 1.6: Layout of the the optical hutch of the satellite station of ID17. An ultra-high vacuum tube inside a tunnel connects this hutch with the first experimental station located inside the storage ring building. The main components to opportunely tune, define and control the beam are shown. The various monochromators exploited for imaging experiments are also illustrated.

The first section is under vacuum and contains a set of slits, called *secondary slits*, a set of solid state attenuators, a double multilayer crystal and a double Si(111) flat crystal used in Bragg geometry. The secondary slits are used to define the transversal dimension of the beam and consequently the thermal load on the monochromators. Instead, the attenuators are used to opportunely tune the beam intensity. The thicknesses of the main attenuators exploited for imaging experiments, Aluminum (Al), Carbon (C) and Copper (Cu), are reported in Table 1.1.

	Thickness [mm]
Al	0.5, 1.0, 2.0
C	0.8, 4.0
Cu	1.0

Table 1.1: Main movable attenuators available at OH2 at the ID17 beamline. A more complete list can be retrieved from Mittone et al. work [15].

Then, a 500 µm thick beryllium window separates this first section from the monochro-

mator vessel, which instead is under oxygen free helium flow at atmospheric pressure. There are two monochromators available working in that condition: (i) a double bent-Laue Si(111) monochromator and (ii) a double Si(111) flat crystal used in Bragg geometry. The one used for the acquisition of the experimental results in this thesis is the double bent-Laue crystal, which is also used in all the tomographic experiments. It is a fixed-exit monochromator which uses two water-cooled bent Si crystals in Laue geometry producing a monochromatic beam parallel to the incident polychromatic one with a vertical offset of 40 mm. It consists of two Si(111) cylindrically bent asymmetric crystals with an asymmetry angle of 15°. The beam is diffracted by the central part of the crystals which is 1 mm thick, 150 mm wide and 12 mm high. The range of energies that can be selected with this monochromator is 25-150 keV, with a bandwidth of 0.1%.
After the monochromators, a set of Plexiglas attenuators is available to adjust the beam intensity without changing the monochromator settings or the wiggler parameters. The Plexiglas thickness can be varied from 0.5 up to 32 cm by steps of 0.5 cm, which provides for example attenuation factors from 5×10^{-1} to 3×10^{-5} at 33 keV [17].

The X-ray beam can be monitored through the use of ion chambers, which are made of a single chamber filled with argon at atmospheric pressure.
Moreover, the optics hutch contains a system of beam shutters which allows radiation to be stopped in the second experimental hutch, avoiding unnecessary exposure of the cameras and biological samples. The shutters are made of sufficiently thick tungsten blades, which are kept out of the beam with springs compressed by electromagnets during experiments. If a problem is detected, they can be closed in about 10 ms by switching off the electro-magnet power supply.

The experimental hutch of this second station contains the sample stage and the detectors utilized for imaging experiments. A simplified representation of this hutch is reported in Figure 1.7. Thanks to the X-ray beam divergence and the long distance from the source the beam can reach approximately 250×10 mm^2 (horizontal $\times$ vertical). However, the horizontal size of the beam is reduced in practice due to the optical constrains (i.e. monochromators and other optics) to about 150×10 mm^2.

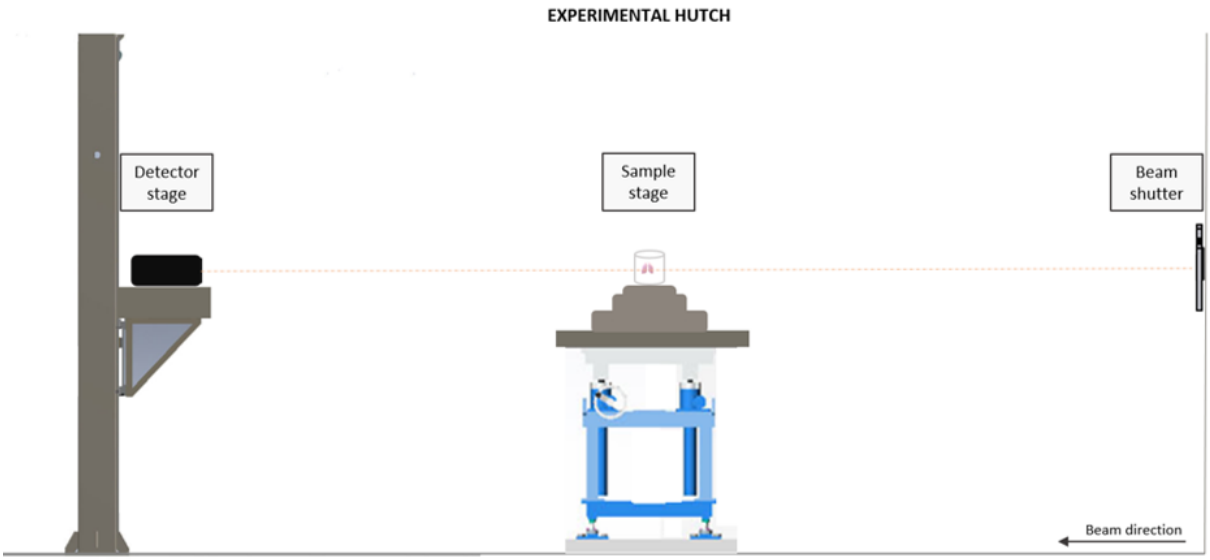

Figure 1.7: Layout of the experimental hutch of the second station of the ID17 beamline. At the entrance of the hutch a fast shutter is located. The sample stage and the detector stage are shown.

2 | Semiconductor pixel detectors

Semiconductor pixel detectors are commonly used for detection of radiation in particles physics and imaging applications [18], especially in the biomedical field [19]. To date there are two approaches for manufacturing pixel detectors, the hybrid and the monolithic approach. Hybrid Pixel Detectors (HPDs) are characterized by the fabrication of the sensor matrix and the readout electronics on two different substrates and then mated, typically by bump bonding. On the other hand, in the monolithic pixel detectors the detection sensor and the readout electronics are integrated in the same technological process. For further details, refer to Rossi et al. work [20].

This chapter first reviews the physics of semiconductor detectors and then, with regard to the development of this thesis work, delves into the main characteristics of HPDs, with a particular focus for photon counting systems.

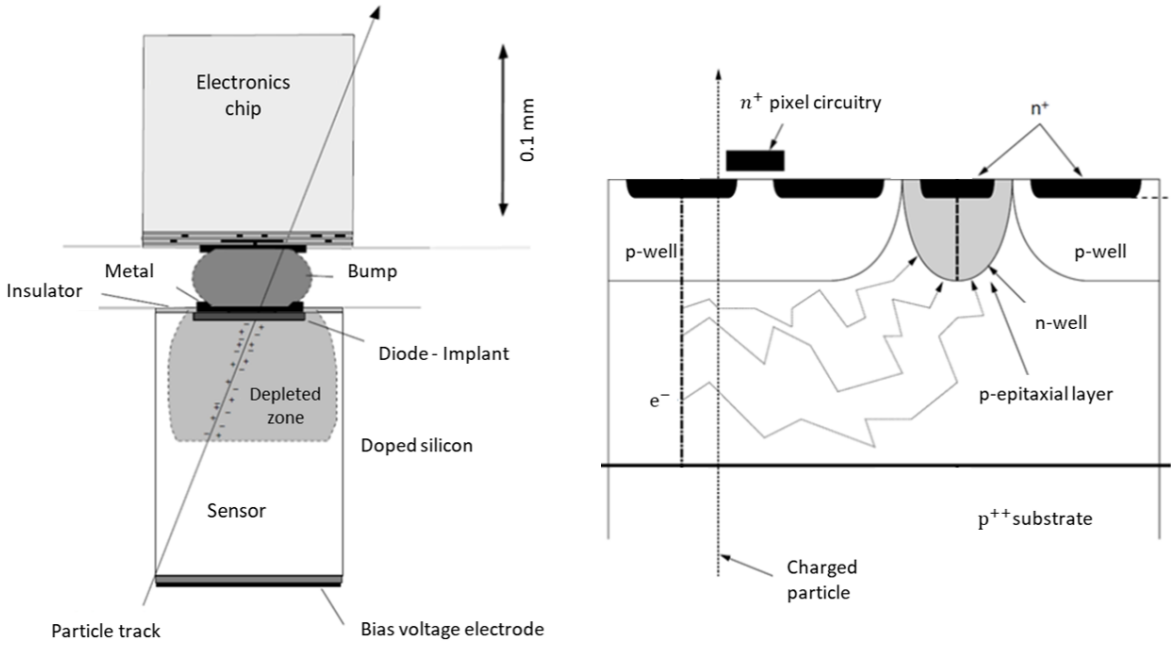

Figure 2.1: Typical structure of hybrid pixel detector (a), and monolithic pixel detector (b). Modified from [20].

2.1. Semiconductor detector physics

2.1.1. Signal source

In a semiconductor there are two main mechanisms of charge generation: thermal excitation and charge particle interaction. Thermal generation is often a parasitic phenomenon that leads to the formation of a leakage current in detectors, resulting in signal degradation. Therefore, for materials with a small energy gap, such as Germanium (Ge), it is necessary to operate at low temperatures to limit this unwanted process. In radiation detectors, the signal comes from the ionization by the impinging particle. In case of X-rays, many electron-hole pairs are generated in a small spatial region around the interaction point. The number of electron-hole pairs (N), created by the photoelectric absorption of an X-ray with energy E_{X-ray}, can be estimated by:

$$N = E_{X-ray}/\epsilon \tag{2.1}$$

where ϵ is the average energy required to create an electron-hole pair. The energy of the incident X-ray is not all used for the creation of electron-hole pairs but part of it is used for the creation of phonons, hence the difference in values observed between the energy band gap and ϵ. The energy gap and the pair creation energy for different semiconductors can be found in Table 2.1.
Electron-hole pairs generation is a stochastic process. If the majority of the energy went into the creation of phonons, it can be shown that the number of electron-hole pairs approaches a Poisson distribution, with a variance equal to the mean number of pairs. In general the distribution departs from the Poissonian one and to quantify it the Fano factor (F) has been introduced [21]:

$$F \equiv \sigma_N^2/\bar{N} \tag{2.2}$$

where $\bar{N}$ is the mean number of electron-hole pairs and σ_N^2 is the variance. $F<1$ means that the creation of each electron-hole pair is not an independent event.

	Si	Ge	GaAs	CdTe
Atomic number Z	14	32	31/33	48/52
Energy band gap [eV]	1.12	0.67	1.43	1.44
Pair creation energy ϵ [eV]	3.6	2.96	4.2	4.43
Hole mobility μ_p [$cm^2V^{-1}s^{-1}$]	450	1900	400	100
Electron mobility μ_n [$cm^2V^{-1}s^{-1}$]	1350	3900	8000	1100
Hole lifetime τ_p [s]	2.22×10^{-3}	5.26×10^{-4}	$> 10^{-8}$	2.00×10^{-6}
Electron lifetime τ_n [s]	7.41×10^{-4}	2.56×10^{-4}	$> 10^{-8}$	2.73×10^{-6}

Table 2.1: Properties of different semiconductors (Silicon (Si), Germanium (Ge), Gallium-Arsenide (GaAS) and Cadmium-Telluride (CdTe) at a temperature of 300 K [22].

2.1.2. Charge transport

Free charges generated by incident radiation are transported in the material through two mechanisms: *diffusion* and *drift*. The diffusion motion arises in the presence of an inhomogeneous gradient distribution of free charge carriers (electrons and holes). Since the carriers move mainly from the region with the highest concentration to the one with the lowest one, the diffusion current has a direction opposite to the concentration gradient. The diffusion current is given for electrons (n) and holes (p) by:

$$J_{diff} = \begin{cases} qD_n\nabla n, & D_n = \mu_n(\frac{kT}{q}) \\ -qD_p\nabla p, & D_p = \mu_p(\frac{kT}{q}) \end{cases} \tag{2.3}$$

where D is the diffusion coefficient and ∇ the density gradient. K, T and q are respectively the Boltzmann constant (1.38×10^{-23} J K^{-1}), the absolute temperature and the fundamental charge (1.6×10^{-19} C). μ is the carrier mobility and the values for different materials are reported in Table 2.1.

On the other hand, the drift current is generated by an applied electric field, E, for example by a reverse biasing. In this case the charge motion is governed by the mobility μ of the charge carrier. The drift velocity for electrons and holes ($v_{n,p}$) is defined as:

$$v_{n,p} = \mu_{n,p}E. \tag{2.4}$$

It includes the effects of scattering and trapping of the carrier but the whole motion results

in a random-walk process which has the appearance of a drift at constant velocity in the electric field direction. Drift velocity grows linearly with the electric field but at a certain point saturation of the carrier velocity is reached. From the drift current we define the drift current density for electrons and holes respectively as:

$$J_{drift} = \begin{cases} -qnv_n \\ qpv_p \end{cases} \tag{2.5}$$

where n and p are the electron and hole free densities.
Therefore, the total current in the semiconductor is given by the sum of the diffusion and drift currents for each type of carrier:

$$J_{tot} = J_n + J_p = (J_{diff} + J_{drift})_n + (J_{diff} + J_{drift})_p. \tag{2.6}$$

An additional parameter significant in the description of charge transport is the *carrier lifetime* τ, that is the survival time of a carrier before it undergoes recombination (annihilation of electron-hole pairs) or trapping. The average distance traveled in the material along the direction of the electric field before trapping is defined by the product of mobility-lifetime and electric field:

$$\lambda = v\tau = \mu\tau E. \tag{2.7}$$

Impurities in a semiconductor, which lead to the creation of new energy levels near the center of the band gap, act as traps for carriers for a certain period of time. We can distinguish between deep and shallow impurities depending on whether they are created in deep states or not. If the trapping period is sufficiently long, the trapped carriers cannot contribute to the measured signal by the detector. Almost all the carriers will be able to contribute to the signal before recombination if the collection time of carriers is lower than the average lifetime. Hence a low collection time is a desirable parameter for a good radiation detector. Structural defects within the crystal may also contribute to charge trapping.

2.1.3. Signal formation

Typical radiation detectors generally include two electrodes at fixed potential. Under an electric field, the electron-hole pairs, generated from direct ionization by a traversing particle, are separated and drift towards the corresponding electrodes where they are measured by the readout electronics. The collection efficiency is therefore defined as the

ratio of the observed collected charge to the expected one. Total charge collection occurs when the carriers reach the electrodes, however charges can be trapped by deep levels in the band gap of the semiconductor (see Section 2.1.2). There are many approaches to find the formed charge distribution on the detector electrodes. One of the most exploited methods is the Ramo's theorem, which states that the amount of electric charge generated on the electrode is determined by the position of the drifting charges and the weighting potential, $\phi_w(x)$, of the electrode at that position. x indicates the coordinate along the drifting direction.
For a charge q drifting from the point x_1 to the point x_2, the electric charge induced on the electrode is given by:

$$Q = q[\phi_w(x_2) - \phi_w(x_2)]. \tag{2.8}$$

For a more detailed discussion please refer to the work of Spieler [22]. In the case of a pixel detector, the induced current no longer depends only on the distance travelled by the carriers, but also on the interaction point. By choosing a pixel of small dimensions compared to the detector thickness, the signal is almost entirely due to electron transport and the effects of hole trapping can be reduced with no loss in detection efficiency [23].

2.1.4. Limiting factors

When dealing with hybrid pixel detectors, various factors must be considered that lead to various degradations in both the recorded counts and the energy spectrum. In the following, the most relevant ones are presented, also in relation to the development of the thesis: pulse pileup, charge sharing, K-escape X-rays, Compton scattering, charge trapping and polarization.

Pulse pileup

Pulses produced by photon interactions are randomly spaced in time and this may lead to superimposition effects between pulses when counting rate are not low. This phenomenon, which is always present in a photon counting detector, goes under the name of pulse pileup and it is a function of the count rate and detector dead time. The latter is defined as the time after each detection event during which the system is not able to record another event. Pulse pileup leads to a loss of counts, also known as dead time losses, and a distortion in the pulse amplitude measurement. Detectors with longer dead times shows this effect at lower count rates. When dealing with high count rates, such as in CT and X-ray medical imaging, two types of pulse pileup are observed: *peak* and *tail* pulse pileup [24]. The pulse pileup originates when multiple pulses, generated by nearly coincident photons, are piled

up, leading to a single output pulse. On the other hand, the tail pulse pileup involves the superposition of pulses on the long-duration tail from a preceding pulse. Two models of dead time behavior of counting systems have come into common usage: *paralyzable* and *non-paralyzable* response. A comparison of the two models is represented in Figure 2.2. In a paralyzable detector an event happening during the dead time is not accounted in the total counts but it will restart the dead time. On the other hand, in a non-paralyzable system an event occurring during the dead time is ignored and have no effect in the measurement. To compensate for these effects in the most demanding imaging modalities in terms of incoming flux, algorithmic methods, based on the properties of the detectors, have been developed [25].

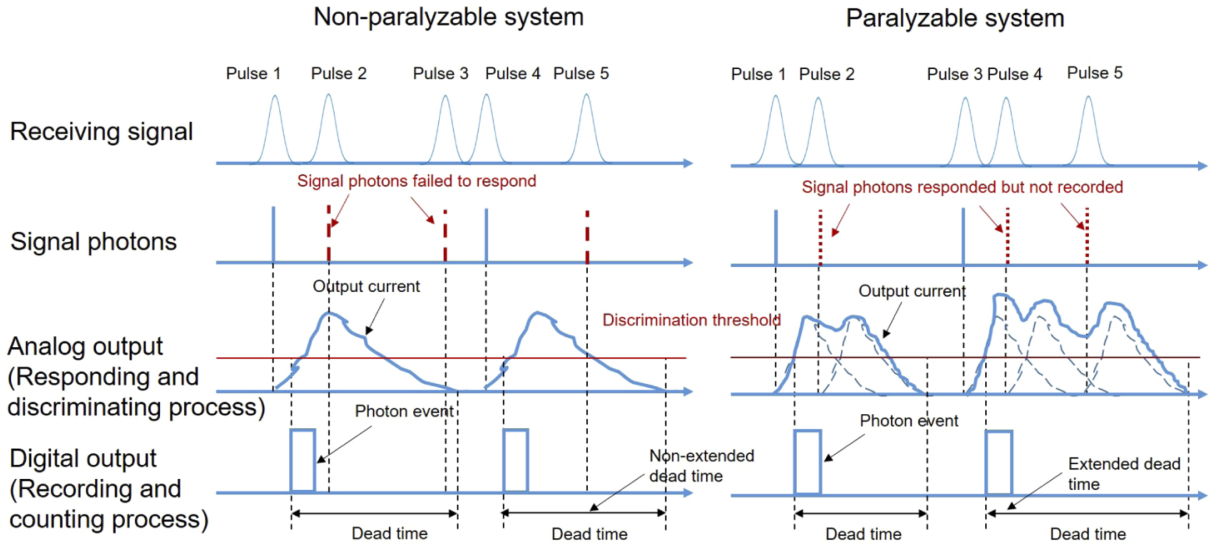

Figure 2.2: Comparison between non-paralyzable and paralyzable system. The non-paralyzable system responds to the first photon received while the paralyzable system responds to all the arriving photons. However, due to the existence of the dead time effect, both systems only record one photon event within a dead time extent [26].

Charge sharing

Charge sharing is an effect that can be observed in pixelated position-sensitive devices when a photon interacts with a sensor on the border between pixels (Figure 2.3). Hence, it becomes an important issue for detectors with small pixel sizes, leading to a deterioration in both detection efficiency and spatial resolution. When an X-ray impinges in a Photon Counting Detector (PCD), a charge cloud is created and the electrons and holes drift towards the respective electrodes under the action of the electric field generated by the applied voltage bias. Due to the diffusion effects and the Coulomb force the charge cloud grows in size. If the electron charge cloud reaches the anode near a pixel boundary, it

may happen that it is detected by multiple pixels at energies lower than the original one, causing a distortion in the spectral response. This effect strongly depends on the sensor material, the pixel size, the applied bias voltage, the depth of interaction in the sensor and the energy of the incoming photon [27].

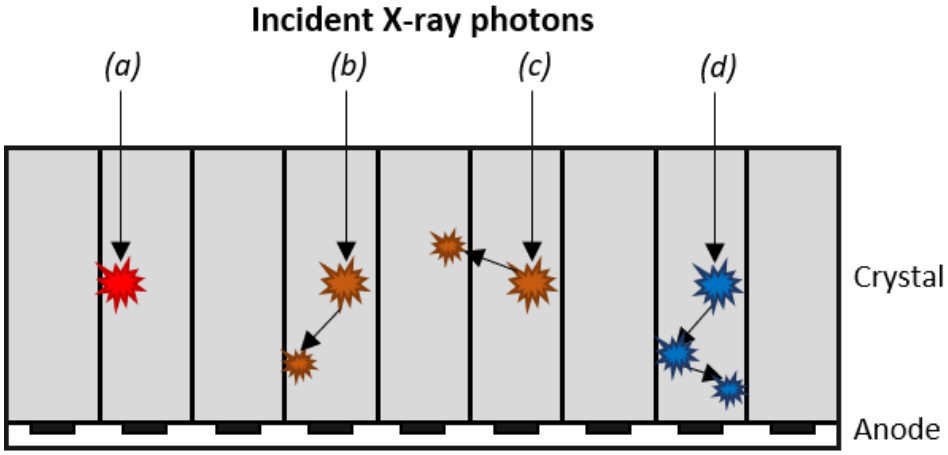

Figure 2.3: Possible X-ray interactions which may contribute to signal degradation in a PCD. An interaction close to the pixel boundaries will be detected by multiple adjacent pixels (charge sharing effect) (a). The photoelectric effect results in a K-escape characteristic X-ray of the PCD sensor, which can be absorbed by the same pixel (b) or by another pixel (c). Multiple Compton scattering results in multiple quasicoincident events (d).

K-escape X-rays

An impinging X-ray, interacting through the photoelectric effect, leads to the release of an electron in one of the inner shells of the sensor atoms, leaving the atom ionized. As a consequence, a higher orbit electron fills the vacancy left by the ejected electron, emitting a characteristic secondary fluorescent X-ray photon or an Auger electron. The emitted photons may either be absorbed by the PCD pixel with the primary interaction, be detected by an adjacent pixel or leave the detector (Figure 2.3). In the first case the two charge clouds generated by the primary and secondary photon may result in quasi-coincident events. If the detector electronics is sufficiently fast, they may be detected as two different counts, otherwise as a single one, resulting in a phenomenon similar to pulse pileup. In case the secondary photon leaves the pixel where it is generated, the recorded energy is lower by the K-shell energy.

Compton scattering

The Compton scatter occurs when an X-ray photon is scattered by the PCD, which leads to a change in its direction, a partial loss of its energy and a deposition of the lost energy

at the interaction site (Figure 2.3). This photon can be absorbed by a pixel, detected by an adjacent pixel or leave the PCD. It can be detrimental to the image quality since the total charge of the photon is not registered and the scattered photon may be counted in another detector element, thereby contributing to image noise and detector blur.

Charge trapping

When designing a semiconductor-based detector is important to take into account charge trapping, which tend to be more pronounced when using high Z-compound materials like CdTe. It consists of a temporary trapping of electrons and holes by trapping centers (see Section 2.1.2), hence leading to a reduction of the signal induced in the readout channel. Various strategies can be adopted to limit this phenomenon: a reduction of the sensor thickness, an increase of the electric field in the material and using materials with higher carrier mobility [28]. Moreover, the so-called "small pixel effect" can be exploited to improve charge collection. In fact, if a detector has pixels of small dimensions, then the carriers drifting towards the electrodes will encounter fewer trapping centers, thus leading to higher charge collection efficiency and spatial resolution.

Sensor polarization

Polarization is a phenomenon occurring in semiconductor detectors that leads to a time-dependent decrease of the count rate and charge collection efficiency [21]. It is due to a distortion of the electric field profile in the detector, consequence of trapping and de-trapping of the carriers. The sensor must be designed such that the charge generated by the X-ray photon is removed from the device at sufficiently high rate through both drift and recombination. This phenomenon can be minimized by applying a high bias voltage and operating at low temperatures.

2.2. Hybrid pixel detector technology

Hybrid detectors with photon-counting pixels have proven to be very powerful tools at synchrotrons. Recent developments continue to improve their performance, especially for higher spatial resolution at higher count rates with higher frame rates. In a hybrid detector, the absorption and signal-processing processes are performed by two separate components which are usually connected together by bump-bondings, high-density interconnects. A schematic representation is represented in Figure 2.4. This allows to optimize independently the absorption and signal processing, providing greater flexibility but at the same time limits the smallest pixel size obtainable. Moreover, the creation of the high-density connections between the two layers of material is delicate, time-consuming and expensive process.

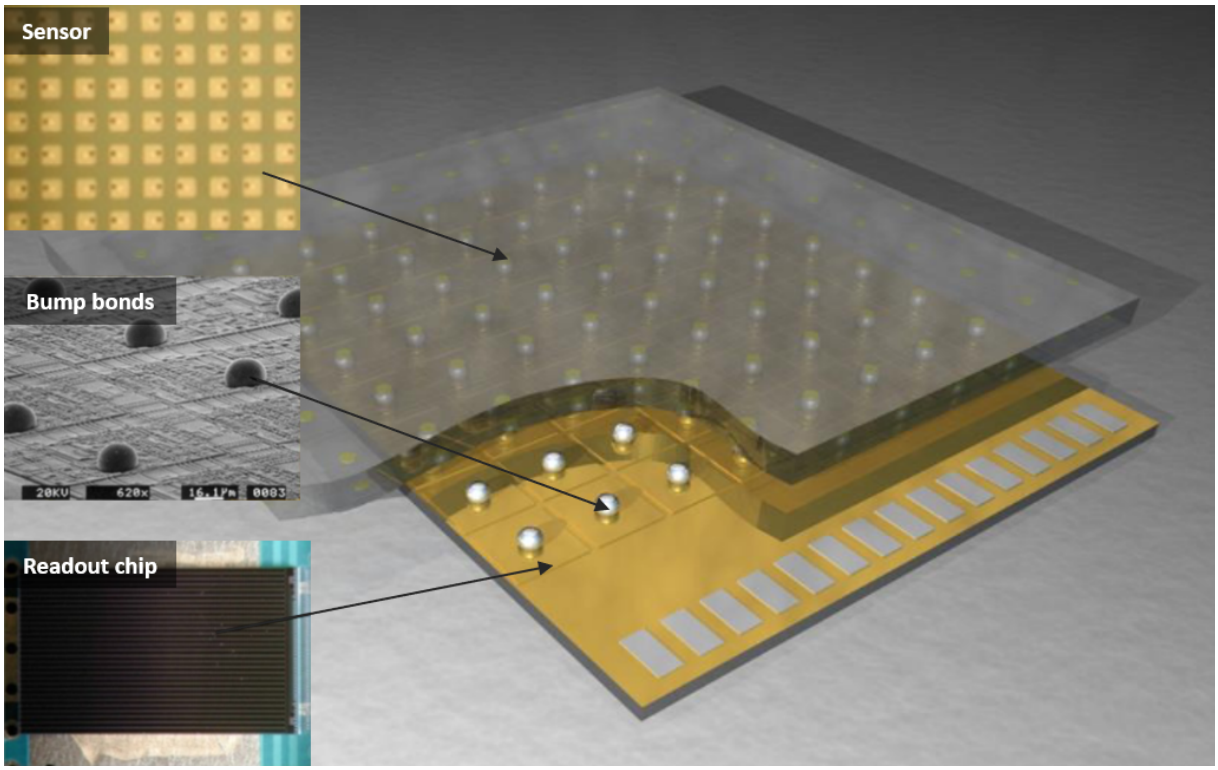

Figure 2.4: Schematic representation of a hybrid pixel detector with sensor and electronics chip connected via bump bonds. Modified from [29].

Two types of image acquisition can be distinguished: *photon counting* and *charge integration*. In photon counting systems the signal generated by the impinging photon is immediately processed and compared to a suitably set threshold in order to decide whether the observed signal corresponds to that expected from a photon of a specific energy. Signals exceeding this threshold during the integration time are appropriately stored in a counter in each pixel of the detector. Hence, a detector operating in this way allows to distinguish whether a signal is generated by a photon of desired energy or by a photon of too high (higher harmonics) or too low energy (fluorescence). However, the main limitation of single photon counting detectors is their limited count-rate capability. This limitation comes from signal pileup (see Section 2.1.4) where the signal of two or more photons is counted as one. Usually this type of detectors has a count-rate capability of a few MHz and hence requiring large count-rate corrections. Further limitations are linked to the minimum achievable pixel size due to the high electronics required for each pixel and to the charge sharing phenomenon between pixels in the sensor (Section 2.1.4). On the other hand, in a photon integrating system the total signal, including noise, is integrated during a user-selected time. They overcome some limitations of single photon counting detectors like the count-rate capability and pixel size but for longer integration

times dark currents may generate significant noise. Moreover, no discrimination between photons of different energies is possible with this mode.

2.2.1. Working principle of a HPCD

In the following, the structure and operating principle of a typical semiconductor hybrid photon counting detector is presented in a generalised manner and without any claim to a detailed description. In particular, attention will be paid to certain aspects useful for understanding the results obtained and presented in the following chapters.

A hybrid photon counting detector (HPCD) is characterized by two core components: a semiconductor material (e.g. Si, CdTe or GaAs) with two electrodes, and Application Specific Integrated Circuits (ASICs). As already mentioned, once the electron-hole pairs are created by the impinging X-ray photon, they start drifting towards the corresponding monolithic and pixelated electrodes under the influence of the externally applied electric field. During the drift motion, a transient current is created and then processed by the connected ASIC through one charge sensitive pre-amplifier, a pulse shaper, multiple comparators and digital counters.

Sensor design and material

Hybrid photon counting sensors are pixelated semiconductor crystals a few hundred micrometres thick. They absorb photons in an energy range determined by their material. When an X-ray is absorbed in the sensor, a charge cloud of a certain number of electrons and holes, proportional to the energy of the impinging photon, is generated. Under the action of an external electric field the charges drift towards the respective electrodes (Figure 2.5). Despite some diffusion and charge repulsion effects, the carriers transfer the signal to the readout electronics.

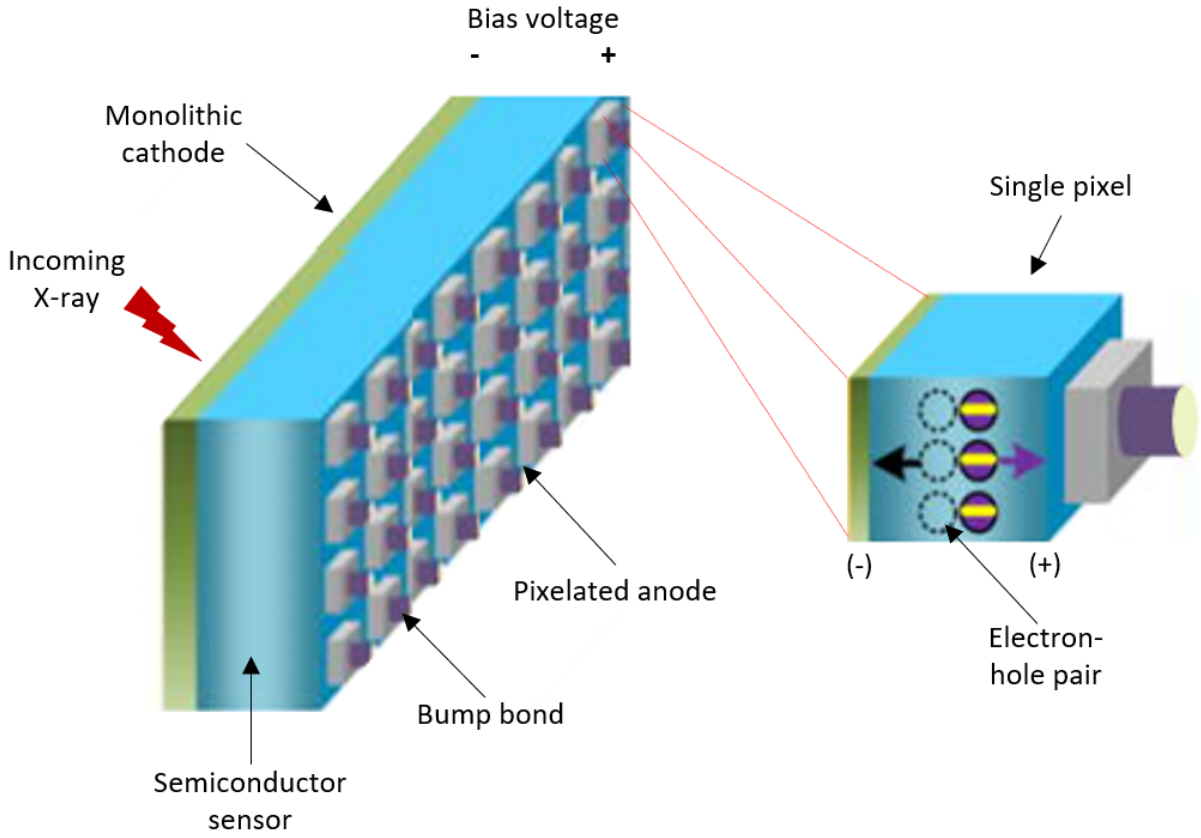

Figure 2.5: Schematic of a semiconductor based photon counting detector: each incoming X-ray photon interacts with the semiconductor material and the deposited energy generates electron-hole pairs which move towards the corresponding electrode, as shown in the enlarged pixel. Adapted from [30].

The choice of the sensor material is extremely important, according to the application. Silicon material is the most appropriate choice at relatively low energy range (< 20 keV), showing high absorption efficiency for sensor thickness up to 500 µm. It is a well understood semiconductor and homogeneous large Si wafers are easily buildable. However, it is not acceptable in low-dose medical imaging applications or in hard X-ray material science experiments at energies higher than 30 keV [31]. Especially, for what concern medical imaging, high quantum efficiency is an important requirement as it allows a high-quality image to be obtained while minimising the X-ray dose to the patient. For that purposes, it is necessary to use alternative semiconductor materials with higher atomic numbers, preferably with a wide-enough band gap to allow operation at room temperature. Currently, there are few promising options such as CdTe or GaAs. Figure 2.6 shows their typical absorption efficiency compared to Si sensors. However, these high-Z materials, compared to Si, shows some weaknesses such as poor uniformity, poor material properties

or difficult fabrication.

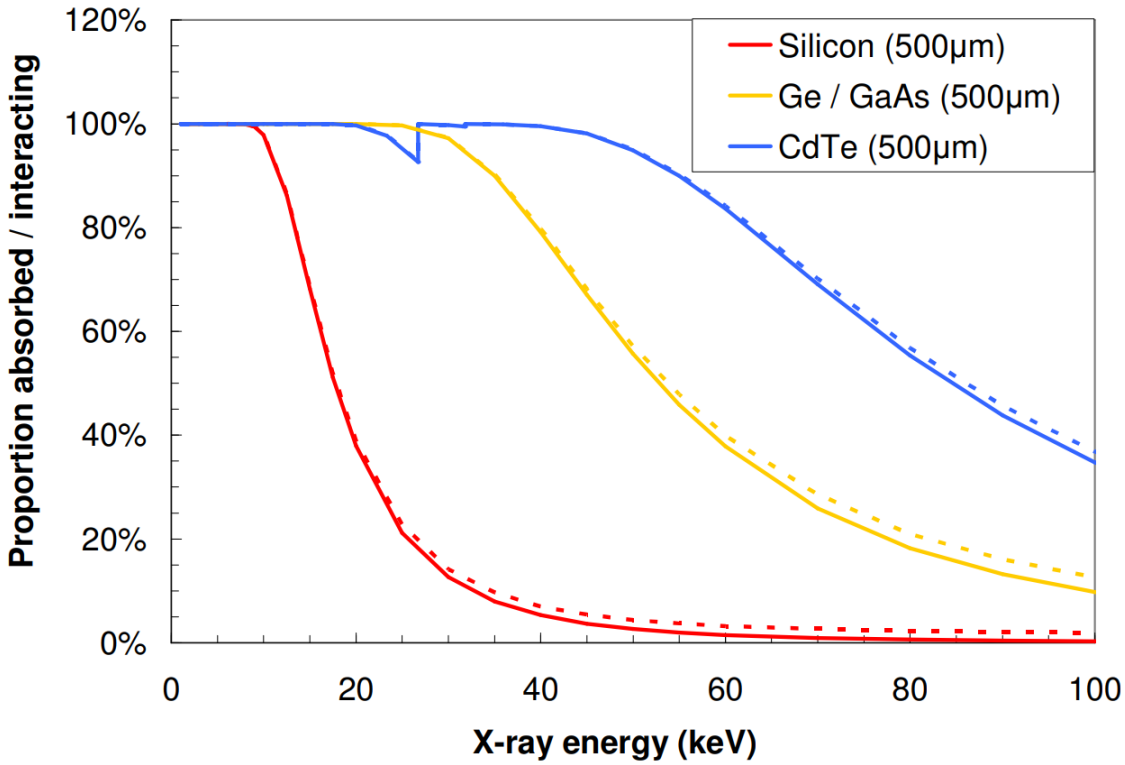

Figure 2.6: Photon absorption efficiency of different semiconductors. The solid line indicates the proportion of incoming photons absorbed by the photoelectric effect, and the dotted line shows the proportion interacting by photoelectric absorption or Compton scattering [32].

Focusing on the development of this thesis, linked to the development of synchrotron light source experiments, it is extremely important to underline the importance of having a uniform wafer [32]. With monochromatic beam, flat-field correction [33] (i.e. using an image acquired without a sample (flat-field or white-field image), to correct subsequent images) is able to compensate variations in pixel count rates of a few percent but larger variations and dead pixels will prevent accurate measurement of intensity. Large detector systems are used for these applications. However, since it is not possible to create an unique crystal sensor of the required dimensions, these detectors must be constructed by placing several crystals side by side. In practice, attempts are made to compensate for these gaps between sensors by taking multiple images at different sensor positions. Nevertheless, where possible, these gaps should be minimised.
Compared to elemental semiconductors, high-Z materials show high defects concentration since usually are made by compound semiconductors. This may lead, for example, to image non-uniformities as shown in Figure 2.7.

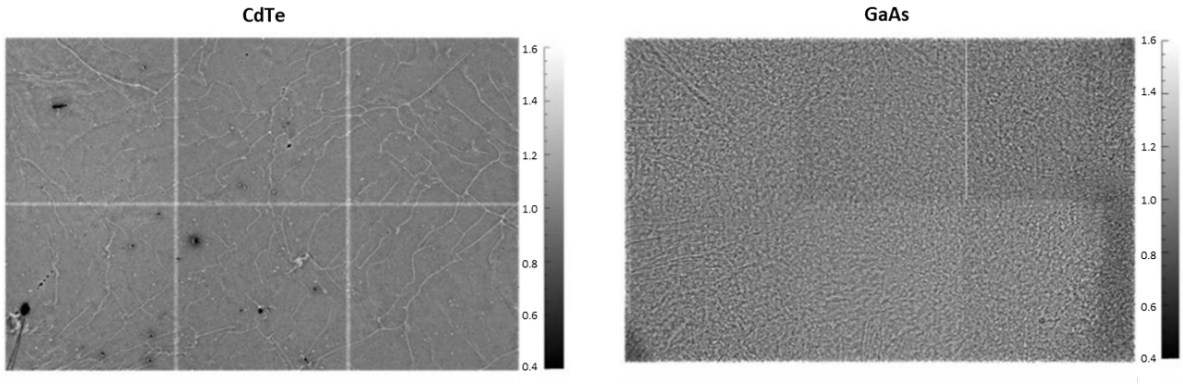

(a) (b)

Figure 2.7: Flat-field images from uniform X-ray exposure of high-Z sensors, (a) CdTe and (b) GaAs, show imperfections, generally not stable over time. The images are normalized to the average pixel value. Adapted from [34].

The flat-field image of the CdTe sensor shows a pattern of overlapping lines on a more uniform response. These lines, corresponding to dislocations in the material, are characterized by high counts in the centre of the line and lower counts towards the edges. In some regions, blobs of insensitive pixels, typically flooded with scattering current, are observed. Since these imperfections are generally not stable over time and with accumulated dose, they can only partly be corrected by the flat-field correction. On the other hand, the raw image of the GaAs sensor exhibits a high level of non-uniformity, with a granular structure which is probably related to the original growth process of wafer. However, there are fewer insensitive pixels compared with CdTe and the inhomogeneity is stable over time; hence image quality can be greatly improved with flat-field correction [34].

Fluorescence, i.e. the emission of a fluorescence photon following the absorption of a photon by photoelectric effect, is an additional aspect to be carefully considered when dealing with high-Z materials for the sensor. In Si the fluorescence photons, having low energy, do not travel very far in the detector, thus little contributing to image quality. In higher-Z materials, K-shell fluorescence photons can carry a large amount of energy, thus travelling longer distances and reaching adjacent pixels or leaving the detector. If this occurs, blur images are obtained, mainly if the incoming photon energy is immediately above the K-edge. The K-shell energy, fluorescence yield and the mean absorption distance of fluorescence photons all increase with the material's atomic number.

Cadmium Telluride

CdTe has been considered a promising semiconductor material for hard X-ray detection since the early 1970s. Nowadays it is a well-established detector material due to significant

technological advances that have enabled the production of high-quality single crystals of CdTe. Since it is the material employed in the EIGER detector sensor, in this section we summarize its main characteristics, reiterating some concepts already introduced previously.

Main properties of CdTe are reported in Tables 2.1 and 2.2. The high atomic number of the materials result in high quantum efficiency at high energies, which makes CdTe a good choice for experiments at 80 keV and above. Moreover, a large band gap allows to operate these detectors at room temperature, avoiding sensor cooling systems, required when using a material such as Ge. Cadmium and Tellurium have the K-edge around 26-32 keV, so if the incident X-rays are in the energy range of about 27-50 keV, fluorescence photons can be produced. The latter may escape from the detector, reducing the signal, or may blur the image if reabsorbed into nearby pixels.

	K-edge energy [keV]	**Characteristic X-ray energy [keV]**
Cd	26.711	23.17
Te	31.814	27.47

Table 2.2: K-edges energies and characteristic X-ray energies of K_α fluorescence of Cd and Te [35, 36].

When small pixel sizes are exploited, grain boundaries can be observed as various lines with increased count rate, surrounded by lines of decreased count rate (Figure 2.7). In this sub-grain boundaries impurities and aggregate space charge are concentrated, acting also as trapping centres for drifting charges [31]. These aggregates of charge and impurities are due to a distortion of the electric field. Hence, charge is collected in adjacent pixels and the resulting images appear distorted around those areas.
Changes in flat-field response over time are observable for CdTe, as seen in Figure 2.8, where a continuous illumination of a single chip has been performed for 3 hours. A clear increase of counts is observed along the boundaries. This phenomenon implies that a single flat-field measurement is not fully correct for the non-uniformities in the detector over an extended period of time. Blobs, preferentially laying at the surface of the detector, show an increasing anisotropic halo all around (see Figure 2.8b) at increasing times of continuous irradiation. Moreover, both temporary and permanent damage (high incident fluxes) have been observed after irradiation on the sensor. In light of these aspects, a bias voltage reset is highly recommended before making measurements to reset temporary changes in the flat-field images.

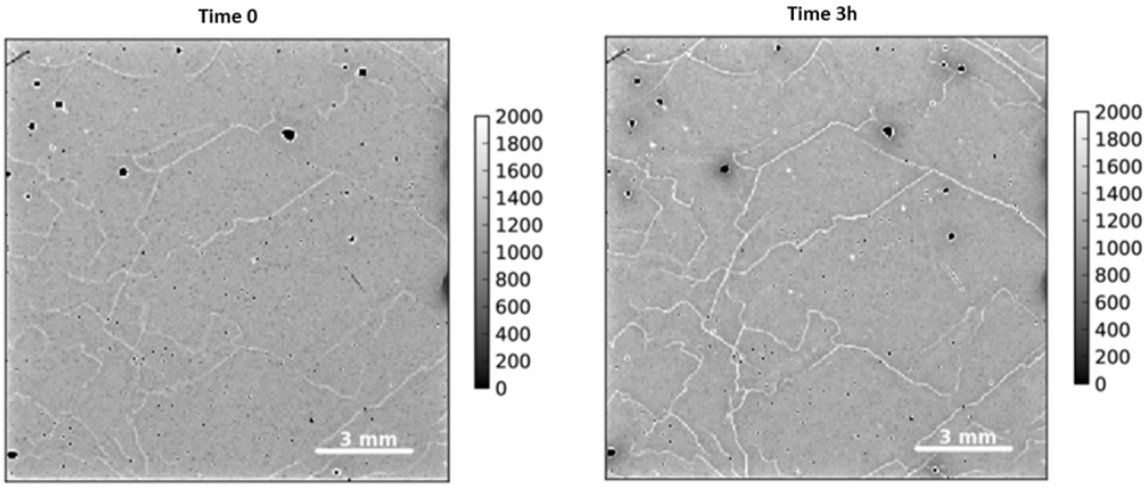

(a) (b)

Figure 2.8: Flat-field images acquired with a chip of CdTe sensor at the beginning (a) and after 3 hours (b) of continuous irradiation with photons of energy of 22 keV. As the exposure time of the sensor to the radiation increases, the visibility of grain boundaries becomes higher and blobs show an increasing anisotropic halo all around [31].

Readout ASIC

As already mentioned in Section 2.2, the charge generated by the absorbed X-ray photon drifts under the action of an applied electric field and a transient current is generated and processed by the connected ASIC, represented in Figure 2.9. The readout chip is segmented into pixels the same size as the sensors. Each readout pixel measures the transient current arriving from the corresponding pixel of the sensor layer through a charge-sensitive preamplifier. The charge signals acquired from the charge-sensitive preamplifier are then shaped and amplified by the pulse shaper, which produces an output voltage pulse with peak amplitude proportional to the initial deposited energy. This latter pulse is sent to multiple voltage pulse height comparators, characterized by tuneable pulse height (energy) thresholds. If the incoming voltage pulse is higher that the selected threshold, the corresponding digital counter is incremented and a count is registered. The key advantage of using an energy threshold is that it is possible to detect photons in a well-defined energy window. Moreover the use of a threshold prevents, for example, the accumulation of electronic noise, dark current from the sensor and the detection of fluorescence photons.

According to the use and setting of the thresholds it is possible to distinguish two operating modes: *imaging mode* and *scanning mode* [30]. In the imaging mode all the thresholds for comparators are set to a fixed value when detecting X-ray photons while in the scanning

mode, the entire range of pulse height is scanned by progressively reducing the threshold according to well-defined steps.

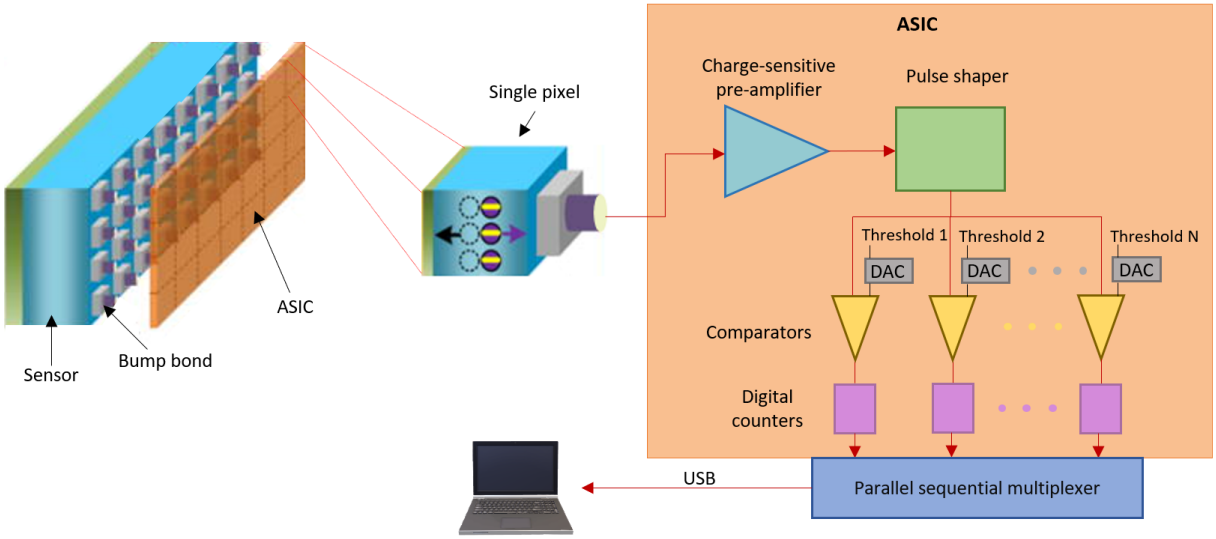

Figure 2.9: Schematic of a semiconductor based photon counting detector and the corresponding ASIC of a single pixel. The transient current generated by the electron-hole pairs is processed by the ASIC through a charge sensitive preamplifier, a pulse shaper, N voltage pulse height comparators and digital counters [30].

2.3. EIGER2 X CdTe 1M-W detector

As already mentioned, in October 2020, the ID17 biomedical beamline received EIGER2 X CdTe 1M-W detector from the world leading developer and manufacturer of X-ray and electron detectors DECTRIS. Its purchase was conceived in light of a beamline instrumentation upgrade project and to accommodate the increased photon flux provided by the new EBS source. EIGER2 is the new family of photon-counting X-ray detectors with 75 µm pixel resolution for both synchrotron beamlines, with the X series [37], and for laboratory instruments, with the R-series [38]. The applications with EIGER2 X, for synchrotron beamlines, are mainly intended for X-ray diffraction experiments [39, 40]. However, ID17 has decided to purchase it with the aim of exploiting the detector for biomedical imaging, hence an accurate characterization became necessary to understand both its performances and its compatibility in typical experiments, such as tomographic scans.

2.3.1. Detector general structure

EIGER2 X CdTe 1M-W is a hybrid single-photon counting detector (see Section 2.2 and Figure 2.10). The main building blocks are the pixelated CdTe sensor and the Complementary Metal-Oxide-Semiconductor (CMOS) readout chip.

Figure 2.10: Front view of EIGER2 X CdTe 1M-W hybrid photon-counting detector [41].

EIGER2 is constituted by two juxtaposed modules of 8 chips of 256×256 pixels each. The pixel size is 75×75 µm^2. The detector structure is represented in Figure 2.11 . The CdTe sensor, placed on top of the two modules, is not a single crystal but 4, each of them covering 256×256 pixels. These single CdTe crystals are called *half sensors*. In between chips there is a physical gap, but since the sensor covers that part, the signal impinging in those areas is not lost. A pixel at the edge of a chip receives more signal with respect to a pixel at the center and hence a "virtual pixel correction" is performed by adding virtual pixels on each side of a chip. Both the virtual pixel and the adjacent physical one are attributed half of the counts measured by the latter. There are some inactive areas: a 2 pixels gap in between the half sensors in a module and a 12 pixels gap in between the two modules. The total insensitive area of the detector amounts to 6%.

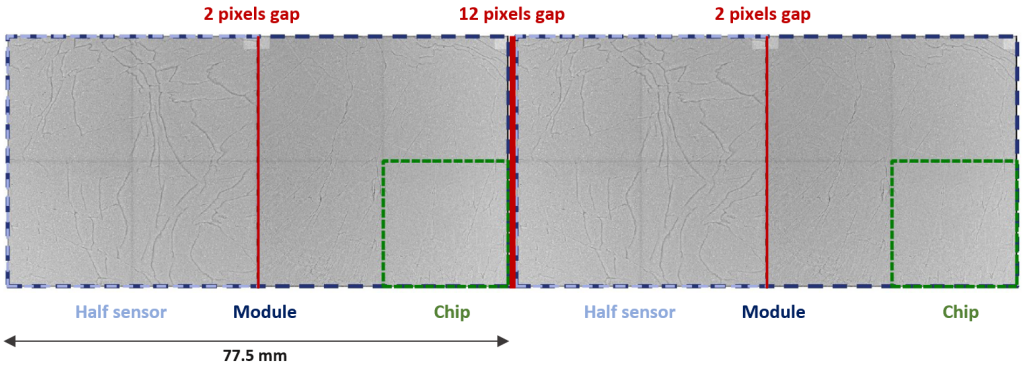

Figure 2.11: EIGER2 X CdTe 1M-W module structure. It is constituted by two juxtaposed modules of 8 chips each. Above each module two CdTe crystals (half crystals) are placed. In red are highlighted the inactive areas: a 12 pixels gap in between the two modules and a 2 pixels gap in between the half sensors. Modified from [42].

CdTe sensor

EIGER2 sensor is a 0.75 mm thick CdTe crystal, determining a detection efficiency higher than 60% in the range 25-60 keV. In Figure 2.12 is reported the simulated and measured quantum efficiency curve, as a function of photon energy, provided by DECTRIS. The drop observed in the quantum efficiency corresponds to the K-edges of cadmium and telluride (see Table 2.2). For further information about CdTe please refer to Paragraph "Cadmium Telluride" of Section 2.2.1.

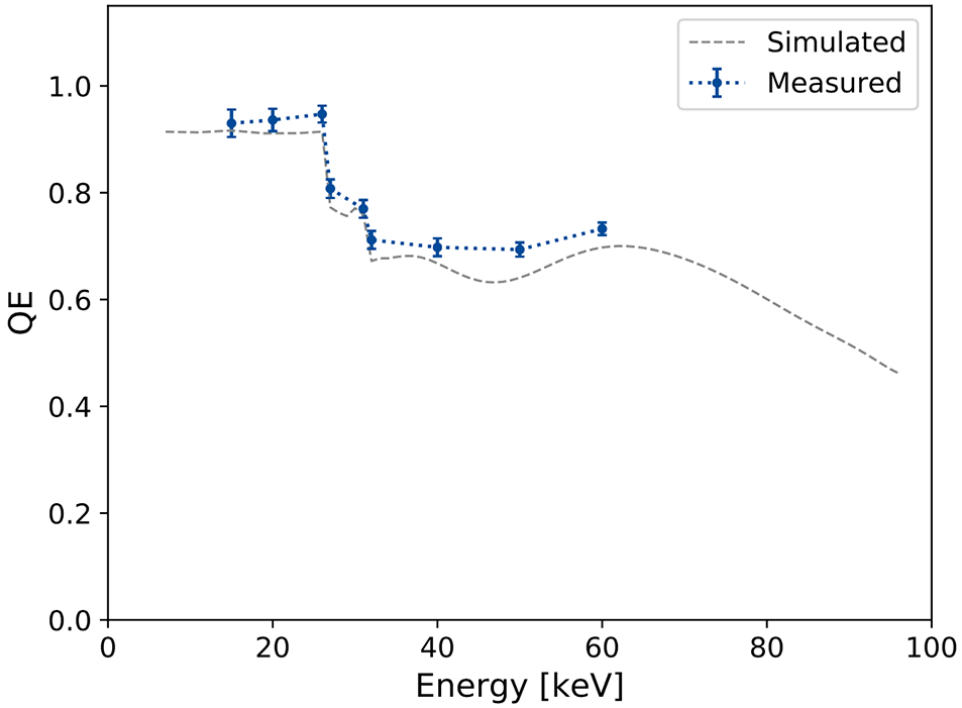

Figure 2.12: Simulated and measured Quantum Efficiency (QE) of a CdTe sensor of 0.75 mm thickness. [43].

IBEX: readout ASIC

The ASIC is based on the novel IBEX chip developed at DECTRIS Ltd. [44]. The front-end electronics of each pixel in the matrix is characterized by a low noise Charge-Sensitive Preamplifier (CSP), a fast shaper AC-coupled to the output of the preamplifier, two independent CoMParators (CMP) with selectable energy threshold (see Paragraph "Readout ASIC" from Section 2.2). Two digital counters for each comparator allow to take advantage of dual-energy discrimination. A block representation of a single chip is represented in Figure 2.13. The CSP has an adjustable gain to cope with the desired dynamic range and it is compatible with signals of both polarities. A double counter allows continuous read-out with a dead time lower than 100 ns and maximum frame rate of 2

KHz. At frame rates below 300 Hz, a default "auto-summation" of frames, accumulating images taken at 300 Hz, is activated. The ASIC can operate in a continuous read out mode with two independent 16-bit counters or in a high counting range mode with a single 32-bit counter per energy threshold level.
IBEX offers an instant retrigger technology, similar to the one implemented in PILATUS3 readout chip [45], with a tunable retrigger-time that yields non paralyzable counting and improve high-rate counting performance. The maximum count-rate capability reachable with this detector is 10^7 photons/pixel/s. The instant retrigger block can be activated or deactivated anytime. EIGER2 features dual threshold mode but only the difference image, namely the difference between the image only with threshold 1 (th1) and the image with threshold 2 (th2), is available to the user. Default threshold values are: th1 = (0.5 × photon energy) and th2 = (1.4 × photon energy), while the lowest threshold value that can be set is 4 keV.

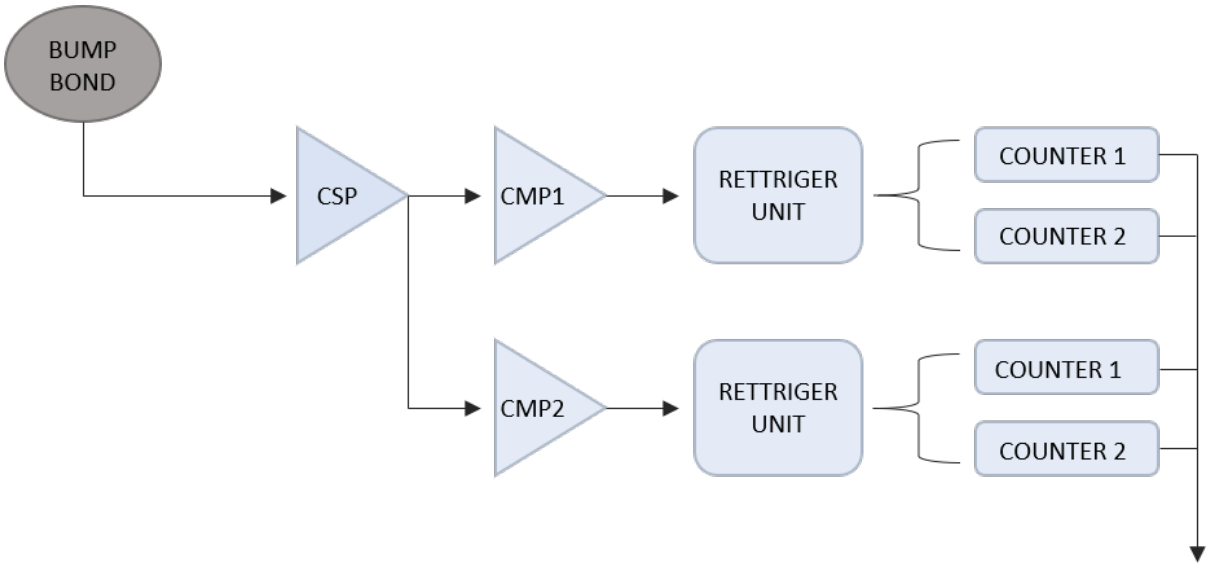

Figure 2.13: Schematic of a single pixel ASIC. The front-end electronics of each pixel is constituted by a low noise charge-sensitive preamplifier, two independent comparators with selectable energy threshold and two retrigger units. Each of these units are output connected to a double counter that allows continuous read-out.

EIGER2 features some automatic software corrections that can be enabled of disabled depending on the needs of the operator; among the main ones there are:

- flat-field correction,
- count-rate correction,

- pixel mask correction.

In most experiments the data quality benefits from data corrections, thus disabling one of the corrections could lead to lower data quality. As already introduced, the flat-field correction consists in correcting subsequent images with an image acquired without a sample to compensate variations in pixel count rates. count-rate correction is used to compensate for counts loss at high photon fluxes. Defective pixels, which can be under-responding or over-responding, are corrected by the so-called *bad pixel mask*. By default, all pixels registered the pixel mask are forced to the saturation value.

2.3.2. Operating conditions

EIGER2 X CdTe 1M-W detector is designed for indoor use only and has a temperature and humidity sensor. If either sensor detects that the operating conditions are not met, the detector will shut down. However, since the sensors cannot prevent damage, the temperature and humidity should be monitored to avoid exceeding the operating limits. To avoid humidity and condensation damage the detector has to be connected to a dry air or nitrogen source. Table 2.3 shows the ambient conditions that must be satisfied for the detector to work under optimum conditions.

Ambient Condition	
Operating temperature	+20°C to +35°C
Operating humidity	<80% at 20°C, non-condensing
Storage temperature	+15°C to +40°C
Storage humidity	<40% at 20°C, non-condensing

Table 2.3: Detector operating ambient conditions [41].

Moreover, the detector system is water-cooled and requires a dedicated thermal stabilization unit. The operating conditions are reported in Table 2.4. In Figure 2.14 is reported the back view of the detector, appropriate tubes must be inserted to allow the influx of coolant and dry air to keep the detector in stable operating condition.

Condition	
Operating temperature	+25°C
Maximum operating pressure	3 bar
Coolant	66% distilled water and 34% ethylene glycol

Table 2.4: Detector operating conditions [41].

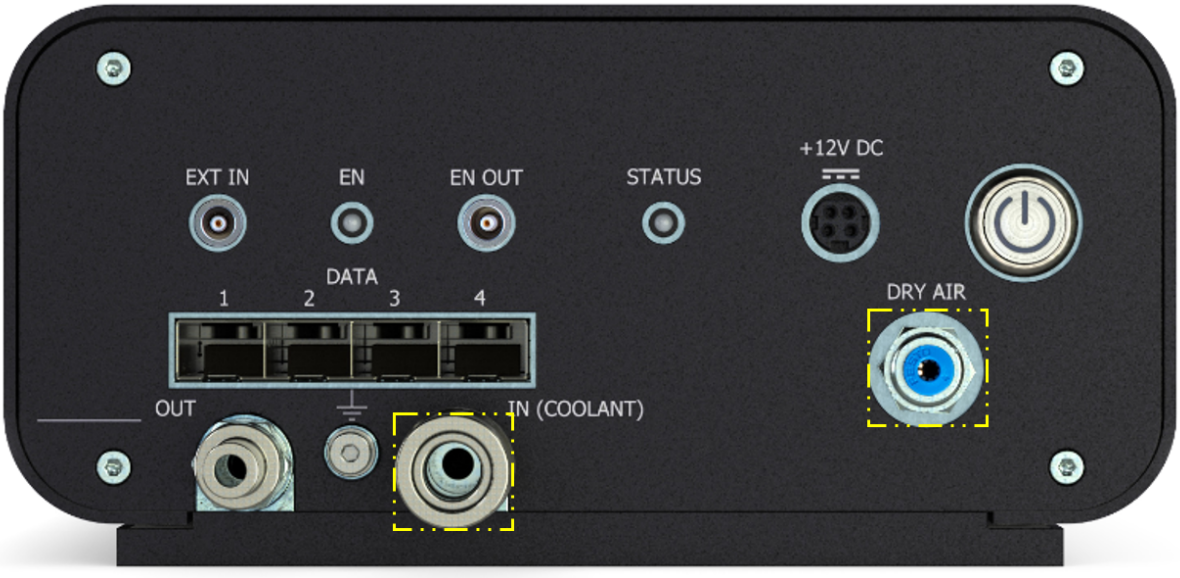

Figure 2.14: Back view of EIGER2 X CdTe 1M-W detector. Connection points for coolant and dry air are highlighted [41].

2.3.3. Computing infrastracture

The general layout of the EIGER2 Data-AcQuisition, DAQ is represented in Figure 2.15. The Detector Control Unit (DCU) is connected point-to-point to the detector via 4× LC/UPC duplex fiber optic connectors [41]. The software running in the DCU deals with the detector control and the reconstruction and correction of the acquired 2D data. It provides a platform-independent control interface through a HTTP server using a RESTlike Application Program Interface (API): SIMPLON [46]. The HTTP-based API is RESTlike since every detector source is uniquely identified by its Uniform Resource Locator (URL). The HTTP interface also allows the EIGER2 initialization and the verification of its connections. Three main modules for data retrieval are available: Stream and FileWriter for image retrieval at high rate and Monitor for low rate image acquisition ($<$ 10 Hz). FileWriter interface allows to control how data are stored in HDF5 files.

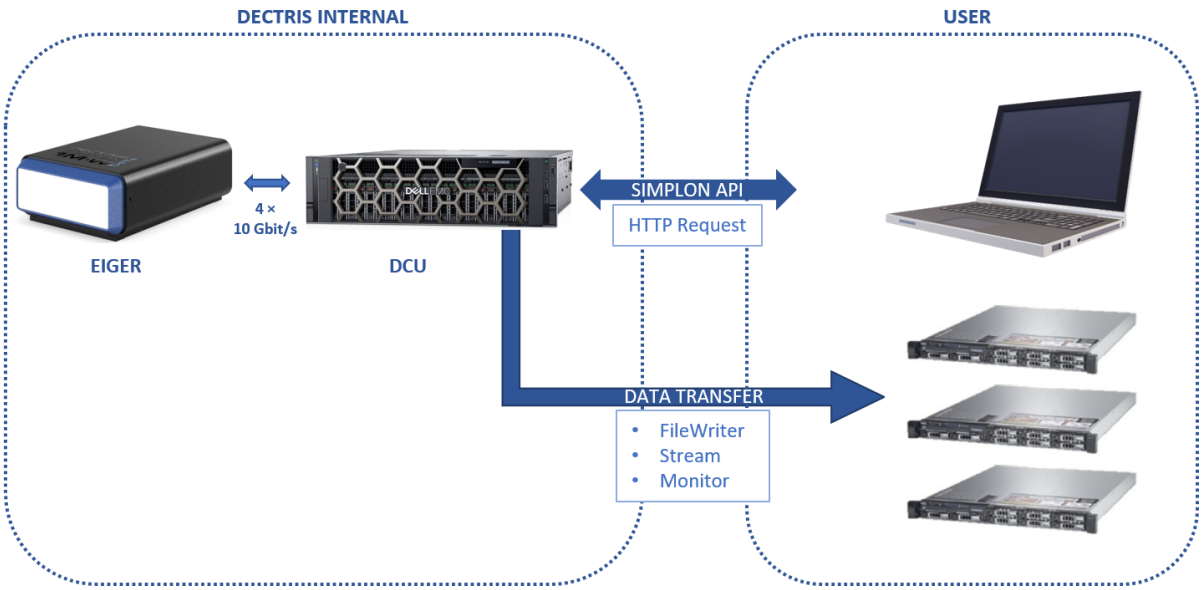

Figure 2.15: General layout of EIGER2 Data-AcQuisition. Modified from [41, 42].

At the ESRF, a Library for Image Acquisition (LIMA) for 2D detectors has been developed. It allows to export a common set of features for every detector, providing alternative software solutions when not implemented by hardware and it aims to exploit every optimization available in the detector, making use of intensive parallel algorithms [47]. The presently available file formats are EDF, Nexus/HDF5 and CBF (Crystallographic Binary File). In particular, the EDF is the file format in use at the ID17 beamline. In addition, LIMA allows parallel storage in a central storage server, an online data analysis workstation, or a network-attached storage with user disks that allow bringing data home. The LIMA software exploits SIMPLON API v1.6.0 [48] to control and configure the image acquisition and data collection through both the FileWriter and Stream mechanism.

3 | Theoretical outlines

In medical imaging the main goal is to provide enough information regarding specific aspects of human body structure and how the latter is altered following injuries or diseases. Thus, the image quality becomes a fundamental parameter to retrieve this information.
The image quality and the resulting information that can be extracted depends on: the irradiated object, the imaging system and the X-ray imaging technique, and the main factors affecting the image quality such as spatial resolution, noise and contrast. Generally, to have a good image quality and hence to be able to detect pathological features, spatial resolution and contrast should be high while noise low. However, these factors are not independent and they affect each other; the optimal balance among them depends on the purpose of the image. If either contrast or spatial resolution is too low, or if noise is too high, as shown in Figure 3.1, no clinical information can be extracted [49]. Spatial resolution is an indicator of the ability of an imaging system to represent sharp edges between distinct anatomical features with the imaged object. Contrast is the magnitude of the intensity difference between the object and the surrounding background. Noise, instead, describes the systematic and random fluctuations that superimposes on the signal that result from X-ray photons and the detector itself. Further explanation of these three concepts can be found in [49].

A full characterization of an imaging detector is of fundamental importance to optimize the image quality and to correctly interpret the results of an imaging experiment. In the first part of this chapter, the fundamental and basic concepts required to characterize an imaging detector in terms of its performances are provided. In particular, the linearity, the Modulation Transfer Function (MTF), the Noise Power Spectrum (NPS) and the Detective Quantum Efficiency (DQE) are presented.
In the second part, focusing on the main medical applications for which the EIGER2 was purchased, the principles of CT and of KES are reviewed. This will provide information on additional requirements of the detector which are specific to each application.

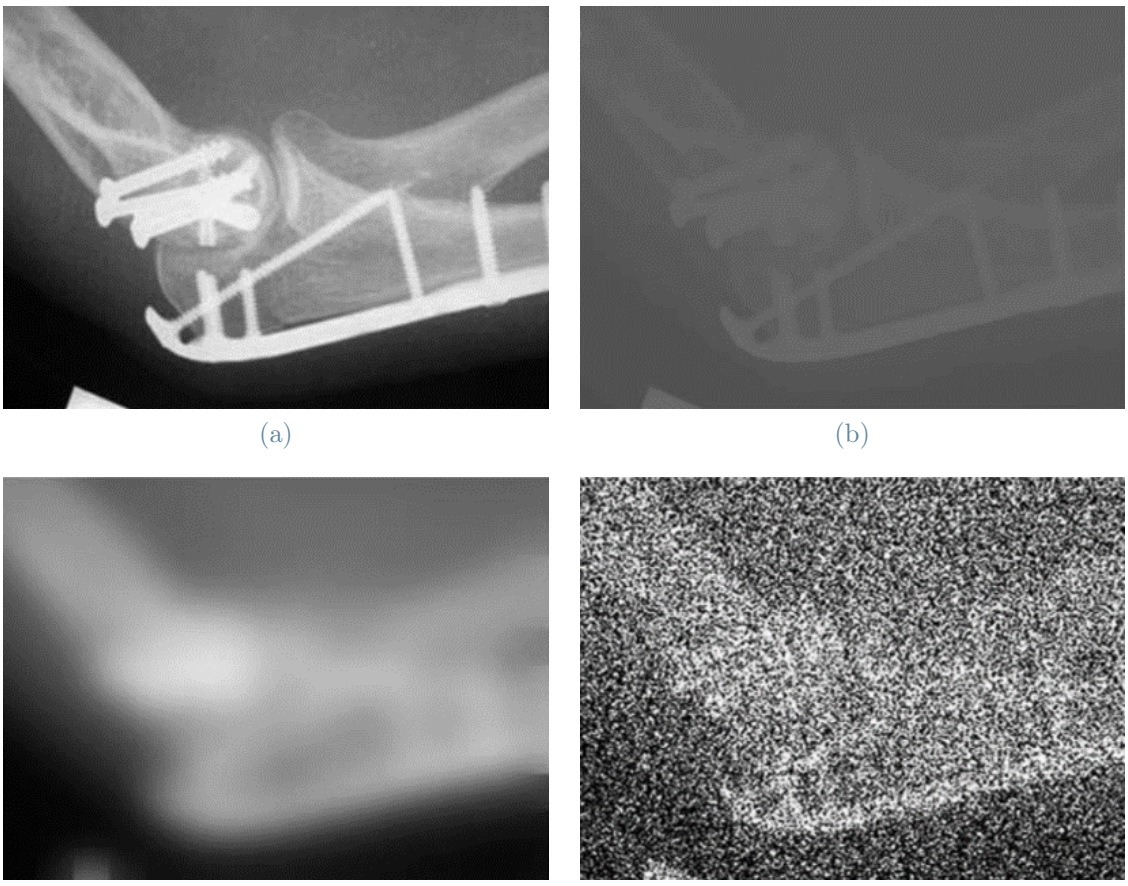

(a) (b) (c) (d)

Figure 3.1: A good image quality is reached for adequate contrast and resolution, and for a low noise level as illustrated in image (a). Image (b) shows high spatial resolution and low noise but almost zero contrast. Image (c) has high contrast and low noise, but extremely poor spatial resolution. In image (d) the high noise level is at the detriment of high resolution and contrast [49].

3.1. Linearity

Ideally, the transfer function between the incident photon number and the final digital output should vary linearly (see Figure 3.2). However, in all imaging systems there is a non-linearity between the input radiation intensity and the digital output response. Linearity represents a crucial property for imaging systems, where the image quality relies on absolute signal measurements. As already explained in Section 2.1.4, there are two mathematical models describing the behavior of detector systems: paralyzable and non-paralyzable. Although these models are simplifications of the behavior of real detection systems, real systems may behave like one or the other model. In particular, they follow the ideal curve for low count-rates while start to lose counts as the incoming photon flux

increases. For a paralyzable detector the registered count-rate reaches a peak value and then decreases, in accordance with the fact that an interaction occurring during the dead time after a previous interaction extends the dead time. On the contrary, the registered count-rate for a non-paralyzable detector increases slowly towards an asymptotic value. This is illustrated in Figure 3.2.

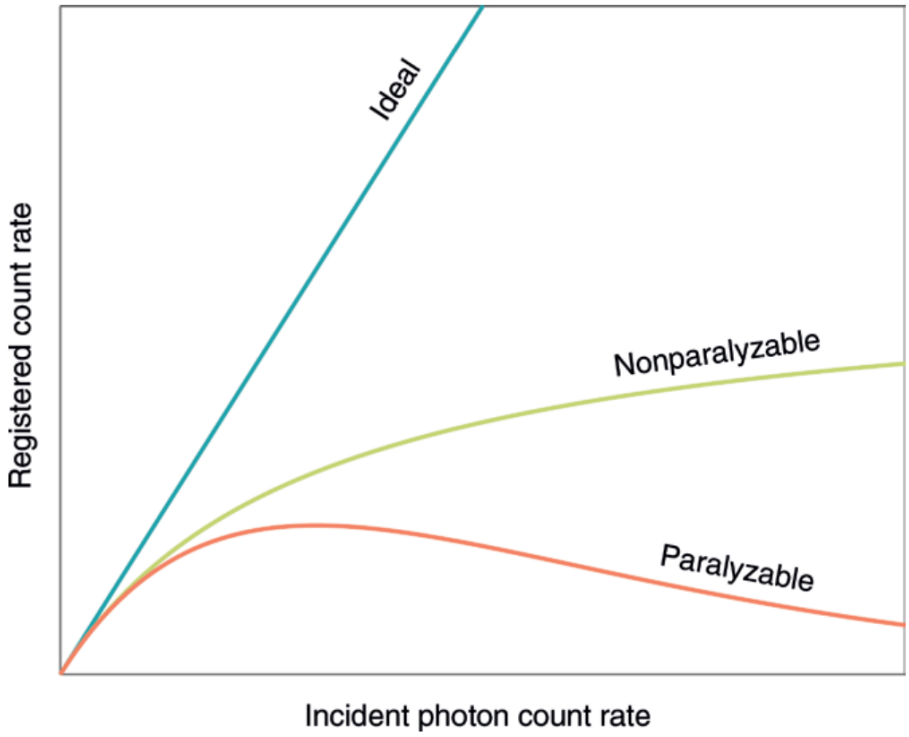

Figure 3.2: Examples of detector behavior under high count-rate irradiation. For an ideal detector, the registered count-rate is equal to the incident one. A real-life detector follows the ideal curve for low count-rates but starts to lose counts due to pile-up as fluence rate increases. Two models of detector behavior are plotted: a non-paralyzable detector, whose registered count-rate increases slowly toward an asymptotic value, and a paralyzable detector, whose registered count-rate reaches a peak value and then drops again [50].

3.2. Modulation Transfer Function

The modulation transfer function is an image-quality metric that determines how much a detector maintains the contrast in the original object. Thus, it characterizes how faithfully the spatial frequency content of the object gets transferred to the image [51].

Considering a transmission of a sinusoidal signal in the one dimensional (1D) object plane

we define the modulation of the input signal M_{in} and of the output one M_{out} as:

$$M_{in} = \frac{(|h_{max}| - |h_{min}|)/2}{(|h_{max}| + |h_{min}|)/2}, \tag{3.1}$$

$$M_{out} = \frac{(|g_{max}| - |g_{min}|)/2}{(|g_{max}| + |g_{min}|)/2}. \tag{3.2}$$

Where h_{max} (g_{max}) and h_{min} (g_{min}) represent the maximum and the minimum signal input (output) intensities. The ratio of the output to the input modulations of any spatial frequencies u introduced in the imaging system is called "modulation transfer function":

$$MTF(u) = \frac{M_{out}(u)}{M_{in}(u)}. \tag{3.3}$$

The spatial frequency (u) is usually given in cycles per millimeter $[cy/mm]$ or line pairs per millimeter $[ln/mm]$.

Conceptually, if an imaging system is spatially stimulated with a pure sine wave of frequency u and amplitude 1, it will still output a sine wave with the same frequency but, due to resolution losses of the system, with lower contrast (amplitude lower than 1). A peak at frequency u and height equal to the amplitude of the wave is obtained when the Fourier Transform (FT) of the resulting signal is calculated. If the input signal is constituted by more than one wave, the FT will separate the result for each frequency. The curve that develops from each of the frequency peaks will result in the MTF curve [52]. The process just described is depicted in Figure 3.3.
When complete transmission of the object's contrast occurs the MTF assumes a value equal to 1, while it takes on value 0 if no transmission of the contrast is verified. In general, the MTF decreases as a function of spatial frequency, meaning that the detectability of an object decreases due to the decrease of the contrast of the output image. In all those applications where it is necessary to distinguish small details, such as microcalcifications in mammography, it is necessary to have an image as sharp as possible and therefore a high resolution is required. Hence, the MTF should be the high as possible for all frequencies. In literature, the limiting resolution of the X-ray imaging system is often indicated as 5% or 10% of the MTF values.

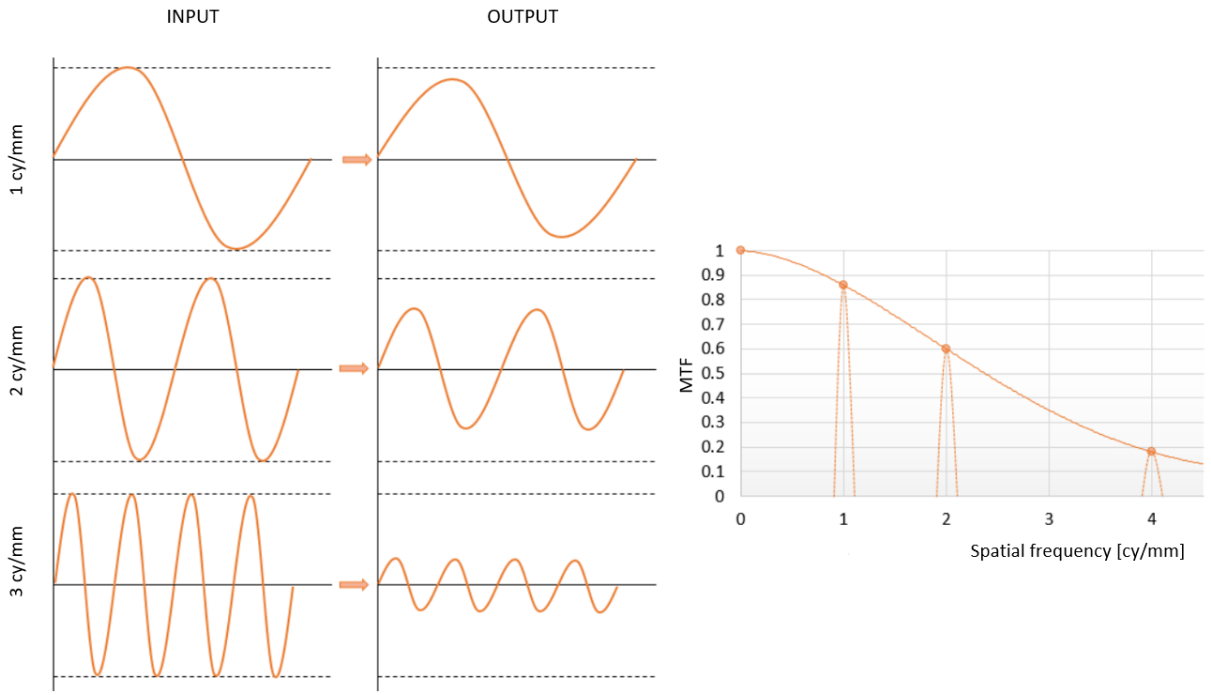

Figure 3.3: (a) Effect of the imaging system over pure sinusoidal profile and (b) visual explanation of how the MTF is obtained [52].

The dimension of the active portion of a detector element (pixel) defines an aperture and the latter determines the spatial frequency response of the detector itself. For example, for an ideal square pixel detector the ideal maximum MTF will be of the form of a sinc function, which is the FT of the aperture function [53]. The sinc function is expressed as:

$$sinc = \frac{sinc(\pi \Delta x \; u)}{\pi \Delta x \; u} \tag{3.4}$$

where Δx is the pixel pitch. The MTF will have its first zero at the sampling frequency $u = \Delta x^{-1}$. The latter corresponds to the double of the Nyquist frequency (F_{Nyq}), which is defined as $F_{Nyq} = 1/(2\Delta x)$. According to the sampling theorem, only the spatial frequencies in the pattern below the Nyquist frequency can be faithfully imaged. The frequency components beyond the Nyquist one may be subject to the so-called *aliasing* phenomenon: those frequencies are folded back to their counterpart frequencies prior to Nyquist frequency, increasing the apparent spectral content of the image at these lower frequencies. Thus, the frequencies of interest for the determination of the MTF are from zero up to the Nyquist frequency; a finer sampling should be used to precisely define the MTF without aliasing in this frequency range.

The MTF can be determined from three functions defined in the spatial domain: Point

Spread Function (PSF), Line Spread Function (LSF) and Edge Spread Function (ESF). They are illustrated in Figure 3.4.

- The **PSF**, which is a two dimensional (2D) function, is the response of the system to an infinitely small aperture (point source). In an ideal imaging system, the radiant energy emanating from the point source in the object plane would be concentrated in a point in the image plane. However, in real systems this does not occur since the image will consist of a round shape with higher intensity in the center, corresponding to the ideal image point, and lower intensity at increasing distances from the center. For a linear system a continuous, two-dimensional object can be seen as an assembly of an infinite number of point sources of various intensities whose image is obtained by the convolution of the input with the PSF. The 2D MTF is then obtained as the modulus of the FT of the PSF. However, the measurement of the PSF is experimentally difficult due to the need to create an infinitely small source and to exactly align it at the center of the distribution.

- The **LSF** is the radiation intensity distribution in the image of an infinitely narrow and long slit (line source). In a perfect imaging system, the radiant energy emanating from a linear source in the object plane would be concentrated into a line in the image plane. However, in real systems, as seen for the PSF, an unsharp image of the line source is obtained. The LSF, which is a good measure of the system resolution, overcome the problems that can be encountered with the PSF. Nevertheless, it introduces another engineering problem linked to the creation of an ideal line object. It is possible to determine the PSF in the two spatial directions x and y by the measured LSF since they are linked by the following relation:

$$LSF(x) = \int_{-\infty}^{+\infty} PSF(x, y)\ dy. \tag{3.5}$$

  However, it is not so easy to determine the PSF from the LSF since the latter is a 1D intensity distribution while the PSF is 2D.
  The method for calculating the MTF involving the LSF is called *slit method*. This method has been accurately described by Fujita et al. [54]. It exploits a narrow slit, positioned at a slight angle (typically $< 2°$) with respect to the pixel matrix, to measure the LSF at a sampling interval much finer that that provided by the pixel-to-pixel distance. The MTF is then obtained as the modulus of the FT of the LSF and it is normalized to one at zero frequency.

- The **ESF** describes the response of the system to a straight edge test device, which enables complete transmission on one side and an almost perfect attenuation on the

other one. The ESF can be defined as the integral of the LSF; that is:

$$ESF(x) = \int_{-\infty}^{x} LSF(x')\ dx'. \tag{3.6}$$

In this case, the method to calculate the MTF, the so-called *edge method* [55, 56] exploits a sharp edge usually made of tungsten or lead. Like the slit method, it is slightly tilted with respect to the pixel matrix. The ESF is first calculated and then differentiated to obtain the LSF. The Fourier amplitude of the LSF is the MTF. Usually this method is preferred to the slit one for its simplicity and practicality since, as already mentioned, the slit method requires precise fabrication and alignment of the slit.

A standard procedure, based on the edge method for the calculation of the MTF, is reported by the International Electrotechnical Commission IEC [57].

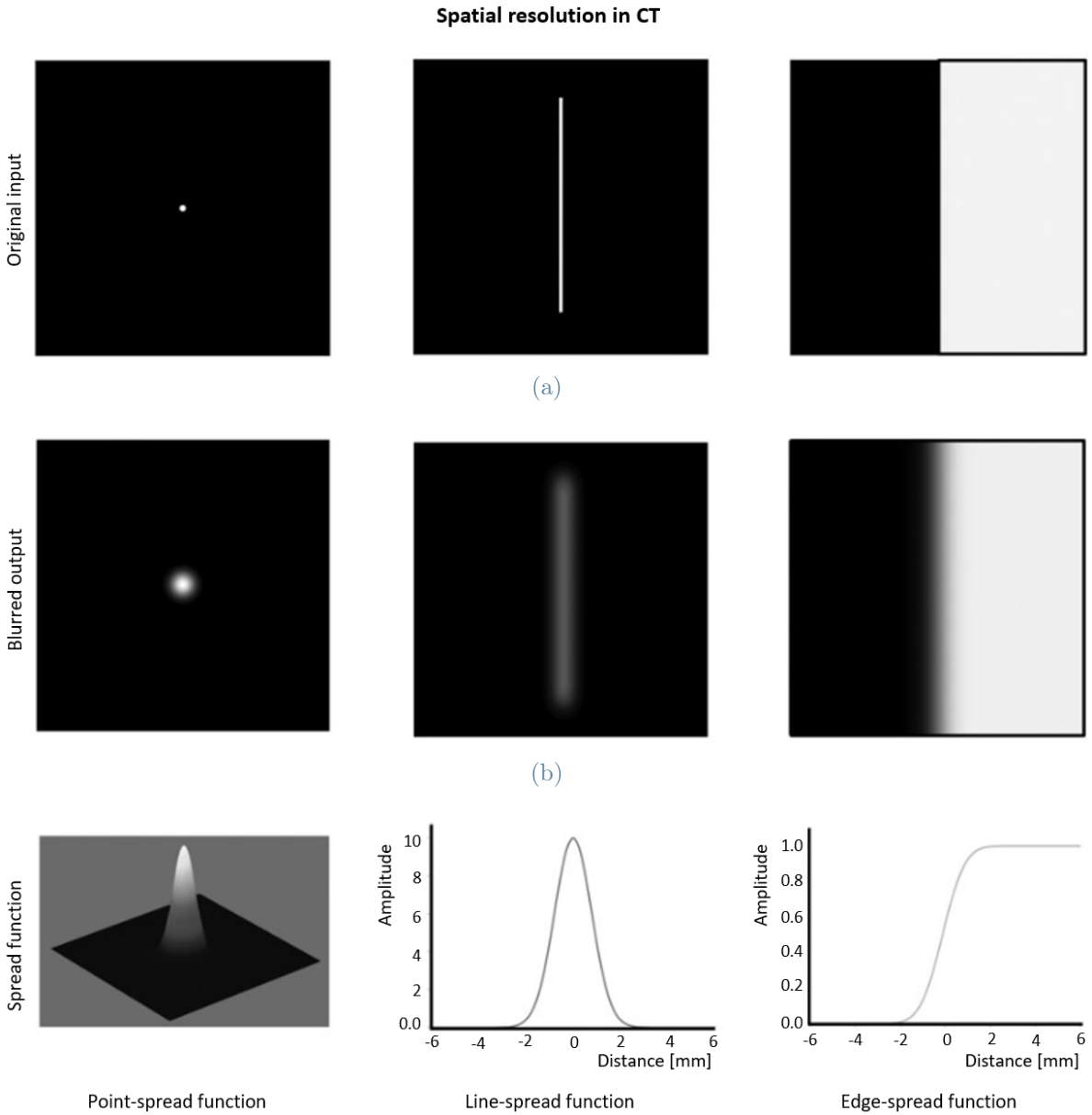

Figure 3.4: (a) Input images (left to right) defining the PSF, LSF, and ESF. (b) Simulated degraded-output images showing the raw image data used for the measurement of PSF, LSF, and ESF. (c) Graphs showing the actual PSF, LSF, and ESF. The PSF is a 2D function, while the LSF and ESF are 1D functions [58].

3.3. Noise Power Spectrum

The noise power spectrum describes the spectral decomposition of the variance in an image and hence it provides an estimation of the dependency on the spatial frequencies of

pixel-to-pixel fluctuations present in the image itself [59]. These fluctuations may be due to quantum noise, linked to the incident X-ray quanta on the detector, and any noise caused by the conversion and transmission of quanta in all stages between the detector input and output. Therefore, since it describes both the magnitude and spatial frequency characteristics of image noise, NPS plays a critical role in analyzing and optimizing imaging system performance.
There are two main methods for the calculation of the NPS when dealing with digital radiographic systems: *direct* and *indirect* method.
Let's consider a 1D detector, for sake of simplicity. Let *P(u)* be the FT of the image data, of dimension L. The NPS (*S(u)*) is then defined as:

$$S(u) = \lim_{L\to+\infty} \left\langle \frac{1}{L} \, |P(u)|^2 \right\rangle \tag{3.7}$$

where <> denotes the average over a set of images acquired under the same conditions. The NPS has the unit of length squared.
On the other hand, in the indirect method the NPS is defined as the FT of the autocovariance function *R(x)* [60]:

$$S(u) = FT[R(x)]. \tag{3.8}$$

The autocovariance function expresses the degree of correlation between neighbouring pixels and in 1D is given by the following expression:

$$R(x) = \lim_{N\to+\infty} \frac{1}{N} \int_{-N/2}^{+N/2} p(x+\tau) \; p^*(\tau) \; d\tau \tag{3.9}$$

where *p(x)* is the pixel value for a 1D image at position x, p^* is its complex conjugate.
With the advent of the Fast Fourier transform (FFT) and fast computers, indirect calculation of the NPS via the autocorrelation function has largely been replaced by the direct method [59].

There is a fundamental limitation in the usage of the NPS for image noise assessment: a stationary noise is required. Therefore, the image mean values must be constant over the whole image and the covariance must only depend on the relative position between image data points. However, this condition is hardly met in practice. Undesired noise components always lead to a systematic rise of the low-frequency spectral components. For this reason, a background detrending technique is usually performed to improve the accuracy of the estimation of the NPS for digital X-rays systems. Various methods have been proposed [61], such as the image subtraction-based method, in which the NPS is calculated from the subtraction of two images acquired in the same experimental condi-

tions and then divided by two to account for the doubling of the magnitude of the noise caused by the subtraction process.
Moreover, the NPS determination requires an infinite number of samples, but in reality, just a limited amount of data is available. The dimension of an image, which is finite, determines the sampling in Fourier space, i.e. the frequency resolution. Averaging over frames reduces the uncertainty of NPS estimation as one over the root of the number of frames. To estimate the NPS it is possible to divide each image into Regions Of Interest (ROIs), thus increasing the number of samples used. With this procedure the statistical uncertainty is reduced. The disadvantage is that the ROIs have a smaller size than the image and this reduces the frequency resolution. The smaller the ROI selected, the more samples are available and the lower the frequency resolution that can be obtained. Hence, to obtain a better estimation of the NPS a trade-off between the size and the number of ROIs should be considered.

For what concern the experimental determination of the NPS, like for the MTF, there is the international standard IEC 62220-1 [57]. The idea is to divide a portion of the uniformly exposed area of the detector into squared ROIs of 256 x 256 pixels in size each. The areas must overlap by 128 pixels in each direction (horizontal and vertical) as shown in Figure 3.5. Starting at the upper left corner, the ROI sweep through the image at 128 pixels intervals in both directions. In order to compute 1D NPS, the IEC recommends using 15 rows or columns of the 2D NPS around the axis (excluded). The direct method for the calculation of the 2D NPS is applied:

$$NPS(u,v) = \frac{\Delta x\ \Delta y}{M N_x N_y} \sum_{m=1}^{M} |FFT[I_m(x,y) - \overline{I(x,y)}]|^2 \tag{3.10}$$

where (u, v) are the spatial frequencies in the horizontal (x) and vertical (y) direction, respectively. $\Delta x, y$ and $N_{x,y}$ are the pixel spacing and the the ROI size in pixels (256 each) in the x- and y- directions, respectively. M is the number of ROIs, $I_m(x,y)$ is the m-th image and $\overline{I(x,y)}$ is the correction applied to each captured image to compensate the presence of background trends and non-linearity.

Often, the Normalized Noise Power Spectrum, NNPS, is used:

$$NNPS(u,v) = \frac{NPS(u,v)}{Q^2} \tag{3.11}$$

where Q is the photon fluence [62]. The NNPS allows to compare the noise properties of different systems and noise at different exposure levels, because the normalization results in a quantity that is independent of amplification.

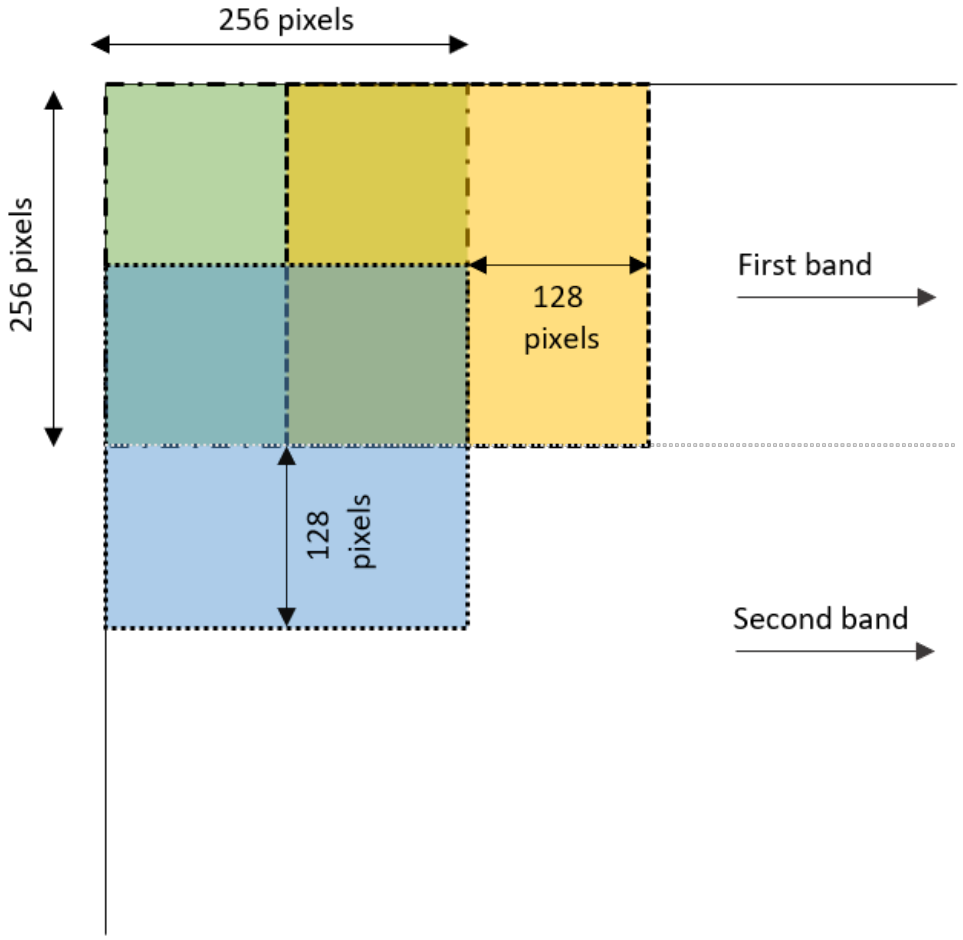

Figure 3.5: Schematic of the ROIs arrangement. The first area (green) of 256×256 pixels to be considered is the one in the upper left corner of the total analysed region. The next area (yellow) is obtained by shifting to the right-hand side the rectangular area of 128 pixels in the horizontal direction, generating a second area, which overlaps half with the first one. The next area is obtained by moving the second one by 128 pixels again. This procedure is repeated until the end of the first horizontal band. Once it is completed, again, starting from the left-hand side of the total region, the same procedure must be applied in the vertical direction. In this way, a second horizontal band is obtained.

3.4. Detective Quantum Efficiency

The detective quantum efficiency is a paradigmatic performance parameter of digital X-ray detectors which provides an indication of the ability of an imaging system to transfer the Signal-to-Noise Ratio (SNR) from its input to the output. Hence, it describes the ability of the system to effectively use the available input X-ray quanta. It is a widely used parameter since it provides an overall information including quantum efficiency, noise

and resolution. It is mathematically defined as the ratio of the output SNR squared and the input SNR squared:

$$DQE(u) = \frac{SNR^2_{out}(u)}{SNR^2_{in}(u)}. \tag{3.12}$$

In the specific case of Poissonian statistics, the SNR for a certain number of detected X-ray photons, N, is defined as the ratio between the signal (s) and the noise (σ):

$$SNR = \frac{s}{\sigma} = \frac{N}{\sqrt{N}} = \sqrt{N}. \tag{3.13}$$

The DQE can be calculated considering the following relation:

$$DQE(u) = \frac{MTF^2(u)}{NNPS(u)\ \bar{q}} \tag{3.14}$$

where $\bar{q}$ is the average number of incident X-ray quanta per unit area.

An ideal imaging system would be characterized by DQE equal to 1 at all spatial frequencies. However, in real systems a deviation from the ideal trend is always verified: the DQE decreases gradually with increasing spatial frequencies. According to Williams et al. [59], this occurs due to the increased effect of noise as a function of spatial frequency.

3.5. X-ray Computed Tomography

X-ray CT is one of the most important imaging techniques in clinical diagnostics and it allows to reveal internal details of an object in 3D and in a non-destructive and non-invasive manner.
It exploits the X-ray capability to penetrate matter to obtain a series of 2D images (projections) of the object from multiple directions. This process is usually called CT scan. It follows a computed reconstruction algorithm to create a stack of cross-sectional slices from the 2D projections of the object, resulting in a digital 3D grey-scale representation of the internal structure of the object.

Experimental configuration.The three main components of a CT scanner are the X-ray source, the sample stage and the X-ray detector. They can be exploited in different configurations according to the goal of the experiment [63]:

- When dealing with a patient, for example, it may be necessary to keep its organs motionless and hence a gantry system with source and detector rotating around the patient may be exploited. The layout of the system is illustrated in Figure 5.19a.

- To image a centimeter-sized or millimeter-sized sample, the detector and the X-ray source must be kept in a fixed position while the specimen rotates. In this case, a cone beam system can be differentiated from a parallel beam system, depending on whether the source is an X-ray tube or a synchrotron source, respectively. A representation of these configurations is shown in the Figure 5.19b and Figure 5.19c.

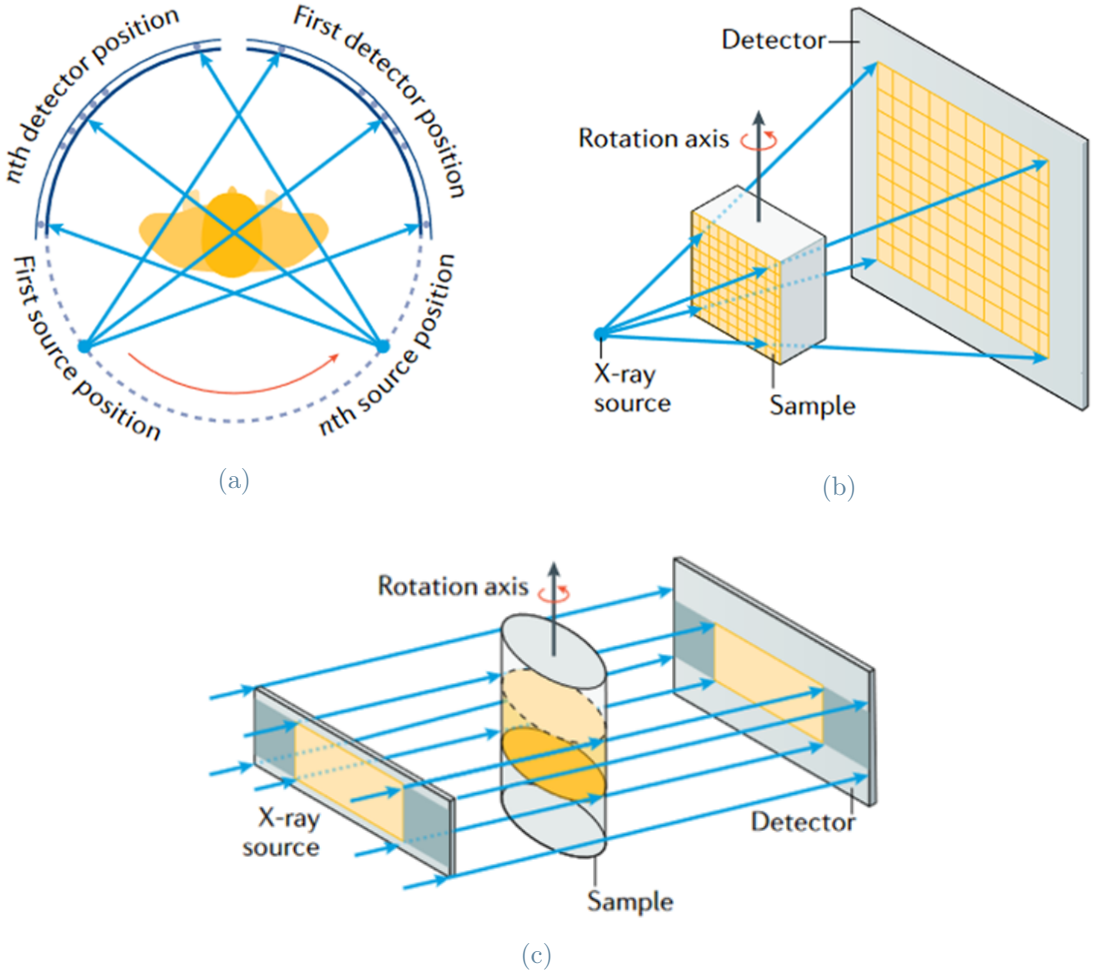

Figure 3.6: Common X-ray CT configurations. (a) Gantry system where the source and the detector rotate in tandem around the patient, animal or specimen. (b) Cone beam system typical of laboratory systems. (c) Parallel beam system geometry typical of synchrotron X-ray systems. Modified from [63].

At the ID17 beamline (ESRF) the parallel system beam geometry is exploited. Due to the fact that the X-ray source is located hundreds of meters away from the sample, the beam is highly parallel (see Section 1.3.1). As a result, this enables to obtain a reconstructed voxel size equal to the detector pixel size. Typical scan times range from sub-seconds to minutes [64]. Usually, the entire sample section is fully illuminated and remains within

the Field Of View (FOV) of the detector for all the projections and also the beam size lies within the FOV.

In Section 2.2.1 we have seen that the synchrotron X-ray source is far from being uniform and that the semiconductor detectors, such as the EIGER2, show pixel to pixel variations in sensitivity. For this reason, the already mentioned flat-field correction is performed: a projection without the sample is acquired to correct for these unwanted phenomena. Moreover, the mechanical stability of both instrumentation and specimen is very important otherwise the image obtained from the reconstruction will be blurred. For example, to avoid blurring due to thermally induced movement of the X-ray source, it is essential to provide adequate thermal stabilization of the monochromator.

When monoenergetic X-rays passes through an object, the latter experience exponential attenuation proportional to the linear attenuation coefficient (μ) of the object. In particular, for an inhomogeneous object, the transmitted intensity, I, is given by the Lambert-Beer's law:

$$I = I_0 \; e^{-\int_0^d \mu(x) \; dx} \tag{3.16}$$

where I_0 is the incident beam intensity and x is the path length inside the object. Each reconstructed slice, can be seen as a map of the linear attenuation coefficient for the respective section in the object. For materials with similar atomic numbers, the absorption contrast will be small.

Tomographic reconstruction. As already introduced, the CT projections once collected are converted into tomographic 3D image slices through a process termed reconstruction. The Radon transform provides a mathematical description of the relation between projections and slices. Various reconstruction algorithms have been developed over the years and two main classes can be distinguished: *iterative* and *analytic* methods. For what concern iterative methods, many efforts have been made to make them popular again because of their unique advantages, such as their performance with incomplete noisy data [65]. Moreover, they allow to obtain a high-quality reconstruction even if only a limited angular range or a small number of projections can be acquired. The Conjugate Gradient (CG) algorithm is one of the most important iterative algorithm [66].
However, the conventional algorithm of image reconstruction is the Filtered Back Projection (FBP) reconstruction technique, which is an analytical method. In Figure 3.7 is schematized the process of FBP on different projections of a human head. Let's consider the attenuation induced by a cross-sectional slice of the head (projection), recorded by a row of pixels of the detector. In Figure 3.7b are shown three projections, represented as a line profile, at 0°, 45° and 180°. A so-called sinogram is the image obtained by plotting the

signal from the various projections at the different angles (Figure 3.7c. In Figure 3.7d, the backprojection reconstruction algorithm takes each projection that constitutes the sinogram and mathematically projects them back along the projection angle at which they were recorded. As it can be observed from Figure 3.7e, the algorithm introduces blurring, which can be removed by applying a filter (usually a ramp filter) to the projections. A more detailed and exhaustive description can be found in Kak et Slaney work [67].

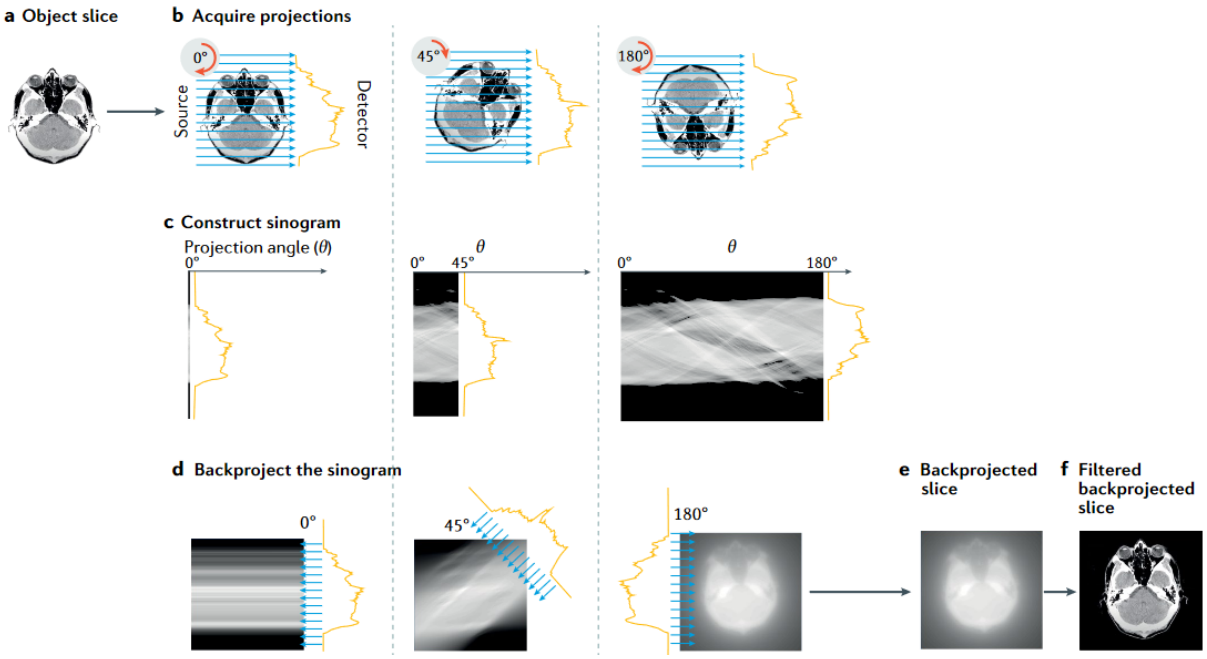

Figure 3.7: Backprojection reconstruction method for a single slice obtained by parallel beam computed tomography. (a) Original object slice: a human head where the highly attenuating features are brightest. (b) Set of projections collected at different angles. (c) Sinogram resulting from many projections. (d) Process of backprojecting the sinogram. (e) Final backprojected image. (f) Equivalent filtered backprojection image [63].

The minimum number of projections N for a tomographic reconstruction with FBP, in order not to have the formation of image artifacts, is given by:

$$N \geq \frac{\pi}{2} n_{pixel} \tag{3.17}$$

where n_{pixel} is the width of the object in pixels [68].

3.6. K-edge subtraction

As already mentioned in the previous Section, X-ray CT lacks the ability to differentiate similarly absorbing substances. This problem, for example, arises when dealing with the commonly used iodine contrast agent and calcium or simply when dealing with soft tissues, which are characterized by a similar elemental composition and a weak attenuation contrast. In order to distinguish these materials, K-edge subtraction can be exploited. It was proposed for the first time by B. Jacobson in 1953 [69] and it consists in subtracting logarithmically two CT scans acquired simultaneously (or in rapid succession) at different X-ray energies slightly below and above the K-edge of the photoelectric absorption of the material of interest or of the contrast agent. Thanks to the discontinuity in the linear absorption coefficient of the contrast agent, the difference image obtained shows the contrasted structure, while removing practically all features due to other structures (Figure 3.8).

This technique can also be used to quantify the concentration of a contrast agent injected into a patient. This can be iodine for the study of blood vessels (angiography) or xenon for the study of ventilation. With this goal, the KES technique is mainly used in the ID17 beamline.

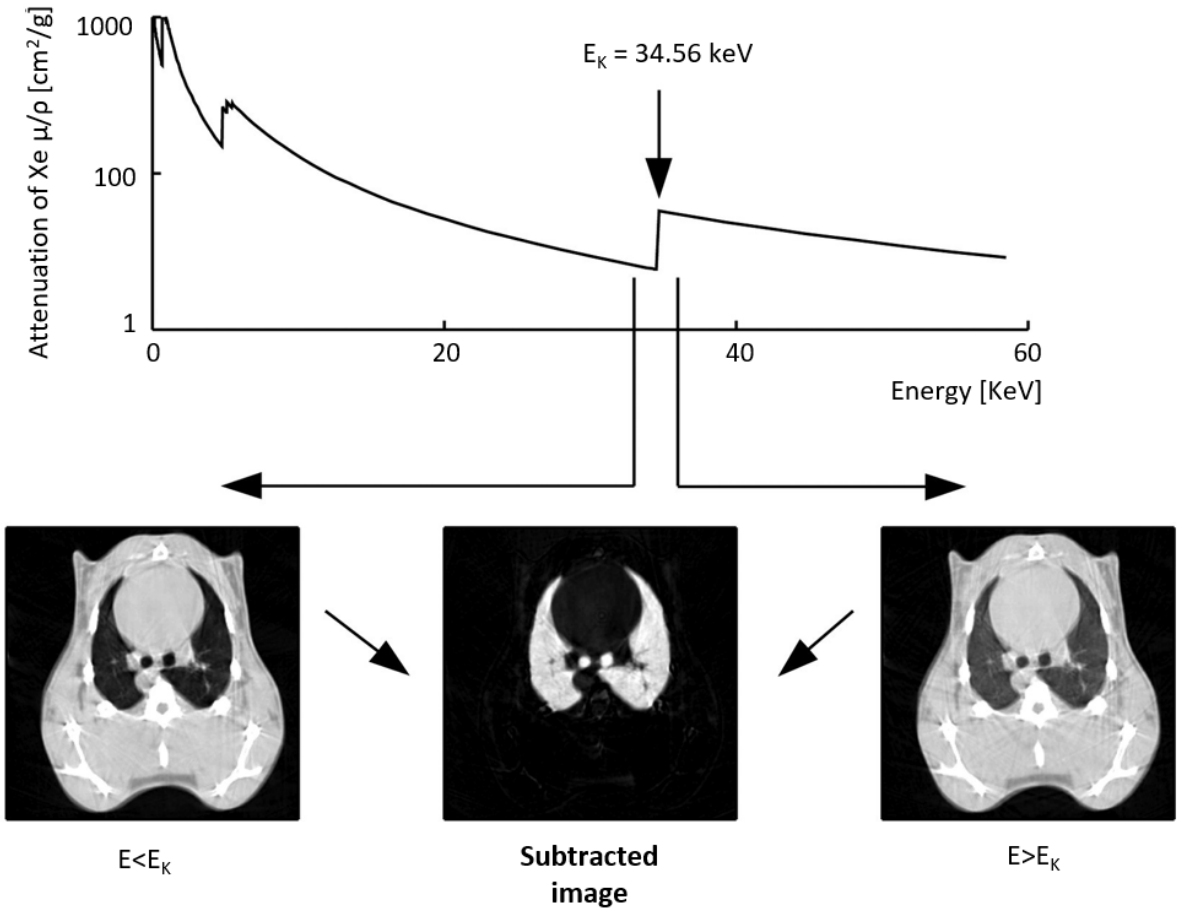

Figure 3.8: Example of KES applied to lung imaging. Two simultaneous CT images are acquired by using two X-ray beams at two different energies (E) above and below the K-edge (E_K) of xenon. Absolute quantity of the contrast agent is determined directly on any given point of a lung CT image after subtracting these two images on a logarithmic scale. Adapted from [70].

The contrast due to anatomic details of tissue and bone disappear if the difference in the X-ray beam energies is sufficiently small (see Figure 3.9).

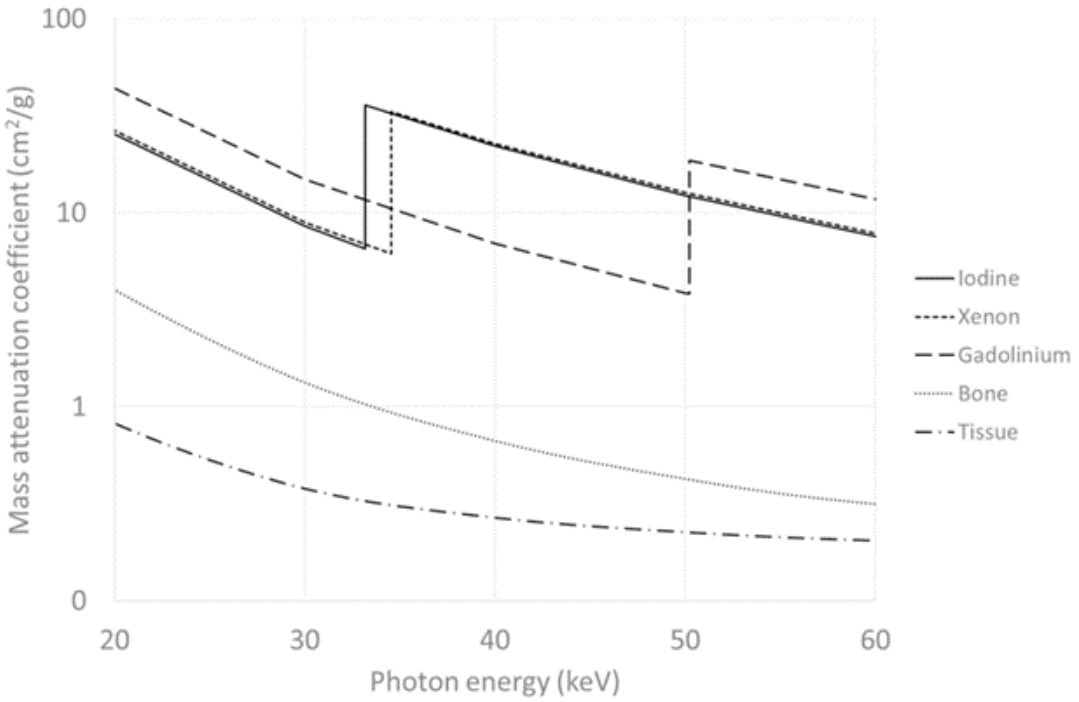

Figure 3.9: Mass attenuation coefficients of iodine, xenon, gadolinium, bone and soft tissue as a function of the photon energy [71].

KES is nowadays an established technique at synchrotron facilities, where quasi monochromatic beams from the full X-ray spectrum can be selected with energy band high enough to bracket the K-edge of the contrast agent. At the ID17 biomedical beamline at ESRF, the KES method was originally developed for human coronary angiography with iodine contrast [72, 73] and later extended to lung imaging with stable xenon gas as a contrast agent [74]. The current KES imaging set-ups are based on the use of a focusing perfect crystal monochromator of Laue-type, shown in Figure 3.10. The bent Laue crystal acts as a lens in the diffraction plane and focuses in the vertical direction the beam at the object. By placing a splitter in between the monochromator and the sample, two separate beams are produced with energy above and below the K-edge, as required by the technique. They are then detected simultaneously and separately by a dual-line solid detector [75]. Most of the synchrotron-based K-edge imaging methods exploits a horizontal fan beam, so that the sample must be scanned vertically. The possibilities and limitations of KES with synchrotron radiation have been extensively reviewed by Thomlinson et al. [76].

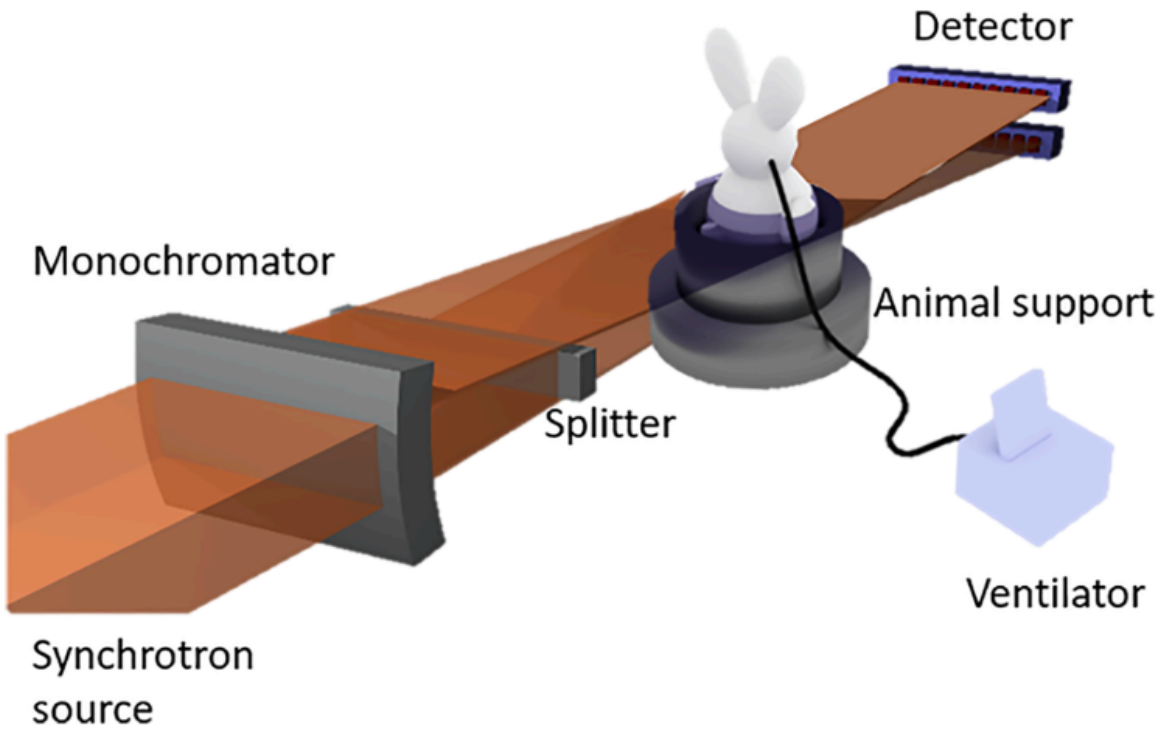

Figure 3.10: Experimental set-up of the KES method. The incident polychromatic beam is focused vertically and monochromatized by a cylindrically bent Laue crystal. Since there is a vertical energy gradient, two separate energy bands are obtained by blocking the central part of the beam. The two beams cross at the sample and are again separated at the dual line detector [71].

In particular, at ID17, the set-up is used at K-edges of particular interest in biomedicine, i.e. iodine (33.17 keV), xenon (34.56 keV), gadolinium (50.25 keV) and gold (80.72 keV), because those elements are included in biocompatible contrast agents. The mass attenuations of some of the elements just mentioned are reported in Figure 3.9.
The simultaneous image acquisition of the sample at two different energy beams bracketing the K-edge of the contrast agent allows to achieve couples of motion-free radiographs. This is an important advantage of KES imaging since, when dealing with in-vivo experiments, motions due to breathing, pulse, etc., blurs and shadows the contrast agent image.

4 | Instrumentation and Methods

The characterization of the EIGER2 detector has been distinguished into two main parts: the determination of the performances of the detector in terms of linearity, MTF, NPS and DQE and the determination of the detector stability at its startup and during a typical CT experiment. All the experiments have been conducted, as already mentioned, in the second experimental station of the ID17 beamline, where a monochromatic X-ray beam is exploited. For more information on the experimental and optical hutch of this station, please refer to Section 1.3.3.

In this chapter the experimental set-up and the methods exploited to perform the above measurements are presented. All the measurements reported below have been first acquired in the energy range 26-51 keV, which is usually exploited in typical imaging experiments. Then, some of the measurements have been performed at higher energy, 80 keV, in view of possible medical imaging applications related for example to the presence of the K-edge of gold at this energy. All DECTRIS corrections (Section 2.3.1) have been applied in all the experimental measurements presented below unless otherwise indicated. The analysis of the acquired data have been performed exploiting Root (version 6.24/06) [77], Python (version 3.8.8) and Excel.

4.1. EIGER2 performances

In Figure 4.1 is represented the experimental setup used for the determination of the linearity, the MTF, the NPS and the DQE. The detector has been appropriately placed on a stable bench and connected to the cooling and dry air system to ensure its optimal operation (see Section 2.3.2). Vertical and horizontal translation stages are used to align the detector with the beam and to select the region of interest of the sensor to be irradiated. Just in front of the detector a shutter has been positioned in order to protect it from unwanted exposures when not in use. Facing the detector a bench is located, in which a tungsten (W) blade for the calculation of the MTF or an Ionization Chamber (IC) for the determination of the photon flux can be opportunely placed. In particular, these devices are installed on suitable motorized systems so that to be correctly positioned

for the experiments. These motors are translation stages, which enable movements in the three directions of space. Moreover, a cradle is used to align the tungsten slit for the slanted edge method (Section 3.2). However, due to some mechanical constraints present during the commissioning phase of the detector, only one module of the EIGER2 could be tested. In particular, the analysis has been performed on a single chip, the smallest unit of the detector. A chip-to-chip characterization is planned, but no differences are expected since the sensor properties should be homogeneous.

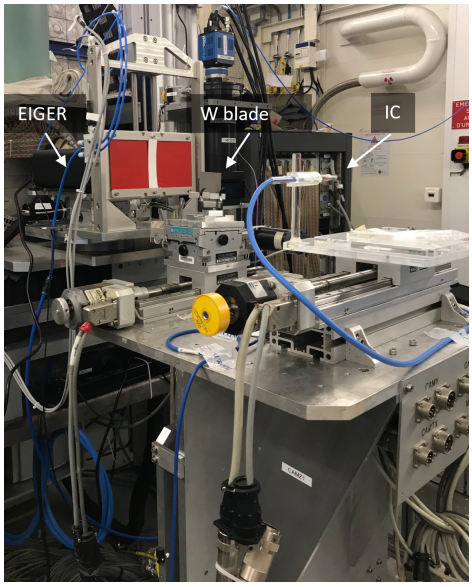

(a) Picture of the main part of the experimental setup in EH2 at ID17 beamline.

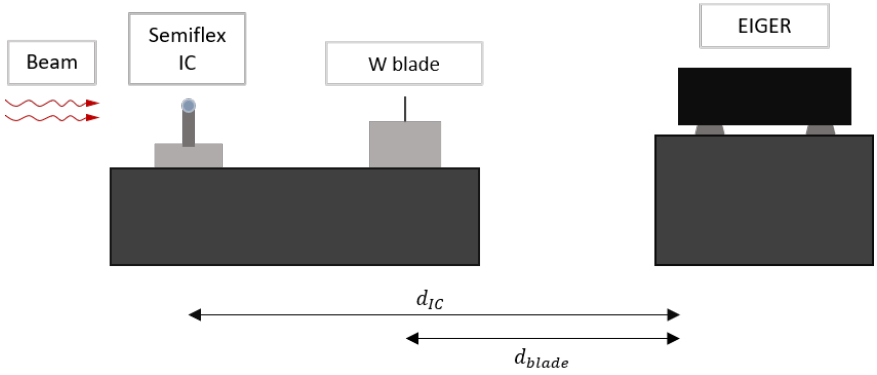

(b) Schematisation of the experimental setup.

Figure 4.1: Representation of the experimental setup for the determination of the EIGER performances. The IC for the calculation of the incoming flux, the tungsten blade for the determination of the MTF and the EIGER2 detector are highlighted. d_{blade} and d_{IC} are the distances between the detector and the tungsten blade and the detector and the IC respectively.

4.1.1. Linearity

For what concern the linearity measurement, the idea is to study whether there is a linear relationship between the number of detector counts and the incident photon flux. Hence, the goal is to determine the flux at the detector Ψ_{EIGER}, knowing the incident photon flux Ψ_{PTW}:

$$\Psi_{EIGER} = m\Psi_{PTW} + q \tag{4.1}$$

where m and q are respectively the slope and the intercept of the linear function.

To perform an in-depth analysis, the count-rate correction applied by DECTRIS has been studied by acquiring data with both on and off correction.
The incoming photon flux has been calculated using a calibrated standard therapy chamber for radiation therapy, positioned on a bench at a distance d_{IC} from the detector (see Figure 4.1b). In particular, the ionization chamber exploited is the PTW Semiflex tube ionization chamber TW31010 (PTW, Freiburg, Germany), which is shown in Figure 4.2. It is calibrated in terms of absorbed dose to water. The chamber is characterized by a small size allowing reasonable spatial resolution and a large sensitive volume of 0.125 cm^3 enabling precise dose measurements. The approximately spherical sensitive volume results in a flat angular response and a uniform spatial resolution. Specific characteristics of the ionization chamber can be found in [78].

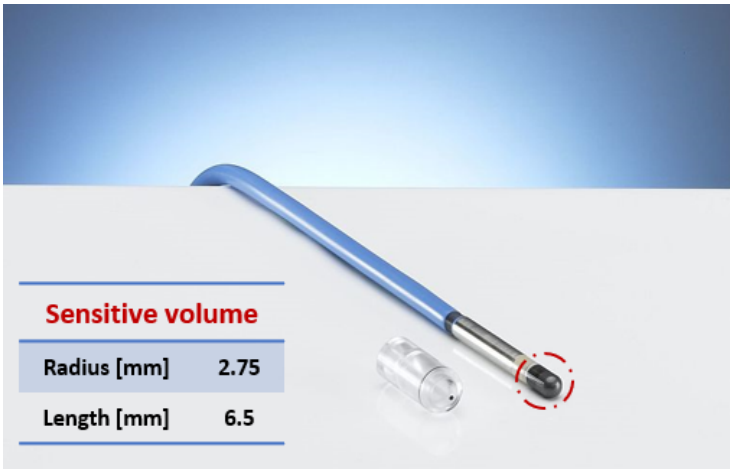

Figure 4.2: Semiflex chamber type 31010 used for the dosimetry calculations. The dimensions of the sensitive volume are reported. Adapted from [79].

According to standard dosimetry and reference calibration protocols of ionization chamber, the latter should be exposed to a uniform beam. However, this condition can hardly be met at the synchrotron since, as already mentioned, the vertical dimension of the

beam is smaller than the dimensions of a typical thimble chamber (see values reported in Figure 4.2). For this reason, the so-called *scanning technique* has been exploited. It consists in having the integration of the dose rate while scanning vertically across the beam the ionization chamber with a constant and well-known speed. The working principle of this technique is represented in Figure 4.3. Prezado et al. [80] have shown that this is equivalent to measuring the dose deposited with a uniform irradiation.

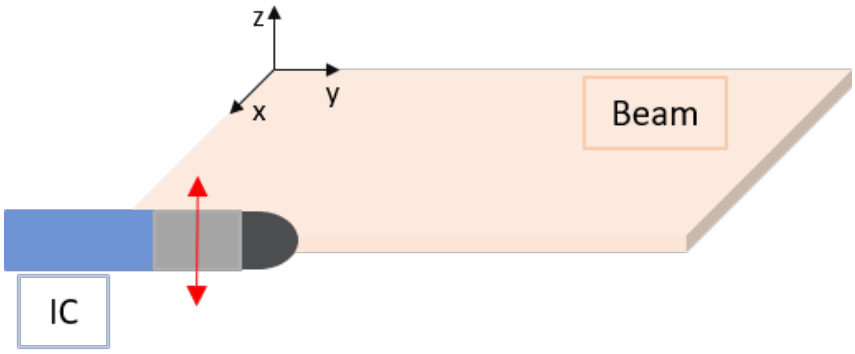

Figure 4.3: Working principle of the scanning technique. The ionization chamber is moved at a constant speed along the z axis through the synchrotron beam.

From the dose value obtained with the PTW (D_{PTW}), knowing the scanning velocity (v_{scan}), the number of scans (n_{scan}), the ring current at the moment of the measurement with the PTW (I) and the vertical size of the beam (δ_v), it is possible to obtain the dose rate normalized to the ring current:

$$D_{rate} = \frac{D_{PTW} v_{scan}}{I n_{scan} \delta_v}. \tag{4.2}$$

To compare the number of incident photons and the number of detector counts, the dose rate must be multiplied by the integration time (t_{int}) of the detector. The dose (D) can then be converted to incident fluence with the expression:

$$\Psi_{PTW} = \frac{D I' k_{air}}{\mu_{en_{water}} E} \tag{4.3}$$

where $\mu_{en_{water}}$ is the mass energy-absorption coefficient in water, E is the energy of the impinging photons and I' is the ring current value during image acquisition. k_{air} is a parameter that takes into account the absorption in air between the PTW and the detector (d_{IC}) and it is derived as follows:

$$k_{air} = e^{-\mu_{air} d_{IC}} \tag{4.4}$$

where μ_{air} is the mass attenuation coefficient in air.

Data has been acquired for energies (E) in the range 26-51 keV and at 80 keV, enabling and disabling the count-rate correction applied by DECTRIS. In particular, the dataset at 26-51 keV was acquired by the ID17 team before the start of this thesis work.
In Table 4.1 just the main parameters concerning the scanning technique and the experimental layout are reported. The incoming photon flux was tuned using PMMA (Poly-Methyl MethAcrylate) absorbers. Higher thicknesses correspond to lower fluxes and vice versa. The values of the of $\mu_{en_{water}}$ and μ_{air} exploited in the above formulas has been retrieved by NIST [81, 82].

E [keV]	**PMMA [cm]**	v_{scan} **[mm/s]**	n_{scan}	δ_v **[mm]**	d_{IC} **[cm]**
26	0-10	2.5	5	3.15	75
28	0-10	2.5	5	3.15	75
30	0-10	2.5	5	3.15	75
35	0-15	2.5	5	3.15	75
51	0-15	2.5	5	3.15	75
80	12-25	2.5	5	4.8	45

Table 4.1: Experimental parameters exploited for the linearity measurement. In particular, for each energy (E) and thickness of the attenuator (PMMA), are reported the scan velocity (v_{scan}), the number of scans (n_{scan}), the vertical beam size (δ_v) and the distance between the detector and the IC (d_{IC}).

In particular for the energy range 26-51 keV, 10 white-fields (wf) images have been acquired for each thickness of the attenuator. In this thesis, as already mentioned, wf image (or flat-field image) means an image registered without a sample in the X-ray beam. Specifically 5 wf images by enabling the DECTRIS count-rate correction and the other 5 by disabling the correction have been acquired. On the other hand, 2 wf images have been acquired for 80 keV for each attenuator. Again, 1 wf image is acquired with the count rate correction enabled and the other with the correction disabled. Having a certain number of flat-field images makes it possible to increase the statistics; however, at the energy of 80 keV only one image has been acquired, as the total exposure of the detector had to be reduced to avoid polarization phenomenon. Moreover, to prevent this phenomenon, small attenuator thicknesses and hence high fluxes have been avoided. The integration time, namely the time of exposure during the acquisition of one projection, has been set to 10 ms for all the energies.

The flux measured by the detector has been therefore derived by dividing the average counts per pixel from the wf image by the pixel surface (75×75 µm^2) of the detector.
To study the linearity of the detector, a linear fit between the flux measured by the detector and the PTW has been performed with the software ROOT [77].

4.1.2. MTF

For the calculation of the MTF, the ISO standard guidelines (see Section 3.2) can not be followed since the vertical dimension of the beam is so narrow that it is not possible to consider a ROI of required dimensions. The crucial point in the determination of the MTF is the fineness of the sampling signal: if the spatial frequencies are not sampled closely enough aliasing will occur. To overcome aliasing effects, the slanted-edge method has been exploited (refer to Section 3.2). It consists in imaging an edge onto the detector, slightly tilted of an angle θ with regard to the rows. The ESF is extracted by projecting data along the edge. The working principle is schematically illustrated in Figure 4.4. Once the uniformly spaced ESF is obtained, it is differentiated to obtain the LSF. Finally, the MTF is calculated as the modulus of the discrete Fourier transform of the LSF using a discrete spatial frequency interval given by $1/N$, where N is the number of sample points of the ESF. The values of the MTF later presented, have been normalized with respect to the MTF at zero frequency.

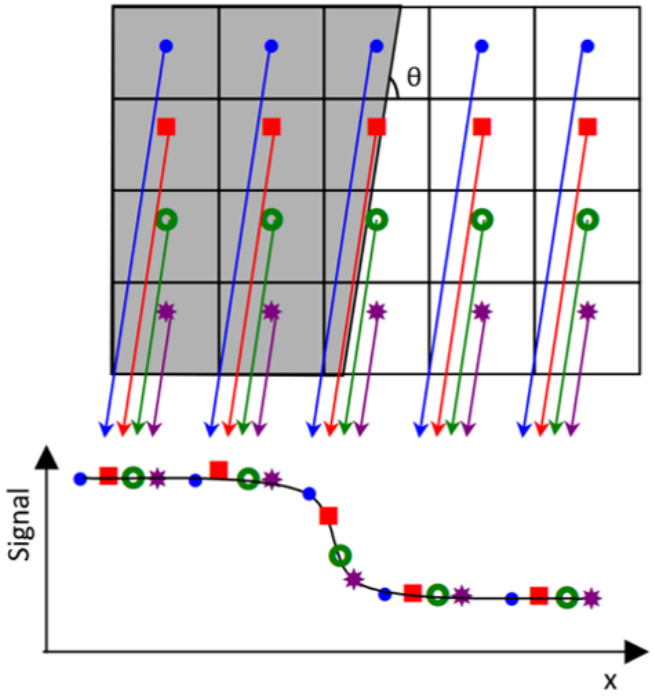

Figure 4.4: Projection of data along the edge according to the slanted-edge method. [83]

In this thesis work, for the determination of the MTF, a tungsten blade of thickness 0.5 mm and purity 99.95% has been chosen. It has been properly positioned in front of the detector at a distance d_{blade} as shown in Figure 4.1b.
Experimentally, the MTF has been calculated for the energies and attenuator thicknesses reported in Table 4.2. Hence, for the energy range 26-50 keV the MTFs have been calculated for two conditions of flux (low and high), while for the energy of 80 keV just the low flux condition has been performed in order to avoid, as already mentioned for the calculation of the linearity, the phenomenon of polarization.
To have a more immediate interpretation of the results, high and low flux will be indicated in the graphs, without specifying the corresponding thickness of the attenuators as reported in the table below. The thickness of the attenuator was chosen to obtain 1M counts/pixel/s and 3M counts/pixel/s for low and high flux, respectively.

E [keV]	PMMA [cm]	Flux
26	1	High
	4	Low
30	2	High
	5	Low
33	3	High
	7	Low
50	2	High
	7	Low
80	18	Low

Table 4.2: Experimental parameters for the MTF determination. The energies and the thicknesses of the Plexiglas attenuators are reported. For a more immediate interpretation the label "high" (3M counts/pixel/s) and "low" (1M counts/pixel/s) flux has been attributed to the thicknesses of the attenuators.

One wf image and two images with the tungsten blade for each energy and for each attenuator thickness have been acquired with an integration time of 10 ms. The wf image has been used to normalize the image of the blade for the beam non-uniformity while the two images with the blade have been used for the determination of the MTF in both directions: horizontal and vertical.

A custom-made code written in Python has been used to estimate the ESF in both the

horizontal and vertical direction. A description of the procedure implemented in the code follows:

1. Estimate the location of the edge by fitting a logistic function to the data row by row or column by column, depending on the orientation (vertical/horizontal) of the ESF to be measured:
$$f(x) = A\left[1 - \frac{1}{1 + e^{\frac{x-\mu}{\sigma}}}\right] \tag{4.5}$$
where x is the pixel location for column (or row), μ the center value of the curve and σ the width of the sigmoid curve and A a normalisation coefficient. μ is considered a rough estimate of the position of the tungsten blade. In order to do that, an appropriate rectangular ROI straddling the edge, as shown in Figure 4.5, has been selected.

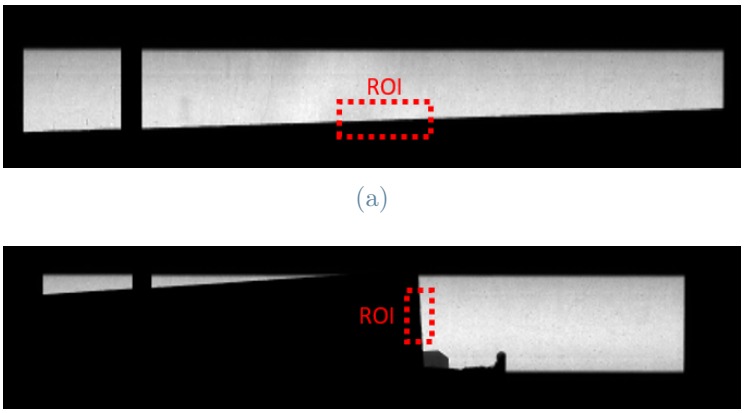

(a)

(b)

Figure 4.5: Flat-field images for the (a) vertical and (b) horizontal determination of the ESF. The ROI straddling the edge is shown.

2. Fit the values regarding the position of the edge obtained in the previous step with a linear fit to get a better estimation of the edge position. In this way it is possible to determine the distance of each pixel from the edge.

3. Align all the ESF profiles obtained by shifting each point by 1/M, where M is the number of rows/columns required for the edge to move one column/row respectively.

However, due to the limited vertical beam size, it has not been possible to get enough statistics for the horizontal MTF and hence in the next chapter, only the results for the vertical MTF have been reported. For sake of simplicity, the term vertical MTF will not be continuously specified in this chapter and in the following one but it will be implied.

Before going to analyze in detail the fit model used for the determination of ESF, it is

necessary to briefly resume what happens when a X-ray photon interacts on the detector. As shown in Figure 4.6, when the photon impinges on the detector, charges (electrons and holes) are released and a charge cloud is created. The latter drifts towards the anode and gradually spreads out with a Gaussian profile.

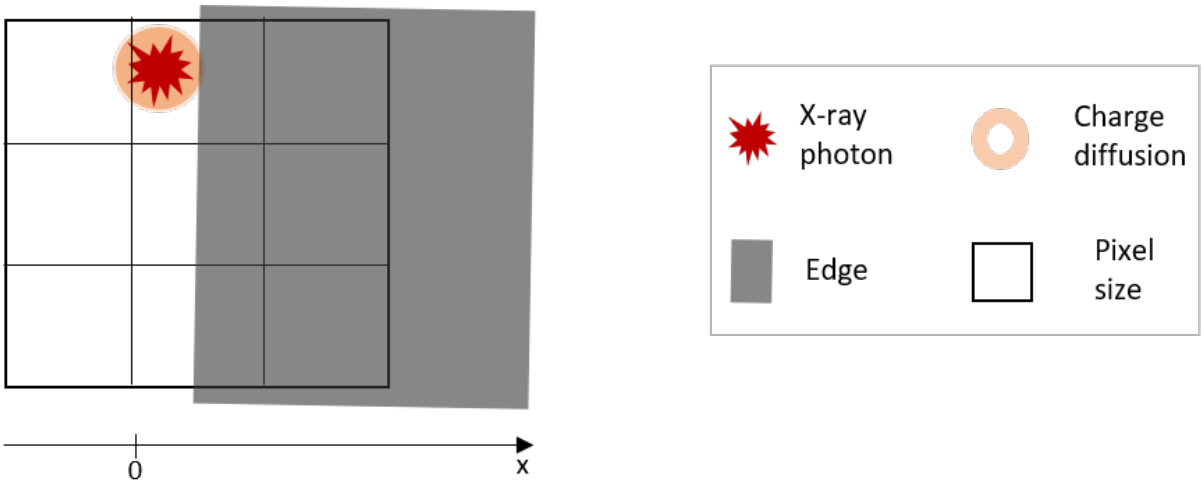

Figure 4.6: Simplified representation of a portion of the active area of a pixelated detector with an edge superimposed, showing the interaction of an X-ray photon. The phenomenon of charge diffusion is depicted.

Usually, to fit the ESF, the ERror Function (ERF) is used. It takes into account the primary absorption of the photon, modeled with a delta function, the diffusion of the charge (Gaussian profile - charge sharing phenomenon) and the presence of the edge, modeled by an edge response (Figure 4.7).

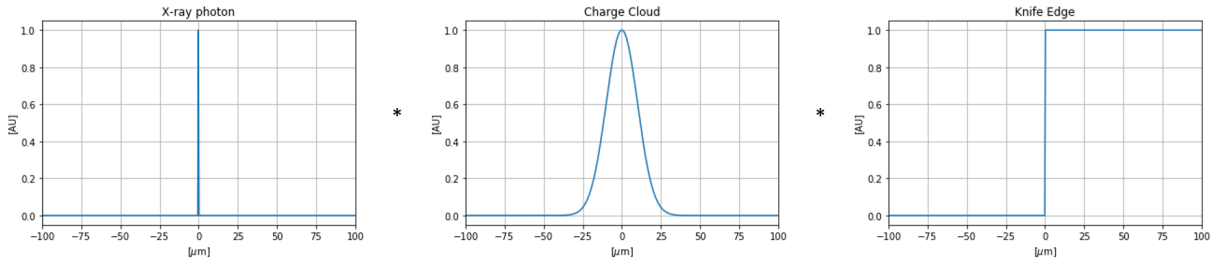

Figure 4.7: The ESF can be fitted by the ERF by performing the convolution between a Dirac delta (primary absorption of a photon), a Gaussian profile (diffusion of the charge) and an edge response (physical presence of an edge). This representation is purely explanatory: the functions corresponds to a detector of pixel size of 100 µm. Image courtesy of P. Busca from Detector Group of the ESRF.

However, this model is not so accurate for our single photon counting detector as it does not take into account certain important parameters, such as the physical size of the pixel. Paolo Busca and Marin Collonge from the Detector group of the ESRF, in an unpublished work, compared the results obtained for the determination of the MTF using two models: the error function and the error function convolved with a box function to account for the physical size of the pixel. In particular, the data were acquired with an EIGER2 detector. They found for ESF and MTF comparable results between the two models while for LSF the results were clearly better for the second model. Similar approach has been followed by Zambon et al. [84] by considering the physical dimension of a pixel of a single photon counting pixelated detector. In particular, they took into account the 2D effects of the charge sharing and of the electronic noise. Their fitting model is based only on geometrical and physical parameters such as the pixel size, the charge cloud size at the pixel depth and the total electronic noise of the front-end circuitry. One of the main limitations of this work is that fluorescence is not taken into account, as according to them a Monte Carlo approach is needed.
The tested function in this thesis has been developed in collaboration with the Detector and Electronics Group of the ESRF Instrumentation Services and Development Division. This new fitting model, in addition to the parameters considered in the ERF model, takes into account the physical size of the pixel, modelled with a box function and the physical phenomenon of fluorescence (see Section 2.1.4). Fluorescence can give charge tails at high distance from the photon's point of impact and so the signal projected on the x-axis ($p(x)$) can be modelled by the superposition of a Dirac delta for the primary absorption and a symmetric exponential for fluorescence:

$$p(x) = a\delta(x) + be^{-\frac{|x|}{c}} \tag{4.6}$$

where a, b and c are coefficients. Let's define α the ratio between b and a. The higher the contribution of fluorescence, i.e. for energies close to the K-edges of Cd and Te, the higher the α parameter and vice versa. A representation of the fluorescence phenomena and of the resulting signal is shown in Figure 4.8.

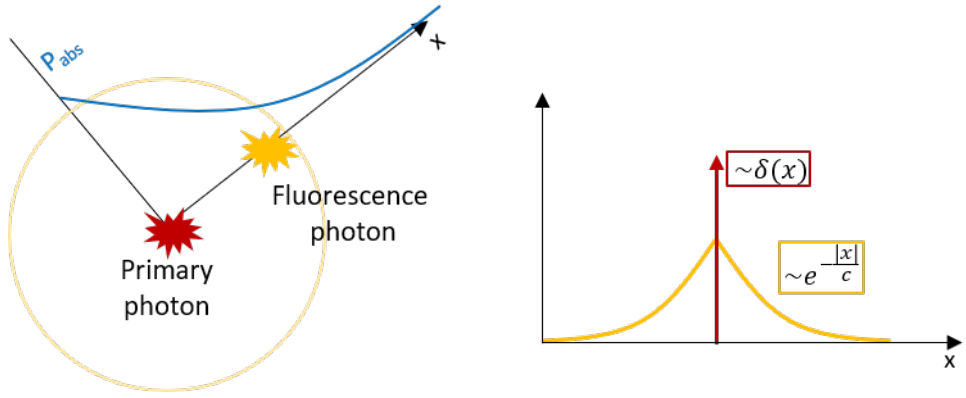

(a) (b)

Figure 4.8: (a) Simplified representation of the fluorescence phenomenon. The primary photon impinging on the detector interacts through the photoelectric effect leaving an atom ionized. As a consequence, a fluorescence photon can be emitted on 4π and it will be absorbed with an exponential probability. (b) The projection of the absorption profile on the x-axis is given by a Dirac delta for the primary absorption of the X-ray photon and two exponential tails for the fluorescence contribution.

Hence the final model is given by the convolution of the various contributions. In Figure 4.9a is depicted the fitting model exploited for the ESF in absence of fluorescence, while in Figure 4.9b the model used in presence of fluorescence is represented.

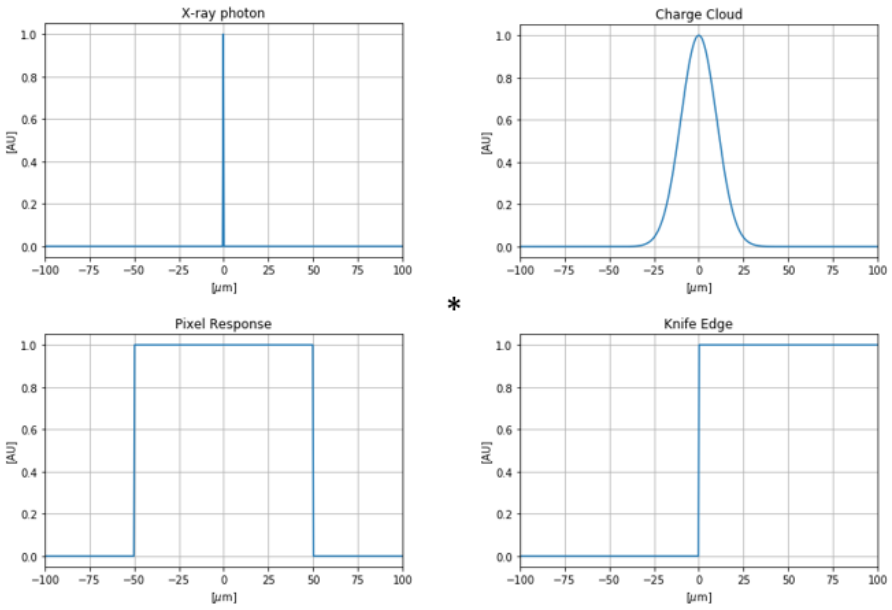

(a) ESF fitting model with no fluorescence phenomenon

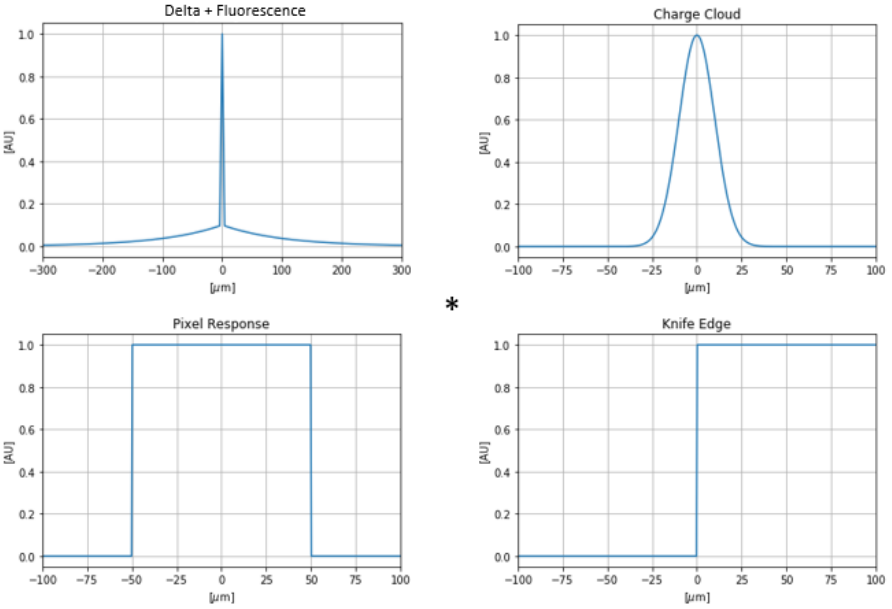

(b) ESF fitting model with fluorescence phenomenon

Figure 4.9: Fitting model for the determination of the ESF. In the absence of fluorescence phenomenon, (a) the model is given by the convolution of a Dirac delta (primary absorption), a Gaussian profile (charge diffusion), a box function (physical dimension of a pixel) and an edge response (slanted edge). When a fluorescent photon is created, (b) the model is given by the convolution of the functions just mentioned but to the Dirac delta a symmetrical exponential function is added. This representation is purely explanatory: the pixel size is 100 µm as opposed to the 75 µm required in this thesis. Image courtesy of P. Busca of the ESRF Detector Group.

It is worth defining the 1D function along the x-axis for the Gaussian distribution (approximated) used in the model to describe the diffusion of the charge cloud:

$$g(x) = e^{-0.5\left(\frac{x}{\sigma_{diff}}\right)^2} \tag{4.7}$$

where σ_{diff} quantifies the diffusion of charge. The latter is given by:

$$\sigma_{diff} = \sqrt{2Dt_d} \tag{4.8}$$

where D is the diffusion coefficient and t_d the drift time [21]. The latter can be computed using [36]:

$$t_d = \frac{d}{\mu \frac{V_{bias}}{z_0}} \tag{4.9}$$

where d is the detector sensor thickness, V_{bias} the voltage applied to the detector (400 V) and z_0 the distance between the point of interaction and the anode. The latter can be calculated by taking into account that an X-ray photon is absorbed at a mean depth in the material of $1/\mu(E)$, where $\mu(E)$ is the already defined linear attenuation coefficient. Thus, for a detector whose anode is on the opposite side of the crystal from the entrance side z_0 can be defined as:

$$z_0 = d - 1/\mu(E) \tag{4.10}$$

4.1.3. NNPS

Even for the NPS, it is not possible to follow the ISO guidelines as the beam size is limited and the sensor exposure is not uniform since we have a Gaussian profile of the beam.

Experimentally, 1000 wf images have been acquired continuously for different energies, with an integration time of 10 ms. In particular, the energies and fluxes tested are reported in Table 4.3. As for the MTF, the thickness of the attenuator was chosen to obtain 1M counts/pixel/s and 3M counts/pixel/s for low and high flux, respectively.

E [keV]	PMMA [cm]	Flux
26	1	High
	4	Low
30	2	High
	5	Low
33	3	High
	7	Low
50	2	High
	7	Low
80	18	Low

Table 4.3: Experimental parameters for the NPS determination. The energies and the thicknesses of the Plexiglas attenuators are reported. For a more immediate interpretation the label "high" (3M counts/pixel/s) and "low" (1M counts/pixel/s) flux has been attributed to the thicknesses of the attenuators.

Theoretically, for the calculation of the NPS, a stationary noise is required. However, since this condition is hardly met in practice, as already explained in Section 3.3, a detrending technique is needed. If the average of the images is subtracted from the individual images, as shown in Figure 4.10, the resulting detrend is not perfect and its effectiveness changes over time.

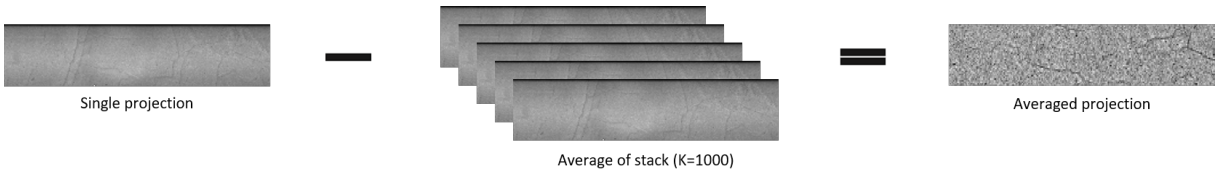

Figure 4.10: Schematisation of the detrend technique for the calculation of the NPS. The average of the thousand acquired projections (K) is subtracted from each single projection.

The reason for this, as deeply analysed in Section 2.2.1, is due to the instability of the CdTe sensor. To overcome this problem, a different background estimate is made for each wf image acquired, i.e. the projections are denoised using the Savitzky-Golay filter [85, 86]. In this way, an instant-by-instant background correction is performed.
The Savitzky-Golay filter is a low pass filter which consists in filtering successive subsets of adjacent data points with a low degree polynomial by the method of least squares.

It allows to increase the SNR without deforming the signal. This smoothing technique has been extensively used in various research fields, such as biomedical signal processing [87, 88] and spectroscopy [89], due to its analytical and computational simplicity.

Once these first steps are performed, the NPS is calculated as the 2D Fourier transform of noise. In this thesis, the NNPS has been calculated by multiplying the NPS for the photon fluence calculated with the semiflex IC and normalizing it for the counts squared. In this way, the NNPS assumes the most immediate meaning of the ratio of SNR_{in}^2 and SNR_{out}^2 at zero frequency.

In particular, just the vertical NNPS has been calculated. This choice was made for reasons of time and also because, since the MTF could only be calculated vertically as explained in the previous section, the subsequent measurement linked to the DQE would only be possible vertically.

4.1.4. DQE

To conclude this experimental part related to the determination of the performances of EIGER2 X 1M-W CdTe, the DQE has been calculated. It has been computed for 1D spatial frequencies in the vertical direction by dividing the vertical MTF and the vertical NNPS at each spatial frequency.

4.2. EIGER2 stability

This second experimental part is devoted to the determination of the stability of the EIGER2 detector during its initialization and during a typical tomographic experiment. For what concern the setup, again EIGER2 is placed on a stable bench and connected to the cooling and dry air system to ensure its optimal operation (see Section 2.3.2). In front of it a shutter is placed to protect it from unwanted exposures when not in use.

4.2.1. At startup

Before each measurement the detector should be initialized through an High Voltage (HV) reset. When the detector is initialized the bias on the CdTe sensor is reset and the operator needs to wait for the sensor to stabilize. To evaluate this stabilization time 8 consecutive HV resets were performed, waiting one hour between one and the other. This measurement was performed without irradiation and during each hour the leakage current of the detector was recorded with a sampling rate of one per minute. In particular, the leakage current was saved by the software running the detector which is able to produce

a log file. A schematic representation of the procedure is illustrated in Figure 4.11.

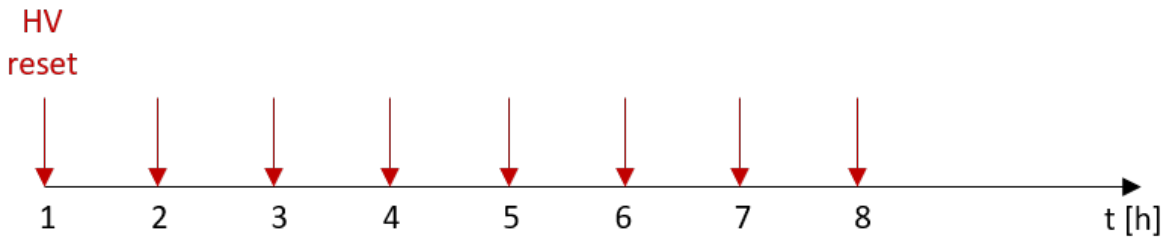

Figure 4.11: Schematisation of the procedure for the calculation of the EIGER2 stability at startup. 8 HV resets are performed and 1 hour is waited between each one during which the leakage current is acquired.

4.2.2. During a CT scan

The purpose of this experiment was to verify if the detector reaches stability during irradiation in a time compatible with a tomographic scan and to find out if repeated tomographic scans, a classical case of medical imaging experiment, are reproducible or not. All DECTRIS corrections were enabled, as it would have been done in a real experiment.

Two different energies have been tested, 33 keV and 50 keV, and for each energy two conditions of flux, low and high, have been studied by opportunely modifying the thickness of the Plexiglas attenuators. The high flux was taken in the limit of linearity ($<$ 1M counts/pixel/s), determined from the results of the previous experimental set of measurements. The low flux was around 150k counts/pixel/s.

The experimental procedure, which is schematised in Figure 4.12, consists of:

1. setting the energy and the flux,
2. performing an HV reset and waiting 1 hour (detector stabilization),
3. continuously irradiating for 1 minute during which 1 wf image is acquired every 10 ms with 10 ms integration time,
4. waiting a time called T_{sleep}, which simulates a dead time between consecutive tomographic scans.

Steps 3 and 4 must be repeated three times. The whole procedure is instead repeated for each combination of energy, flux and varying T_{sleep} (see Table 4.4). Initially data were acquired for relatively short T_{sleep}: 1 and 5 minutes (Table 4.4a). However, in light of the results obtained with these times, it was decided to enlarge the dataset considering

longer T_{sleep} times: 10 and 20 minutes (Table 4.4b). For reasons of time, data with longer T_{sleep} were only acquired at an energy of 33 keV. The three irradiations will be indicated as CT1, CT2 and CT3.

Since the ring current, and therefore the intensity of the impinging flux, changes with time, it is necessary to record the storage ring current to interpret the time dependency of the counts of the detector. However, it was not possible due to an error in the acquisition macro. Given the impossibility to solve the error in a time frame compatible with the time allocated for the experiment, only the current at the beginning and at the end of the radiation minute was possible to acquire.

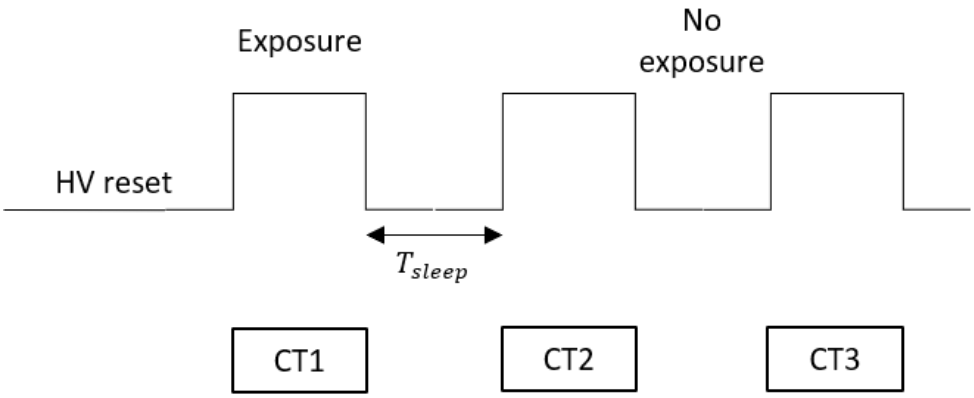

Figure 4.12: Schematisation of the procedure for the determination of the EIGER2 stability during a CT scan. Initially an HV reset is performed and 1 hour is waited so that the detector stabilises. This is followed by three irradiations of 1 minute each, called respectively CT1, CT2 and CT3, interspersed with a variable time period called T_{sleep} where no irradiation is performed.

E [keV]	PMMA [cm]	Flux	T_{sleep} [min]
33	10	High	1
			5
	16	Low	1
			5
50	12	High	1
			5
	18	Low	1
			5

(a)

E [keV]	PMMA [cm]	Flux	T_{sleep} [min]
33	10	High	10
			20
	16	Low	10
			20

(b)

Table 4.4: Experimental parameters for the determination of EIGER2 stability during a CT scan. The energies, the thicknesses of the Plexiglas attenuators and the time in between successive irradiations (T_{sleep}) are reported. For a more immediate interpretation the label "high" and "low" flux has been attributed to the thicknesses of the attenuators.

5 | Results

In this chapter, the main results obtained for the characterization of the hybrid single photon counting detector EIGER2 X CdTe 1M-W are presented. The same structure adopted in the previous chapter regarding the methods and instrumentation is kept. In the first part the results concerning the determination of the performances of the detector in terms of linearity, MTF, NPS and DQE are reported, while in the second part the results related to the determination of the detector stability at its startup and during a typical CT experiment are presented. In some cases the results for the energy of 80 keV are separated from those obtained for the low energy range 26-51 keV. The characterisation of the detector at high energy was in fact started at a later stage because of the fear of damage to the sensor itself.
All graphs presented below have been obtained using Python codes, unless otherwise specified.

5.1. EIGER2 performances

5.1.1. Linearity

For what concern the linearity measurement, the idea is to determine the flux at the detector, knowing the incident photon flux (see Equation 4.1). To determine the incoming photon flux the so-called scanning technique, deeply explained in Section 4.1.1, has been exploited. In Table 5.1 are reported the flux values for each energy obtained with the PTW Semiflex ionization chamber.

Flux PTW [ph mm^{-2} s^{-1}]					
26 keV	**28 keV**	**30 keV**	**35 keV**	**51 keV**	**80 keV**
4.43×10^6	7.97×10^6	1.78×10^6	8.80×10^6	1.14×10^7	9.58×10^6
6.81×10^6	1.56×10^7	2.52×10^6	1.20×10^6	1.46×10^7	1.14×10^7
1.05×10^7	1.69×10^7	3.60×10^6	1.62×10^6	1.85×10^7	1.40×10^7
1.57×10^7	2.45×10^7	5.02×10^6	2.20×10^6	2.36×10^7	1.78×10^7
2.38×10^7	3.57×10^7	7.18×10^6	2.97×10^6	3.00×10^7	2.17×10^7
3.61×10^7	5.23×10^7	1.02×10^6	4.05×10^6	3.82×10^7	2.67×10^7
5.51×10^7	7.68×10^7	1.45×10^6	5.46×10^6	4.86×10^7	3.27×10^7
8.32×10^7	1.12×10^8	2.05×10^6	7.42×10^6	6.18×10^7	4.00×10^7
1.27×10^8	1.64×10^8	2.92×10^6	9.96×10^6	7.80×10^7	4.88×10^7
1.93×10^8	2.41×10^8	4.16×10^6	1.35×10^6	9.92×10^7	5.99×10^7
3.14×10^8	3.53×10^8	5.90×10^6	1.73×10^6	1.26×10^8	7.32×10^7
			2.35×10^6	1.61×10^8	9.00×10^7
			3.16×10^6	2.04×10^8	
			4.30×10^6	2.61×10^8	
			5.81×10^6	3.31×10^8	
			8.41×10^6	4.48×10^8	

Table 5.1: Photon flux values for each energy obtained with the PTW ionisation chamber using the scanning technique.

In Figure 5.1 the result of the linear fit for the linearity at 26 keV, obtained with ROOT, is shown. The data represented have been calculated with the automatic count-rate correction applied by DECTRIS while the red curve represents the linear fit. For the estimation of the error of Ψ_{EIGER}, the standard deviation of the counts was propagated. On the contrary for the estimation of the error of Ψ_{PTW}, it was not possible to precisely estimate all the contributions to the uncertainty. Some variability comes from the fact that the camera is calibrated for dose in water while here is scanned in air and that the photon flux may not be directly proportional to the current in the storage ring, due to the presence of optical elements such as the monochromator. The known uncertainties were propagated and rounded up to 5%.
The results for all the energies are summarized in Table 5.2, where the slope (m) and the intercept (q) for each energy are reported. The error associated with the intercept has not been reported as it is compatible with zero.

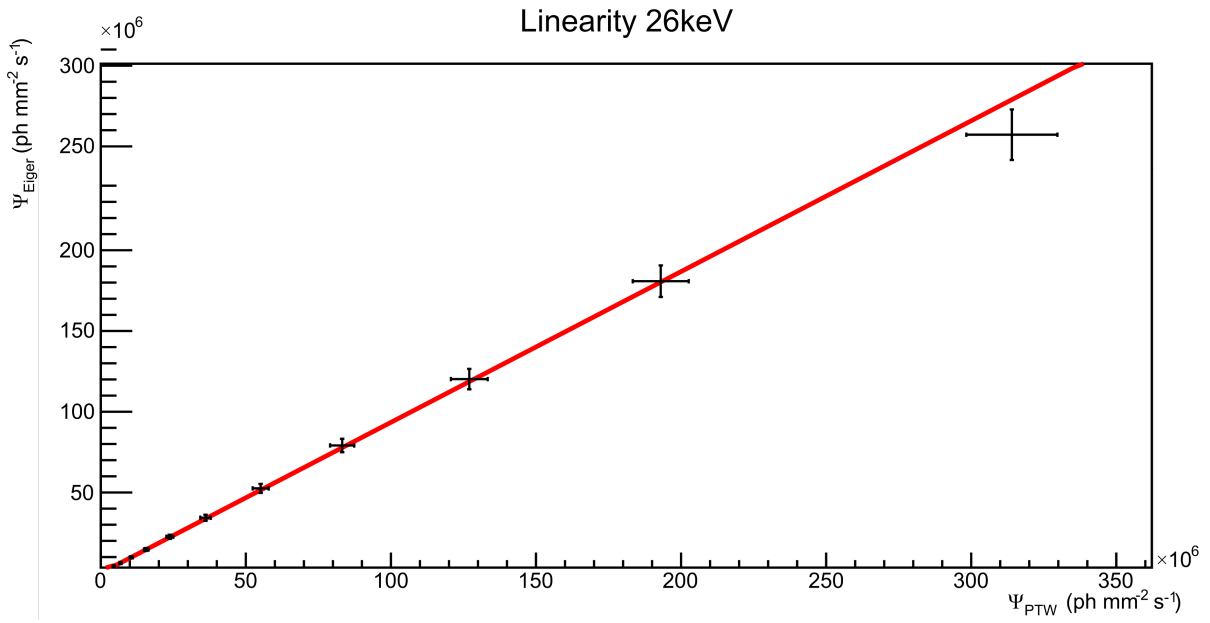

Figure 5.1: Linearity of EIGER2 at 26 keV. Plotted data were acquired by enabling DECTRIS count-rate correction. The red curve represents the linear fit.

E [keV]	m	q
26	(0.93±0.03)	0
28	(0.98±0.06)	0
30	(0.84±0.03)	0
35	(0.76±0.02)	0
51	(0.76±0.02)	0
80	(0.66±0.01)	0

Table 5.2: Slopes (m) and intercepts (q) of the linear fits for each energy studied.

A further analysis has been performed to study the intrinsic linearity of the detector. For this purpose, the flux data obtained with the count-rate correction enabled have been taken as a reference for the linearity condition of the detector. It was then calculated at which flux, for each energy, the data without count-rate correction differed by more than 5% from those with the correction applied.

In Figure 5.2 are shown the data flux for the count-rate correction on and off for the energy of 30 keV. The trendlines added to the two datasets have been introduced just to help the reader with the visualization. The graphs obtained for all the other energies studied are reported in Appendix A, in Figure A.1.

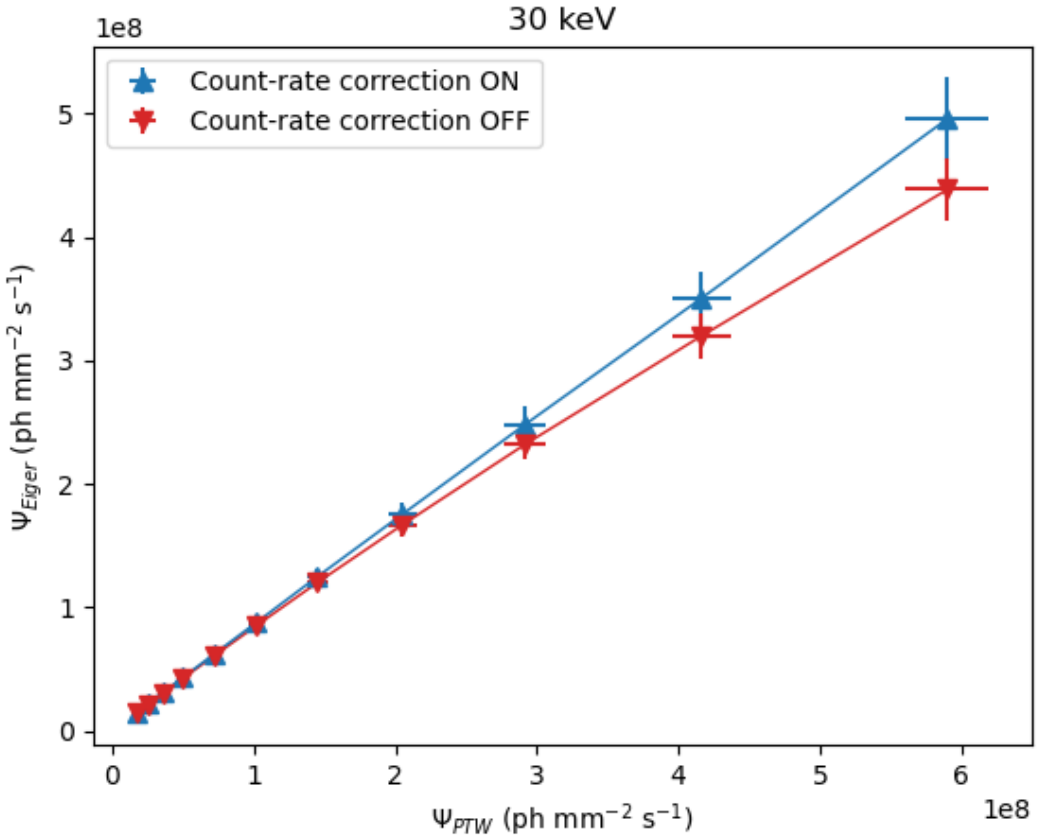

Figure 5.2: Flux recorded by the EIGER2 detector vs the flux measured by a PTW ionization chamber placed upstream the detector for the energy of 30 keV. In blue, the recorded values with the count-rate correction applied; in red the recorded values once the correction was switched off.

In Table 5.3 are reported the values of the fluxes at each energy for which there is a deviation from linearity greater than or equal to 5%. As can be observed, at 26 keV and 80 keV no such deviation has been found for the fluxes analysed. In particular, with regard to the energy of 80 keV, as already mentioned, the flux values considered were chosen low precisely to avoid having the phenomenon of polarisation.

E [keV]	Flux [ph mm^{-2} s^{-1}]
26	-
28	3.53×10^{8}
30	2.92×10^{8}
35	3.16×10^{8}
51	3.31×10^{8}
80	-

Table 5.3: Photon flux data for which a deviation from linearity greater than or equal to 5% of the flux data obtained with the count rate correction disabled is observed.

5.1.2. MTF

For the determination of the MTF, the slanted-edge method, explained in Section 4.1.2, has been exploited. Once the ESF is retrieved, it is differentiated to obtain the LSF. The Fourier amplitude of the LSF is the MTF. A new fitting model for the ESF, developed in collaboration with the Detector Group of the ESRF, has been tested. In Table 5.4 the main results are summarised. For each condition of energy and flux the FWHM (Full Width at Half Maximum) of the LSF and the ESOP (Equivalent Size Of Pixel) are reported. The theoretical FWHM of the LSF should be equal to 75 µm, corresponding to the physical dimension of the pixel (75 µm). Nevertheless, in order to quantify the observed altered frequency response of the detector, especially for those energies where the fluorescence contribution is important, the ESOP parameter has been introduced. It corresponds to the pixel size of an ideal perfect 2D detector that would present a similar MTF below the Nyquist spatial frequency as the detector under investigation [90].
The procedure to determine this parameter is as follows:

1. consider the ideal MTF value at Nyquist frequency ($f_{Nyq} = (2(pixel\ size))^{-1}$),
2. project this MTF value onto the measured curve,
3. find the corresponding frequency (Nyquist frequency associated with this curve),
4. calculate the pixel size that would correspond to this frequency (inverse formula for calculating the Nyquist frequency).

In order to have a better understanding of the procedure, the latter has been graphically represented for a generic MTF in Figure 5.3.

As already introduced in the previous chapter, just the results for the vertical MTF will be presented here since for the horizontal one it was not possible to get enough statistics due to the narrow vertical beam size.

E [keV]	Flux [ph mm^{-2} s^{-1}]	LSF FWHM [µm]	ESOP [µm]
26	1.58×10^{8}	74.79	78.87
	5.56×10^{8}	75.06	80.74
30	2.41×10^{8}	81.29	141.09
	6.99×10^{8}	78.29	135.53
33	2.02×10^{8}	77.55	141.11
	7.25×10^{8}	77.58	145.54
50	1.95×10^{8}	75.57	95.60
	6.58×10^{8}	75.58	94.51
80	3.98×10^{7}	74.86	78.56

Table 5.4: Final results obtained for the MTF. The values of the FWHM of the LSF and the values of the ESOP are reported for each energy value studied and for each flux condition. Around 1M counts/pixel/s and 3M counts/pixel/s have been considered to set the low and high flux condition for each energy respectively.

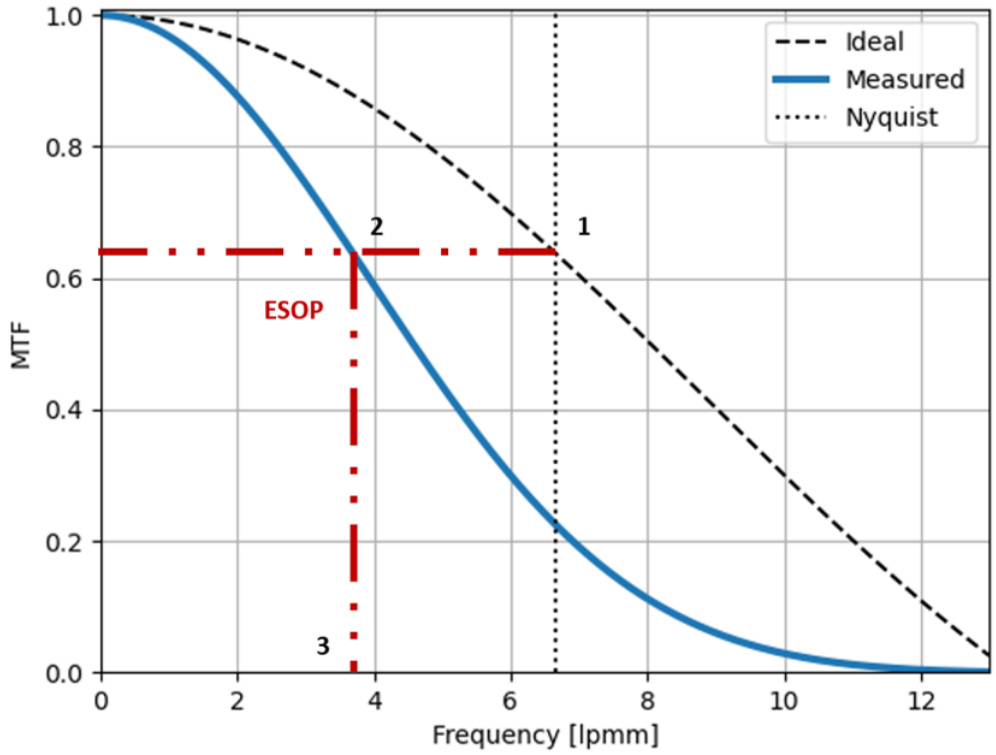

Figure 5.3: Schematisation of the procedure for calculating the ESOP parameter for a generalised MTF. The procedure is to (1) find the MTF value on the ideal curve at the ideal Nyquist frequency. (2) Project this value onto the measured curve and (3) derive the corresponding frequency (Nyquist frequency of the measured curve). From the latter, using the definition of Nyquist frequency, derive the corresponding pixel size.

To show the model output for the low energy range, in Figure 5.4 the results obtained for 33 keV at low flux are presented. In particular, the ESF and the LSF exploited to obtain the MTF are shown. For all the graphs, the ideal curve (dashed) and the measured one (blue) are plotted. Moreover, for the ESF the fitting model (orange) is reported while for the MTF plot, the Nyquist frequency is highlighted (dotted). The latter, as already reported, is calculated as the inverse of half of the pixel size and for the EIGER2 detector, which has a pixel size of 75 µm, is 6.67 mm^{-1}.
This energy, which is close to the K-edges of Cd and Te, has been chosen since it is the most representative to highlight the importance of considering the fluorescence phenomenon in the fitting model of the ESF.

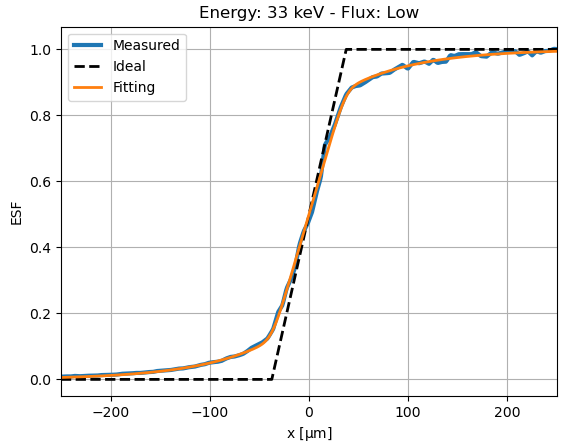

(a)

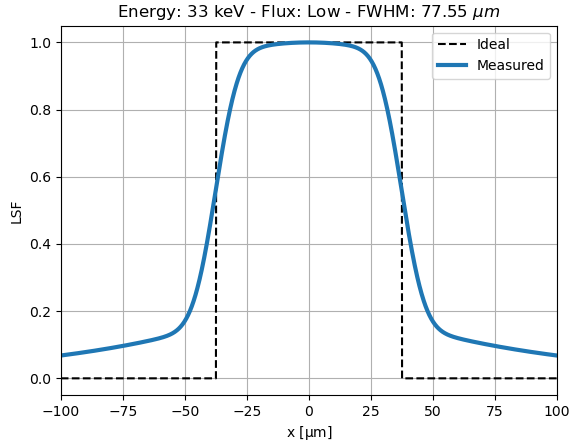

(b)

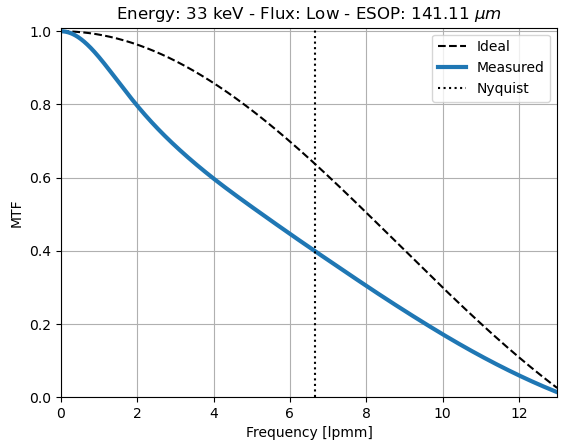

(c)

Figure 5.4: (a) ESF, (b) LSF and (c) MTF for the energy of 33 keV for the low flux condition. For each function the measured and the ideal curves are plotted. For the ESF, the fitting model is reported, while for the MTF plot the Nyquist frequency is highlighted.

In order to demonstrate the relevance of considering fluorescence in the ESF fitting model, for those energies where the phenomenon occurs, it was decided to plot two graphs of the ESF under the same conditions (energy and flux) where one includes fluorescence, and the other does not. For this purpose, the energy of 33 keV and the low-flux condition were once again considered. In Figure 5.5a the ESF without the fluorescence phenomenon is shown, while in Figure 5.5b the ESF includes the fluorescence.

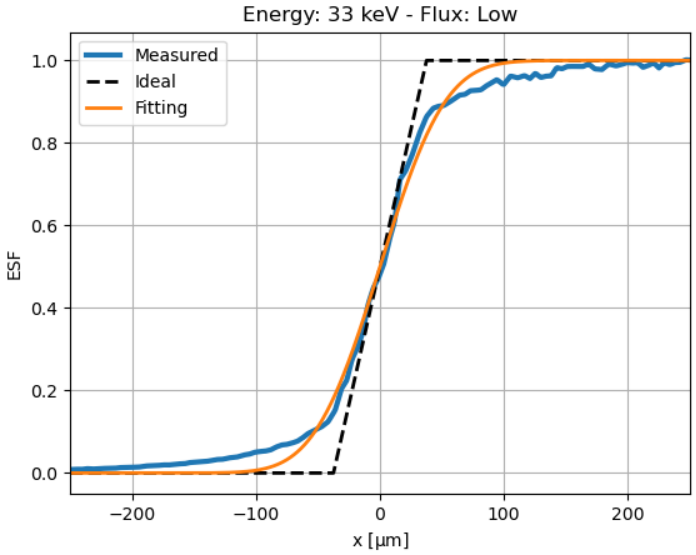

(a) ESF without florescence model applied.

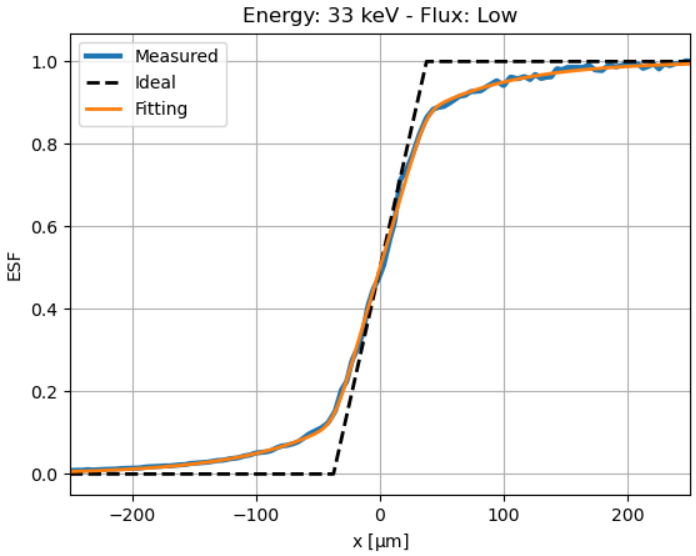

(b) ESF with florescence model applied.

Figure 5.5: ESF for the energy of 33 keV for the low flux condition in which the difference between including (a) and not including (b) the fluorescence phenomenon is shown.

An attempt has been made to study whether the fit parameters used in the model have adequate physical meaning. In particular, the parameters α, c (see Equation 4.6) and σ_{diff} (Equation 4.7) have been studied.

In Figure 5.6 the α parameter for those energies where fluorescence has been included in the fit model of the ESF has been plotted, i.e., for 30 keV, 33 keV and 50 keV. As expected, it is higher for the energies where the fluorescence phenomenon is more accentuated.

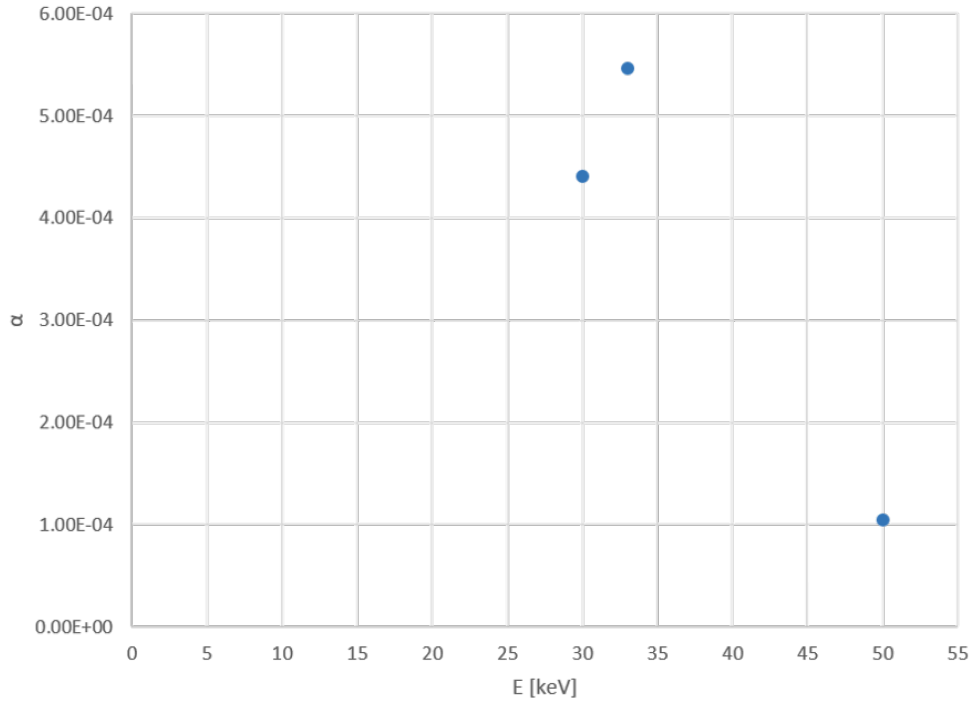

Figure 5.6: α parameter as a function of the photon energy. It has been plotted for those energies where fluorescence has been included in the fit model of the ESF, i.e. 30 keV, 33 keV and 50 keV. It is higher for the energy of 30 keV and 33 keV, where the K-edges of Cd and Te are present, while it is lower for 50 keV since the threshold of the detector may start cutting part of the fluorescence contribution.

Another parameter which is strictly related to the fluorescence component is the coefficient c of the exponential function. In particular, it regulates the width of the fluorescence tails, which are closely related to the distance the fluorescent photon travels before being absorbed. In order to compare the value obtained by the fit with a physical parameter, the mean free path travelled by the fluorescence photon of energy E^* has been computed by:

$$l = \frac{1}{\mu(E^*)} = \frac{1}{\frac{\mu(E^*)}{\rho}\rho} \tag{5.1}$$

where $\mu(E^*)$ is the linear attenuation coefficient of the fluorescence photon and ρ the density of the material traversed by the photon [36]. From NIST [91, 92] the mass attenuation coefficient and the density of CdTe (6.20 g cm^{-3}) can be retrieved. In Table 2.2 the values of the characteristic X-ray energy of Cd and Te are reported.

For a photon of energy 23 keV and 27 keV, the mean free path is equal to 116 µm and 60 µm, respectively. The value of c obtained from the fit at 30 keV is 68.90 µm, while at 50 keV is equal to 95.20 µm. From the comparison between the coefficient of the exponential of the function related to the fluorescence signal and the theoretical value of the mean free path of the photon, it is observed that the coefficient follows the physical interpretation, especially for energies where the fluorescence phenomenon is stronger. At 50 keV the agreement is less good because at this energy the threshold, set at half the energy, could start to cut off part of the signal due to the fluorescence, thus leading to the greater discrepancy between the value obtained with the fit and the theoretical one.

The last parameter studied is σ_{diff}, which quantifies the charge diffusion. By putting together Equations (4.8), (4.9), (4.10), the final expression of sigma is obtained:

$$\sigma_{diff} = \sqrt{\frac{2kTd}{qV}\left(d - \frac{1}{\mu(E)}\right)}. \tag{5.2}$$

The theoretical value of σ_{diff} obtained by this formula, for a photon of 26 keV, is equal to 8.5 µm, to be compared with the value obtained from the fit equal to 8.1 µm.

In Figure 5.7 the LSF, the ESF and the MTF for the 80 keV at low flux are presented. In this case the fluorescence phenomenon has not been included in the model.
The graphs obtained for the determination of the vertical MTF for all the other energies and fluxes studied are reported in Appendix A, in Figure A.2, A.3, A.4 and A.5. Moreover, in Appendix A, the graphs related to the determination of the horizontal MTF for all the energies and fluxes analysed are presented (Figure A.6, A.7, A.8, A.9 and A.10).

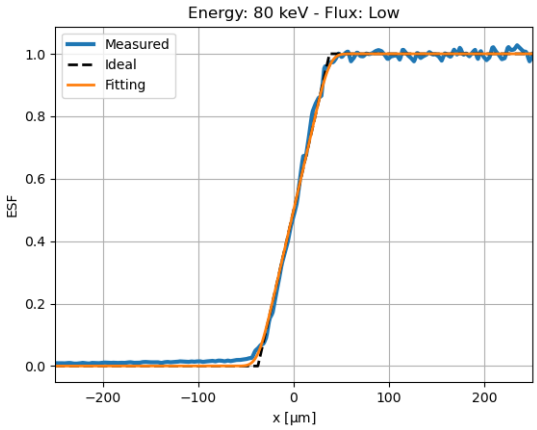

(a)

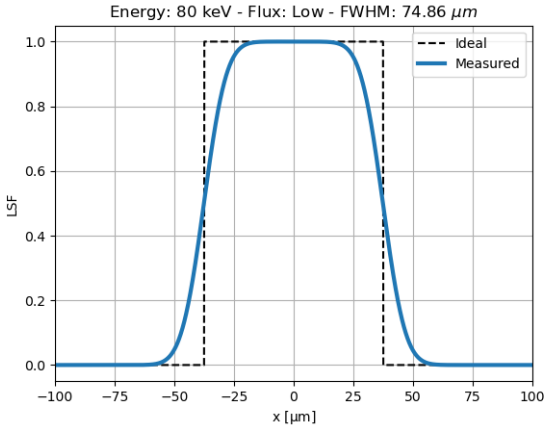

(b)

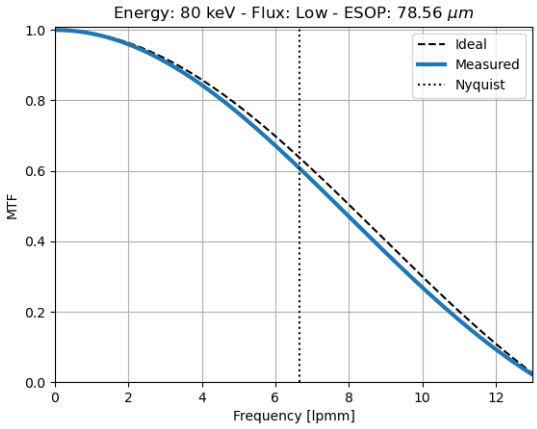

(c)

Figure 5.7: (a) ESF, (b) LSF and (c) MTF for the energy of 80 keV for the low flux condition. For each function the measured and the ideal curves are plotted. For the ESF the fitting model is reported while for the MTF plot the Nyquist frequency is highlighted.

5.1.3. NNPS

To obtain the NNPS the NPS must first be calculated. Since the response of the EIGER2 detector is not uniform in time, a detrend technique has been applied to the data presented below, as explained in Section 5.1.3. The Savitzky-Golay filter has been used to perform an instant-by-instant background correction. The flux values exploited for the calculations are reported in Table 5.5. All the results in this section refers to the vertical NNPS.
In Figure 5.8 an example of the NNPS for the energy of 26 keV at high flux, as a function of the vertical and horizontal frequency, is presented. It reveals that there are artefacts at very low frequency.

E [keV]	Flux [ph mm^{-2} s^{-1}]
26	1.58×10^{8}
	5.56×10^{8}
30	2.41×10^{8}
	6.99×10^{8}
33	2.02×10^{8}
	7.25×10^{8}
50	1.95×10^{8}
	6.58×10^{8}
80	3.98×10^{7}

Table 5.5: Photon flux values exploited for the calculation of the NNPS for each energy. Around 1M counts/pixel/s and 3M counts/pixel/s have been considered to set the low and high flux condition for each energy respectively.

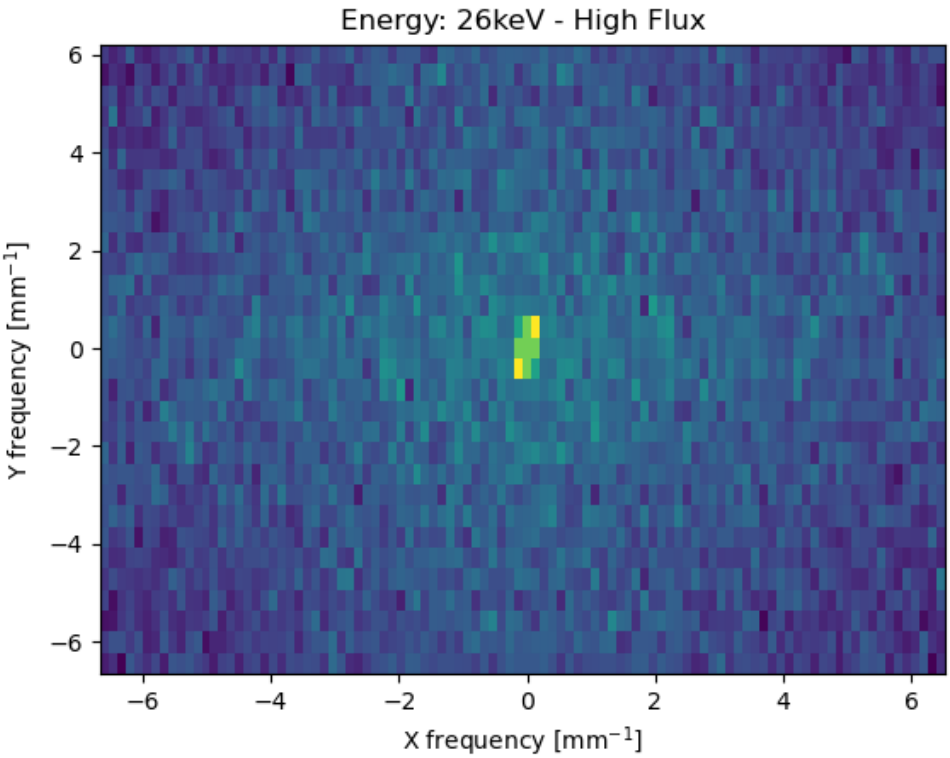

Figure 5.8: NNPS as a function of the vertical and horizontal frequency at 26 keV for the high flux condition.

For this reason, the one-dimensional cuts of the NNPS along the vertical direction, after having averaged two rows/columns on both sides of the axes, have been calculated. In Figure 5.9 the NNPS curves as a function of the spatial frequency for the energy range 26-50 keV are presented. In particular, Figure 5.9a refers to the low flux condition, while the Figure 5.9b shows the NNPS curves for the high flux.

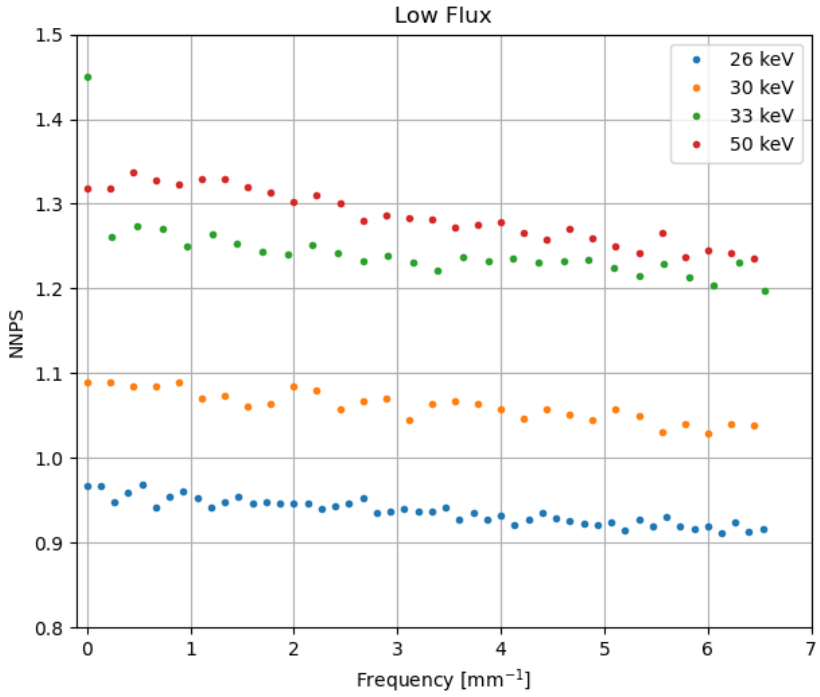

(a)

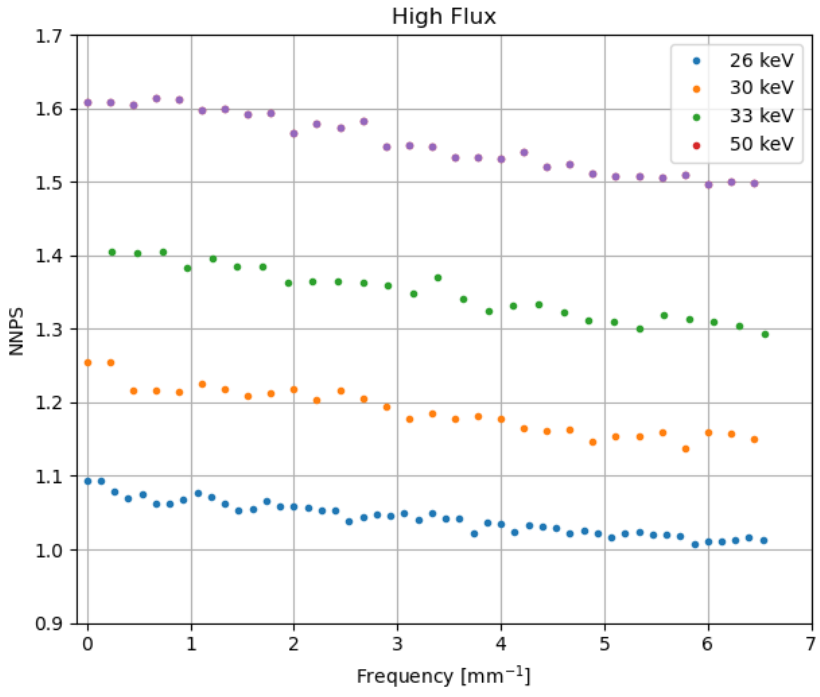

(b)

Figure 5.9: NNPS as a function of the spatial frequency for the energy range 26-50 keV and for the low (a) and high (b) flux conditions.

In Figure 5.10 the NNPS as a function of the spatial frequency for the energy of 80 keV at low flux is shown.

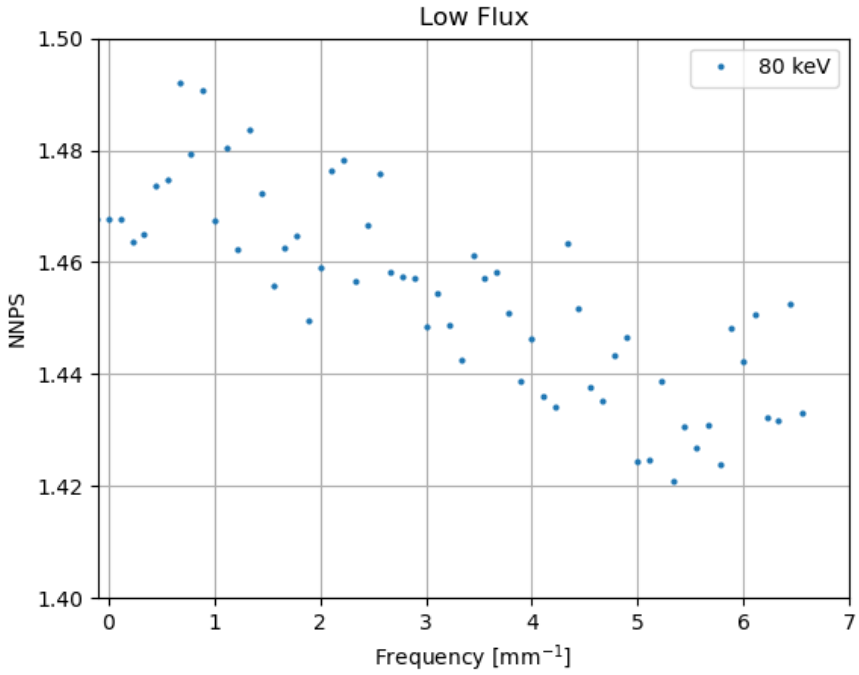

Figure 5.10: NNPS as a function of the spatial frequency for the energy of 80 keV and for the low flux condition.

5.1.4. DQE

Once the MTF and the NNPS have been derived, the DQE can be calculated by dividing the MTF by the NNPS at each spatial frequency. In Figure 5.11 the DQE curves as a function of the spatial frequency for the low energy range 26-50 keV is presented. In particular in Figure 5.11a the DQE is calculated at low flux while in Figure 5.11b at high flux.

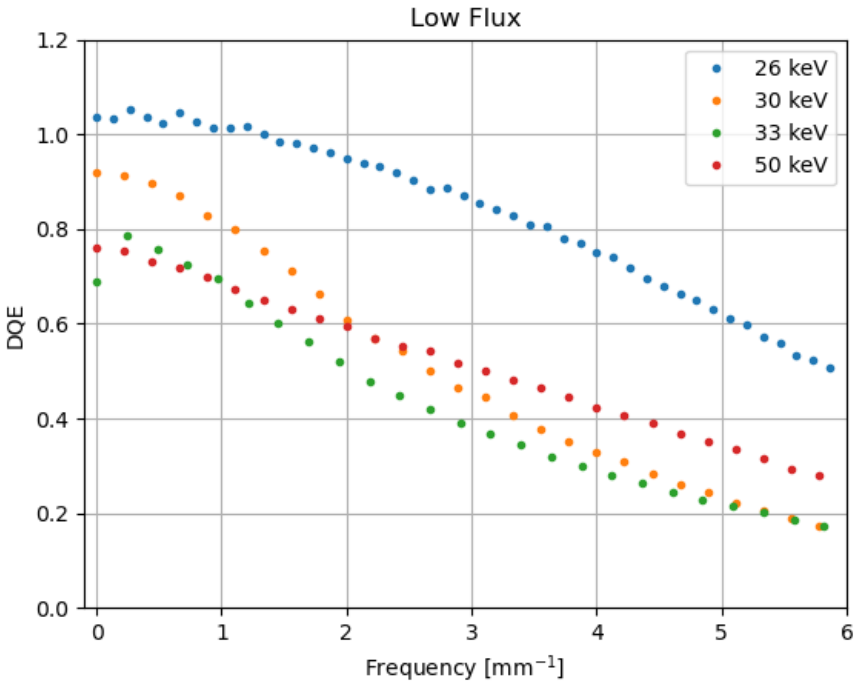

(a)

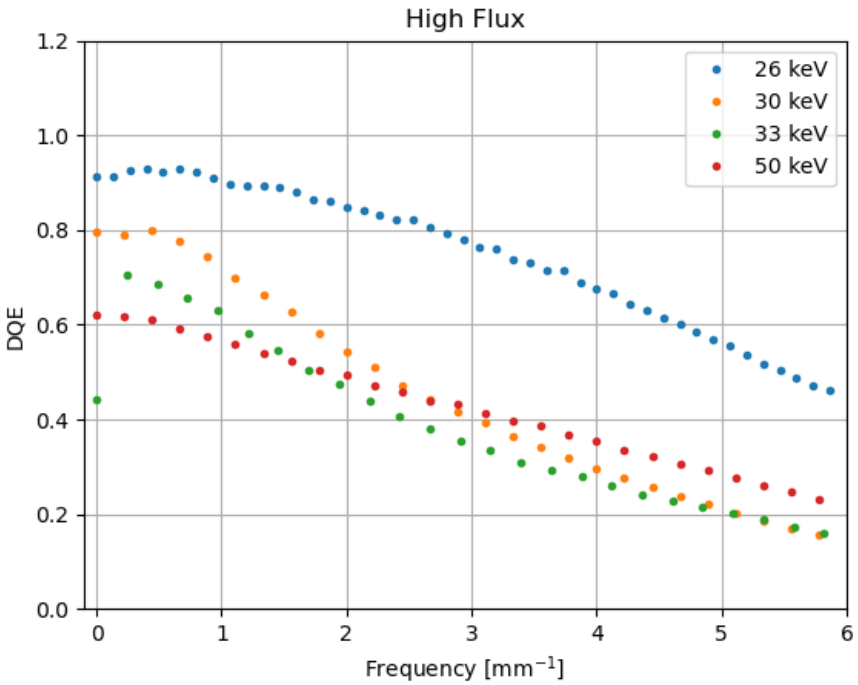

(b)

Figure 5.11: DQE as a function of the spatial frequency for the energy range 26-50 keV and for the low (a) and high (b) flux conditions.

In Figure 5.8 the DQE as a function of the spatial frequency for the 80 keV at low flux is shown.

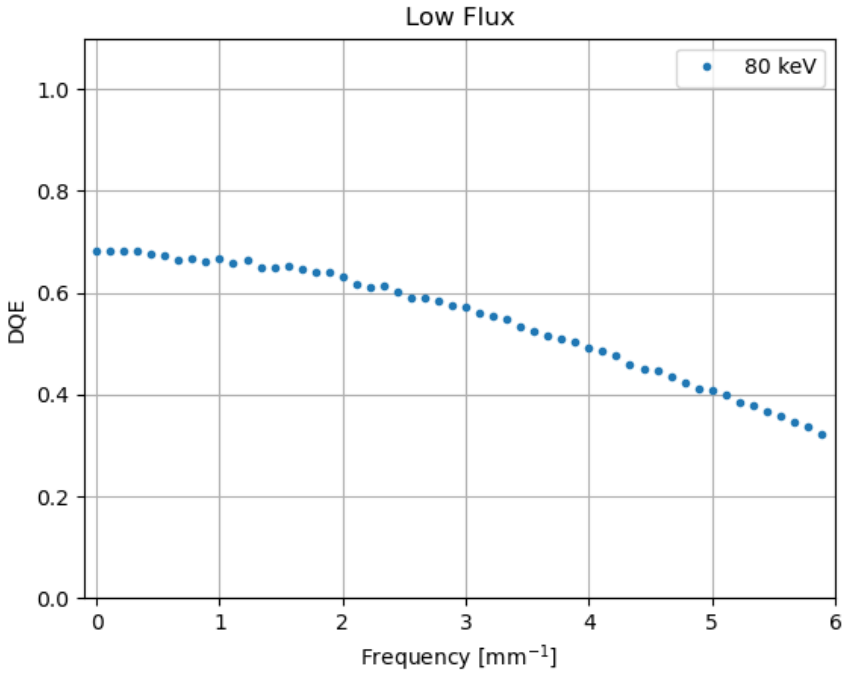

Figure 5.12: NNPS as a function of the spatial frequency for the energy of 80 keV and for the low flux condition.

5.2. EIGER2 stability

5.2.1. At startup

The idea behind the study of the stability of the detector at start-up was to find out how long it would take to reach stability once it has been initialized. One HV reset has been performed each hour for 8 consecutive times. In Figure 5.13 the trend of the leakage current after each reset is shown. The plot has been obtained with EXCEL.

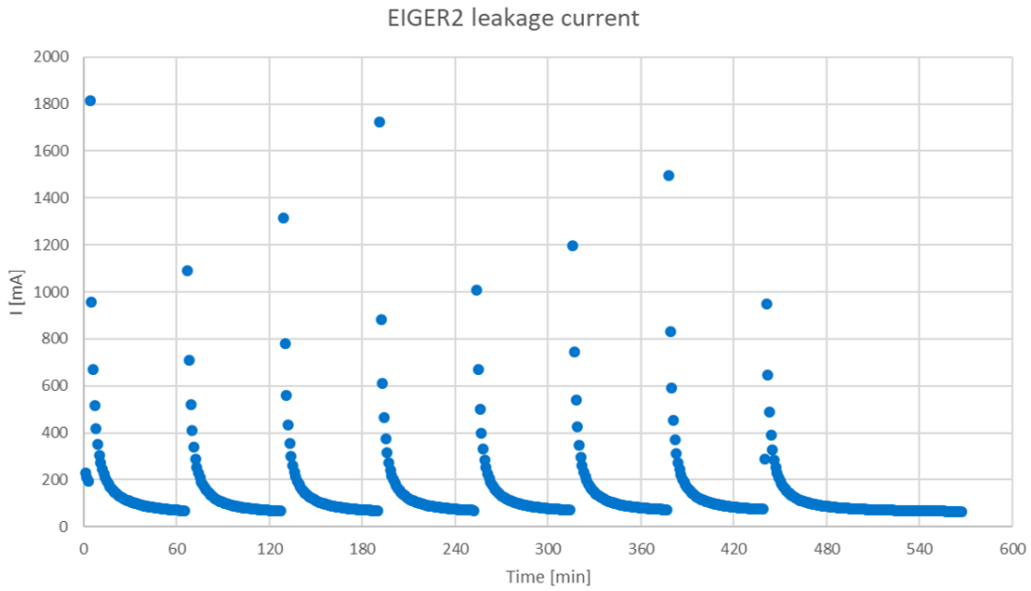

Figure 5.13: Leakage current of the EIGER2 detector as a function of time. It has been acquired after each of the 8 HV resets performed 1 hour apart.

5.2.2. During a CT scan

Knowing the stability of the detector during a typical CT experiment is extremely important to obtain good results. The procedure, which is deeply explained in Section 4.2.2, briefly consists in performing an HV reset so that the detector stabilizes and in continuously irradiating the detector (1 minute) 3 times by acquiring 1 wf image every 10 ms with an integration time of 10 ms. Between one irradiation and the other a time T_{sleep} is waited. All the combinations of energy, flux and T_{sleep} time studied are reported in Table 4.4a.

In Figure 5.14 the main results for the energy of 33 keV and for each condition of flux (low and high) and T_{sleep} time are shown. In particular, the average normalized counts for the ring current acquired at the initial instant of irradiation of each CT are presented. The three irradiations performed, CT1, CT2 and CT3 are represented by a blue, red and green curve respectively. A smoothing of the data has been performed through the application of the Savitzky-Golay filter.

Table 5.6 shows the initial and final ring current values and their relative percentage variation for the energy of 33 keV, the T_{sleep} time of 1 minute, for the two flux conditions and for each CT. As can be observed, the percentage variation between the two current values is of the order of 1-2 $^{o}/_{oo}$. This value was also found for the other conditions studied. Therefore, the fact of having normalized only for the initial current and not for

a combination of the two leads to a completely negligible error for the analysis.

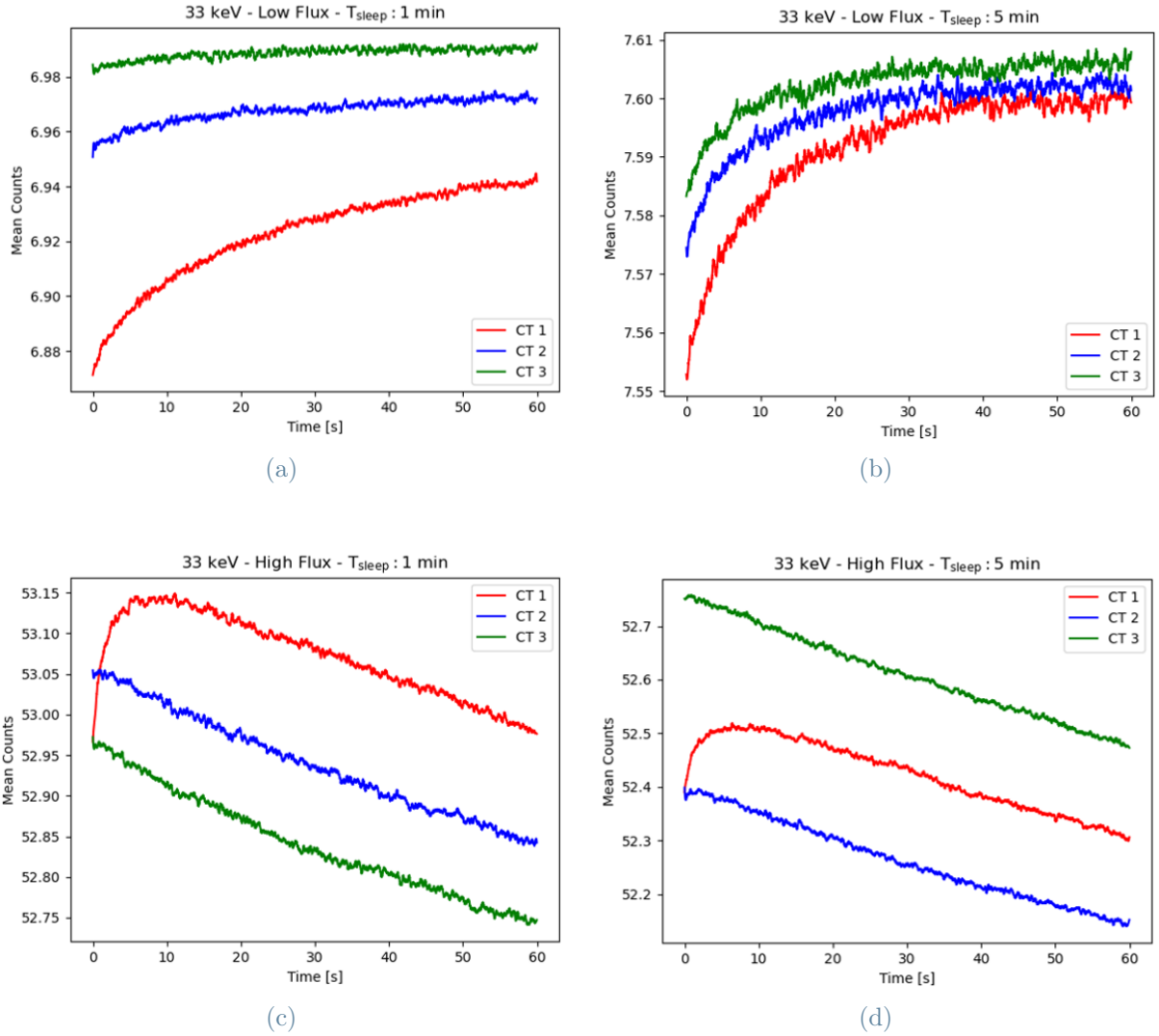

Figure 5.14: The mean counts for the energy of 33 keV and for each condition of flux, low (a, b) and high (c, d), and T_{sleep} time (1 and 5 minutes) are presented. In particular, data have been normalized for the ring current acquired at the initial instant of the 1 minute of irradiation. In red the first minute of irradiation (CT1), in blue the second minute of irradiation (CT2) and in green the third one (CT3).

33 keV					
Flux	T_{sleep} **[s]**	**CT**	I_{in}	I_{out}	ΔI %
Low	60	1	198.827	198.534	0.147
		2	198.534	198.239	0.149
		3	198.239	197.944	0.149
High	60	1	198.008	197.755	0.128
		2	197.738	197.490	0.125
		3	197.486	197.233	0.128

Table 5.6: Percentage variation of the ring current between the initial instant of irradiation and the last one for each CT. In particular, the values for the energy of 33 keV and T_{sleep} of 1 minute and for each flux condition are reported.

In Figure 5.15 the results for the 50 keV are reported. The operating conditions are exactly the same as those explained for the previous energy.

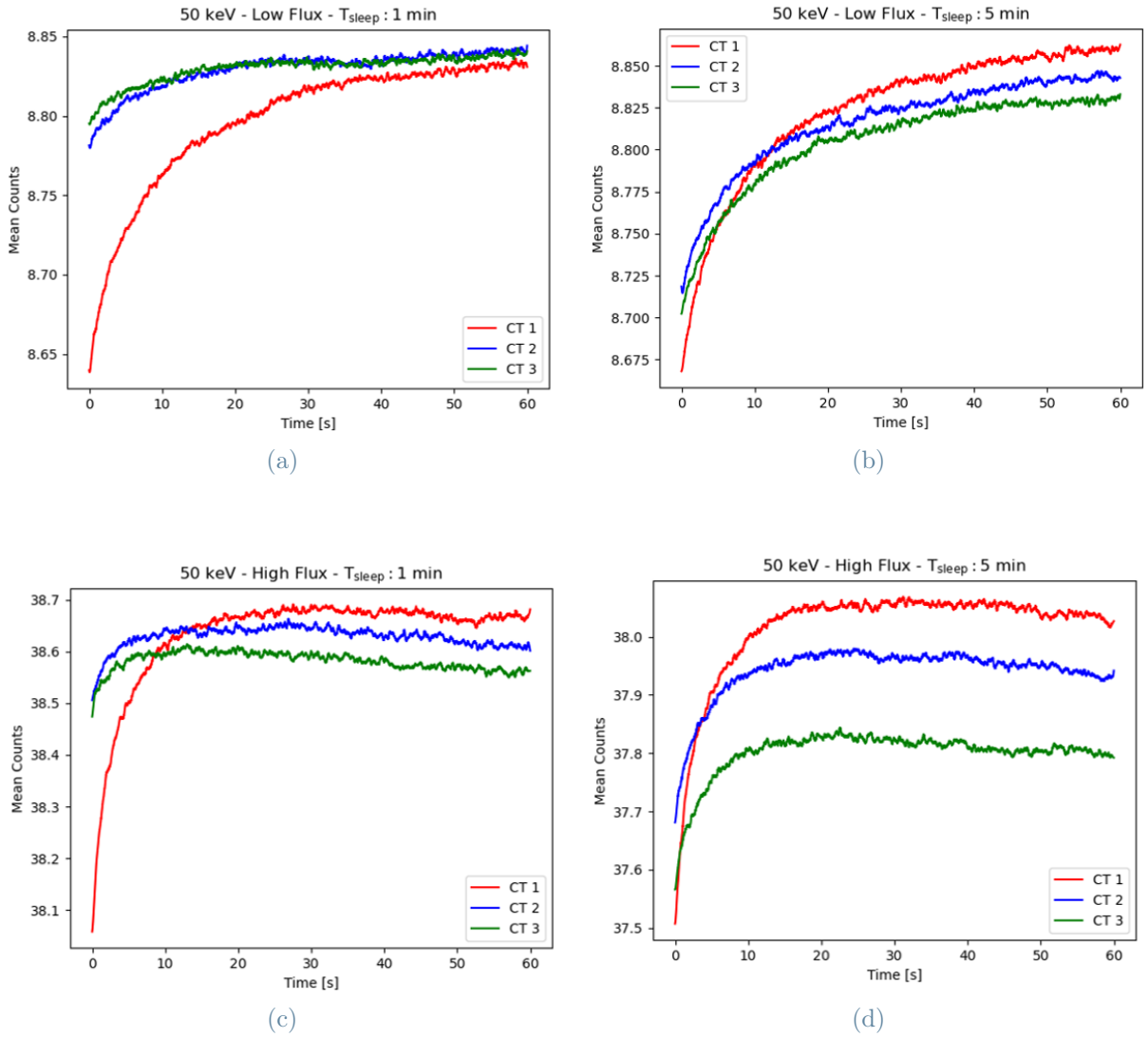

Figure 5.15: The mean counts for the energy of 50 keV and for each condition of flux, low (a, b) and high (c, d), and T_{sleep} time (1 and 5 minutes) are presented. In particular, data have been normalized for the ring current acquired at the initial instant of the 1 minute of irradiation. In red the first minute of irradiation (CT1), in blue the second minute of irradiation (CT2) and in green the third one (CT3).

In the light of the graphs just presented, it was decided to see whether stable average counts correspond to a stable image. The idea is to study whether or not a local modification of the wf images is observed during irradiation, i.e. to see if any structures appear within the image or not. Recalling the experimental procedure, during 1 minute of irradiation, 6000 wf images have been acquired, thus 1 wf image every 10 ms. To study this, the ratio between the wf image at the end of the 1 minute irradiation for one CT and the wf image at time 0 (beginning of irradiation) for the same CT has been performed. The

calculation has been done for each CT at each condition of flux and of T_{sleep} time. In particular in Figure 5.16 are reported the images obtained at the energy of 33 keV while in Figure 5.17 at the energy of 50 keV.

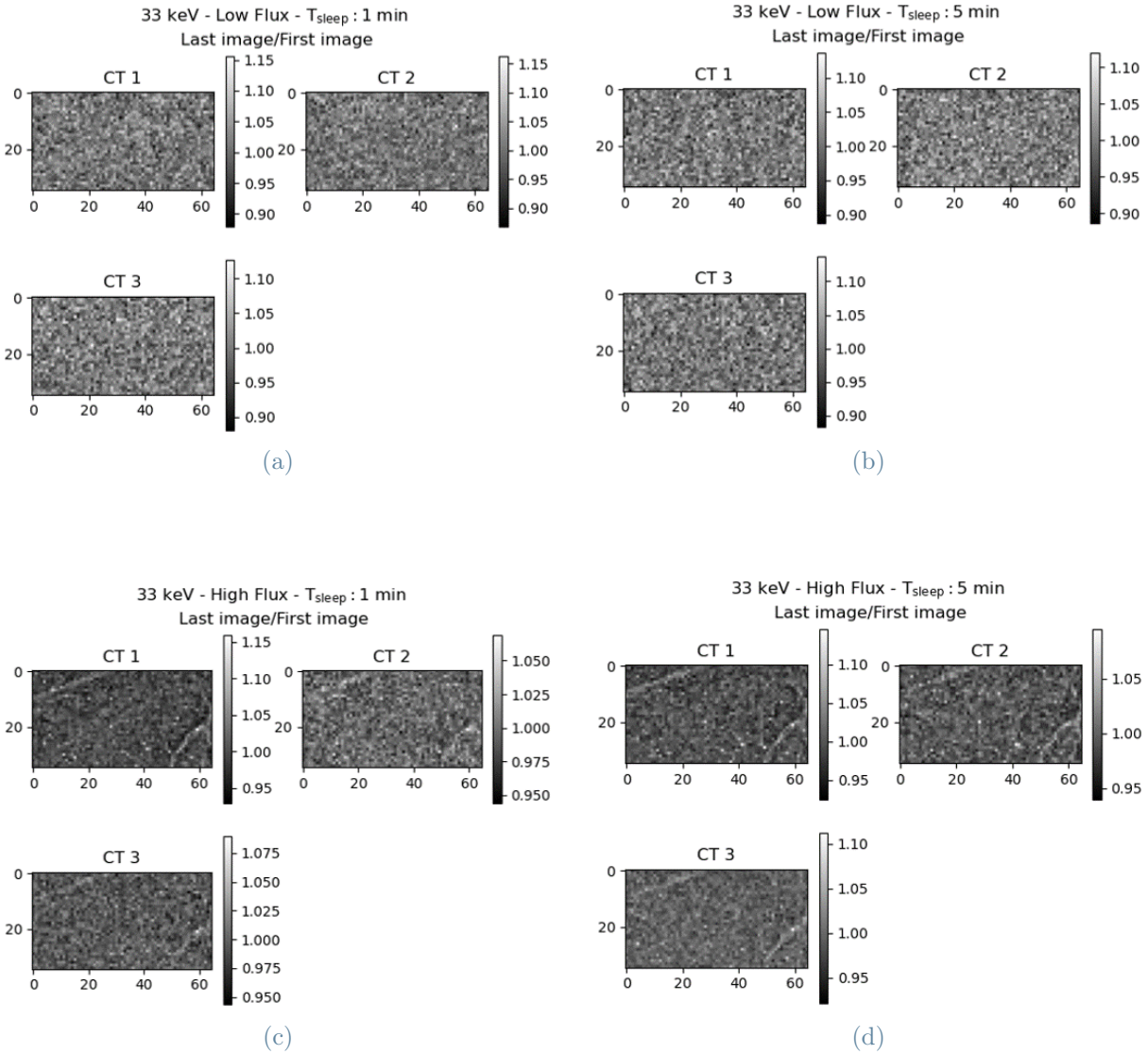

Figure 5.16: Images showing the ratio between the wf image acquired at the initial instant of the minute of irradiation and the wf image corresponding to the final instant of irradiation for each CT and for the energy of 33 keV. They are reported for each condition of flux, low (a, b) and high (c, d), and T_{sleep} (1 and 5 minutes).

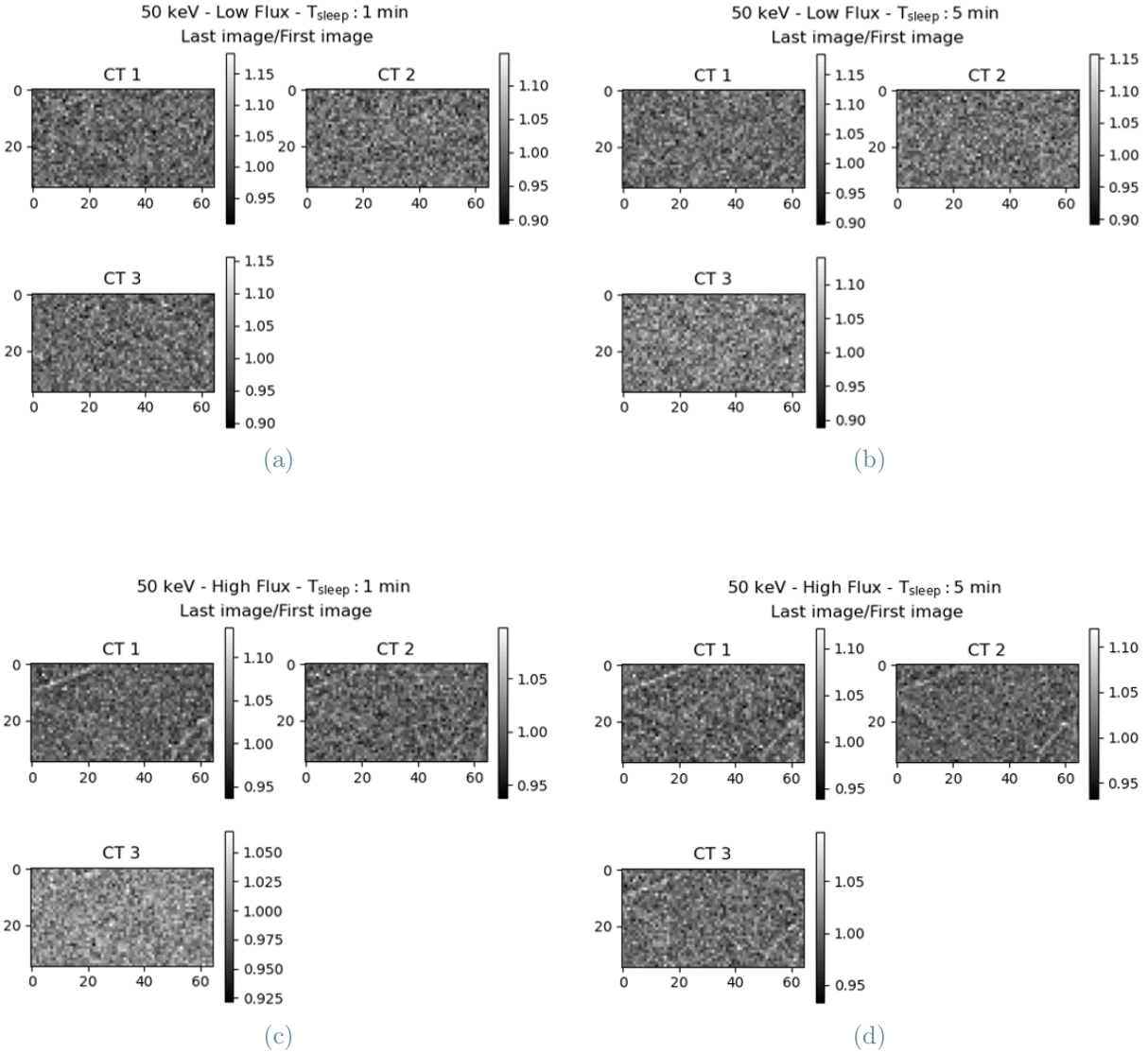

Figure 5.17: Images showing the ratio between the wf image acquired at the initial instant of the minute of irradiation and the wf image corresponding to the final instant of irradiation for each CT and for the energy of 50 keV. They are reported for each condition of flux, low (a, b) and high (c, d), and T_{sleep} (1 and 5 minutes).

As already introduced in the previous chapter, to have a more complete dataset of the stability study and to verify the hypothesis formulated for the previous results, the dataset has been enlarged by considering longer T_{sleep} times: 10 and 20 minutes. The calculations have been done just for the energy of 33 keV for reasons of time. In Figure 5.18 the mean counts normalized by the initial current of the ring for each CT and for each condition of flux and T_{sleep} time are shown. The plots with T_{sleep} time of 10 minutes for low and high flux were cut off at 50 s and 30 s respectively as there was a refill of the electron beam

in the storage ring, resulting in a sudden increase of the ring current. Also in this case, the ratio between the wf image at the end of the 1 minute irradiation for one CT and the wf image at time 0 for the same CT has been performed to see if any structures appear within the image or not. The results are shown in Figure 5.19.

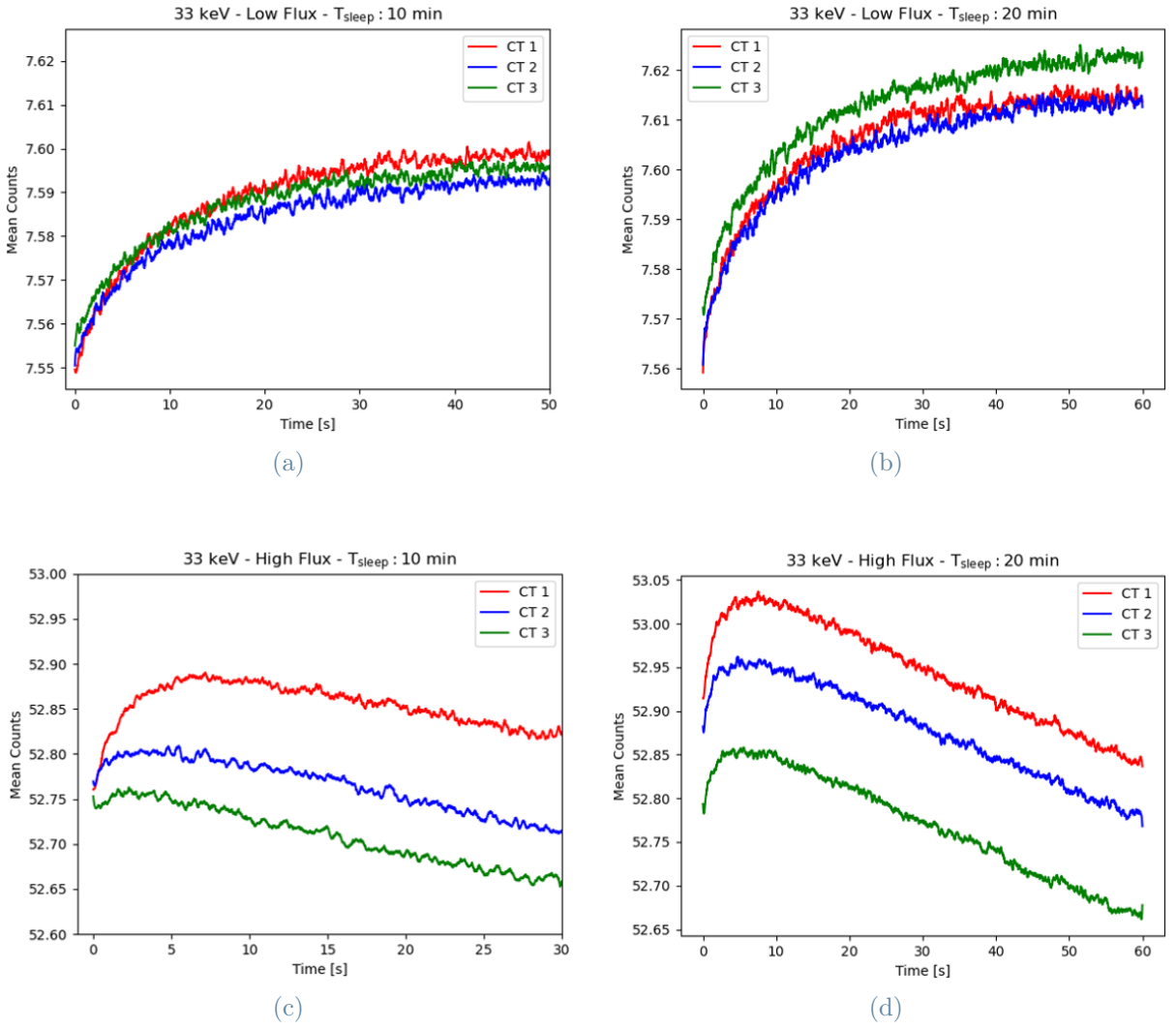

Figure 5.18: The mean counts for the energy of 33 keV and for each condition of flux, low (a, b) and high (c, d), and T_{sleep} (10 and 20 minutes) are presented. In particular, data have been normalized for the ring current acquired at the initial instant of the 1 minute of irradiation. In red the first minute of irradiation (CT1), in blue the second minute of irradiation (CT2) and in green the third one (CT3).

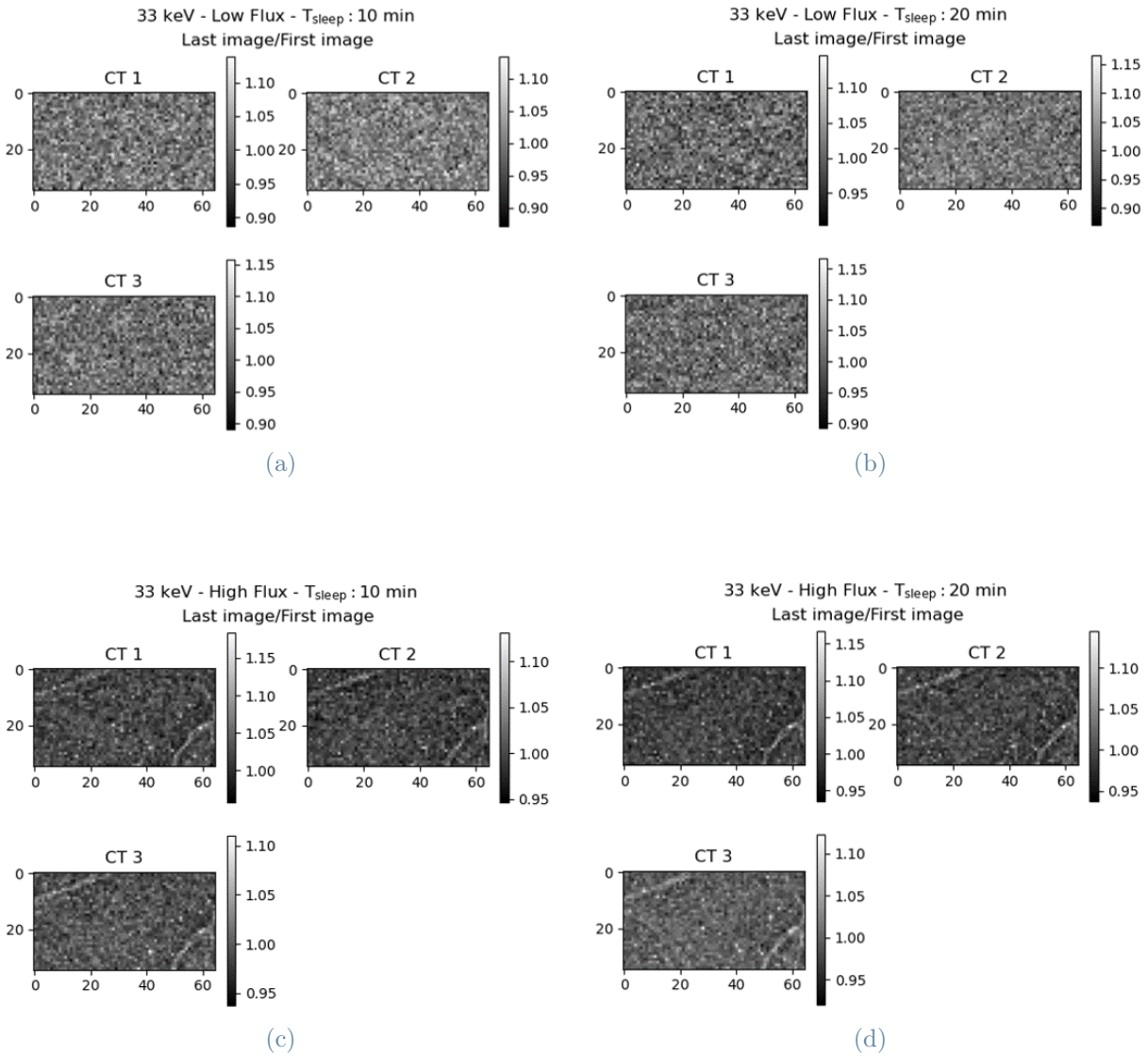

Figure 5.19: Images showing the ratio between the wf image acquired at the initial instant of the minute of irradiation and the wf image corresponding to the final instant of irradiation for each CT and for the energy of 33 keV. They are reported for each condition of flux, low (a, b) and high (c, d), and T_{sleep} (10 and 20 minutes).

6 | Discussion

In this chapter, the results of the characterization of the EIGER2 detector are discussed. There are some aspects which represented a limitation for the measurements presented in the previous chapter:

- limited vertical beam size,
- Gaussian beam profile,
- beam instabilities due to drifts of the monochromator crystals,
- decrease of electron beam current over time,
- change in time of sensor response when irradiated.

These limitations made it necessary to introduce new methods for data acquisition and analysis. In particular, for the detector linearity calculation, the scanning technique had to be used, while for the MTF and NPS a readjustment of the ISO standard guidelines was necessary.

In particular, the first two limitations mean that it is impossible to have uniform irradiation of the detector sensor, while the fact that the sensor response changes over time means that time dependent detrending techniques must be applied. The decrease of the electron beam current is practically negligible (loss of 5% in 1 hour) and especially for those measurements where the irradiation lasts for a short time can be considered a negligible error. The beam oscillations could be due to ground vibrations or in our case also to oscillations induced by the monochromator cooling system. However, for the measurements made during this characterization, this latter error contribution should be negligible as it becomes more important at submicron resolution.
In general, an accurate estimate of the errors associated with any measurement performed is very difficult to make as there are many factors involved.

6.1. EIGER2 performances

6.1.1. Linearity

The linearity of the detector in typical working ranges has been studied. The incoming photon flux has been calculated through the scanning technique by exploiting a PTW ionization chamber. The use of this technique has been necessary since standard dosimetry and reference calibration protocols require a uniform irradiation of the ionization chamber but at the synchrotron this condition can not be met. In fact, the vertical dimension of the beam is smaller than the dimensions of the thimble chamber. The values of the flux obtained with the PTW have been reported in Table 5.1 for the energies in the working range 26-51 keV and for the high energy of 80 keV. Through the use of Plexiglas attenuators, the flux has been properly tuned. For the energy range 26-51 keV, the fluxes ranged from low to high (no Plexiglas thickness). For the energy of 80 keV, on the other hand, the fluxes were kept at relatively low values in order to prevent the polarization phenomenon from occurring. In fact, the attenuator of thickness 12 cm, corresponding to the highest flux value used (9.00×10^7 photons/mm^2/s) was chosen before a drop in efficiency was detected for higher flux values. In particular, a 7% drop in efficiency was already observed from a flux of 1.72×10^8 photons/mm^2/s compared to the flux value of 9.00×10^7 photons/mm^2/s. Once again, to avoid this phenomenon of detector polarization only two wf images has been acquired for each attenuator thickness, so as to expose the detector to minimum radiation, but at the expense of statistics. On the contrary, for the energy range 26-51 keV 10 wf images have been acquired for each attenuator thickness. Half of the wf images acquired were taken by enabling DECTRIS count-rate correction and the other half by disabling it.
Dose measurements with the PTW were made under different conditions (air) from the calibration ones (water); this results in a systematic error of the order of a few percent.

In Table 5.2 the linearity results for all the energies are reported. This analysis of linearity has been performed by enabling the count-rate correction of DECTRIS. In the light of the results the correction works well especially for low energies while around 30 keV a deviation from the linear behavior begins to occur. This deviation is attributable to the presence of the K-edges of Cd and Te. In fact, the photons absorbed around these energies can give rise to fluorescence photons, which in some cases can be absorbed by adjacent pixels. This leads to a decrease in detector efficiency and spatial resolution. A recovery of efficiency starts to be noticeable from 50 keV onwards, where the fluorescence phenomenon gradually diminishes. The efficiency decreases again at 80 keV. This behavior is in accordance with the measured and simulated quantum efficiency by DECTRIS, where around 30 keV and 80 keV a decrease is achieved (refer to Figure 2.12). The result for the linearity at 26 keV obtained with ROOT has been reported in Figure 5.1. The error of

the flux at the detector has been estimated by propagating the standard deviation of the counts, while a precise estimation of the error for the calculation of the flux with PTW has been not possible. As already mentioned, the PTW ionization chamber is calibrated for dose in water while here is scanned in air and moreover the photon flux may not be directly proportional to the current in the storage ring, due to the presence of optical elements along the beam path, such as the monochromator. The known uncertainties has been propagated and rounded up to 5%.

A further analysis has been performed to study the intrinsic linearity of the detector. The idea was to take the flux data acquired with the count-rate correction enabled as a reference for the linearity condition of the detector and see for which flux data obtained by disabling the correction deviated by more than 5% from those values taken as a reference for linearity. As can be seen from the values obtained in Table 5.3, this flux value corresponds to approximately 3×10^8 photons/mm^2/s for the energy range 28-51 keV. For the energy of 26 keV and 80 keV no such deviation has been found for the fluxes analyzed. Beyond this flux value, linearity correction is no longer negligible and can alter the pixel count statistics.

6.1.2. MTF

The MTF has been determined by using the edge method, since several studies have demonstrated that, in comparison to the slit method, it is easier and more practical to apply, and it provides accurate results in the low- and mid- frequency domain [55, 56]. The experimental protocol was initially developed to derive both vertical and horizontal MTF. However, due to an intrinsic limitation of the synchrotron radiation beam, it was not possible to obtain sufficient statistics for the horizontal MTF. This limitation is represented by the very narrow vertical dimension of the beam. Hence, just the vertical MTF results have been presented in the previous chapter.
The measurements were carried out in two different experimental sessions. More specifically, the detector was initially characterised in terms of the MTF in a relatively low energy range between 26 keV and 50 keV. Subsequently, it was decided to determine the MTF also at high energies and in particular the measurement was performed at the energy of 80 keV. For each energy in the low energy range, measurements were carried out for two separate fluxes: low and high. An attempt was made to maintain a number of counts around 1M counts/pixel/s and 3M counts/pixel/s for low and high fluxes respectively. For the 80 keV only the low flux condition has been studied in order to avoid the polarization phenomenon.

In Table 5.4 are reported the results obtained for all the energies. A weak flux dependence has been observed and it has been noticed that although the LSF gives a FWHM of about 75 µm for all the energies, which is a value required by DECTRIS, the frequency response is completely altered, especially for those energies where the fluorescence contribution becomes important. To quantify this, the ESOP parameter has been introduced. As can be seen from the ESOP values obtained, the pixel size corresponding to the Nyquist frequency for the measured MTF curve is greater than the value of 75 µm. For energies of 30 and 33 keV, where the fluorescence phenomenon is strong, the ESOP is about twice as large as the ideal pixel size. Hence, it is more appropriate to consider the MTF than the LSF as the MTF gives a whole frequency characterization.

In this thesis, a new fitting model for the ESF has been considered, resulting from an internal collaboration with the ESRF Detector Group Division. The paper has not yet been published as final refinements of the code are being undertaken but the rational behind this study was to start testing it with data acquired at ID17. Zambon et al. [84] had already taken the ESF fit model one step further than the typical ERF fitting model found in the literature by considering the physical dimension of a pixel of a single photon counting detector, modelled with a box function. However, they did not take the fluorescence phenomenon into account, as according to them a Monte Carlo simulation was needed. In this new fitting model, this phenomenon has been taken into account and it has been applied to those energies where the fluorescence phenomenon is present, i.e. for the energies of 30 keV, 33 keV and 50 keV. For these energies, the inclusion of fluorescence has led to improved results. Plots of the ESF for the energy of 33 keV and for the low flux condition with and without the application of fluorescence are shown in Figure 5.5. As can be observed, the fluorescence model fits well the tails of the measured curve, which are due to the fluorescence contribution. Although the model has yet to be finalised, an attempt has been made to investigate whether the model parameters had any physical significance. The first parameter studied has been α (Equation 4.6), which gives an indication of the fluorescence contribution. This parameter, which is given by the ratio between the multiplicative coefficient of the exponential (fluorescence contribution) and the multiplicative coefficient of the delta (primary absorption contribution), must be high for those energies where the fluorescence contribution dominates over the primary absorption contribution. Plotting this parameter as a function of energy, it can be observed that it reflects what has just been said. In fact, it is high for 30 and 33 keV, i.e. for energies close to the K-edges of Cd and Te, and decreases as it moves away from this K-edge.

Another parameter strictly related to the fluorescence phenomenon is the coefficient c of

the exponential function (Equation 4.6). It regulates the width of the fluorescence tails, which are closely related to the distance travelled by the fluorescence photon before being absorbed. Hence, the value of the parameter obtained with the fit model has been compared to the value of the mean free path travelled by the fluorescence photon and calculated through the Equation 5.1. For the energy of 30 keV, where the fluorescence contribution is strong, a good agreement has been obtained between the two values. For the 50 keV energy, where the fluorescence contribution is less predominant, the agreement has proven less good but still reasonable.
The last parameter studied has been σ_{diff}, which quantifies the charge diffusion. From Equation 5.2 the theoretical value has been obtained. The comparison between the theoretical value and that obtained from the fit has been done for the energy of 26 keV, where the fluorescence contribution is not present. This comparison has been made with this energy to reduce the number of parameters involved in the model. The agreement between the two values is very good. This analysis proves that this new model used to fit the ESF, although still in the testing phase, is a good approximation of the physical system. In order to show the complete model for the calculation of the MTF, the graphs obtained for the ESF, LSF and MTF has been reported for the energy of 33 keV and 80 keV (see Figures 5.4 and 5.7). The behaviour at 33 keV has already been explained at length, and as can be seen from the final graph of the MTF, there is a deviation of the measured curve from the ideal trend, already at low frequencies. The curves measured at 80 keV have an almost ideal behaviour. Fluorescence has not been applied to the fit model for the ESF as its contribution is negligible at this energy. The fit reproduces well the experimental data, which are very close to the ideal trend. Both the FWHM of the LSF and the ESOP are about 75 µm, in accordance with the ideal pixel size. The MTF is practically ideal at low frequencies and deviates slightly from the ideal curve at medium and high frequencies.

The biggest contributor to error in this measurement could be the blade used for the edge method. This may not have perfectly straight edges but may have imperfections, making impossible to realign perfectly the ESFs of different rows/columns. In addition, the blade should be attached to the detector to avoid blurring but this is not experimentally possible as it has to be positioned on a suitable motor for correct inclination.
In addition, inter-pixel intensity fluctuations may lead to an error in the fit regarding the estimation of the correct edge position in the different columns.

6.1.3. NNPS

The NNPS was obtained by multiplying the NPS by the photon fluence and dividing it by the number of counts squared. Since the CdTe sensor of EIGER2 changes over time, a feature known in the literature [31] and also observed during the experimental activity of this thesis, a time dependent detrend technique has been applied to the acquired wf images. Due to the fact that, with synchrotron radiation (Gaussian beam profile), it is not possible to have a uniform exposure of the detector sensor and that the response of the detector is not constant with time, the ISO standard guidelines could not be applied. In all the considered flux-energy cases, the NNPS presents significant higher values near the zero frequency, where the deterministic noise component prevails. This aspect is highlighted in Figure 5.8 for the energy of 26 keV and for the condition of high flux.
NNPS results have been shown for the energy range 26-50 keV in Figure 5.9, distinguishing between low flux (around 1M counts/pixel/s) and high flux (around 3M counts/pixel/s). For low energies there is an almost ideal trend: NNPS about one (Poissonian statistical condition). However, at higher energies, the NNPS starts to degrade, probably due to a decrease in the efficiency of the detector.
Regarding the flux dependence, the NNPS graphs show a deviation from the ideal trend at higher fluxes for the same energy. The low and high flux values used for each energy are reported in Table 5.5. As can be seen, the high flux value is higher than the flux value for which the DECTRIS count-rate correction becomes important (deviation greater than or equal to 5% from linearity for flux values for which the DECTRIS count-rate correction is not applied). This value of flux is reported for each energy studied in Table 5.3. The degradation of the NNPS at high fluxes could therefore be due to the fact that the detector is no longer locally linear and deviates more and more from the Poisson statistic.
In Figure 5.9a the dataset at 26 keV is systematically below one and this could be due to statistical uncertainties related to the flux or to an over-correction of the data by the Savitzky-Golay filter.
The low-flux 80 keV NNPS, as expected, is greater than 1 and in particular it takes on greater values than NNPSs in the 26-50 keV energy range.

Thus, in general, it has been noted that at approximately equal fluxes, there is a degradation of the NNPS from the ideal constant trend equal to 1 as the energy increases, while at equal energy the NNPS deviates from the ideal trend as the flux increases.

6.1.4. DQE

DQE is a key performance parameter for digital X-ray detectors as it is a frequency-dependent measure of the efficiency of the system in reproducing the information contained in the incident X-ray signal. It has been calculated by dividing the MTF by the NNPS at each spatial frequency. As can be observed from the results reported in Figure 5.11 for the energy range of 26-50 keV, a decrease of the DQE with energy for the same flux is observed. This behaviour is expected because as the energy increases, there is a loss of the detector efficiency, as shown in Figure 2.12. Especially for the energies of 30 keV and 33 keV the trend of the DQE curve decreases more abruptly, corresponding to the presence of the K-edges of Cd and Te. The decrease in DQE with flux, on the other hand, is due to the behaviour of the NNPS. Contributing to this decrease of the DQE could also be a degradation of the output signal, probably due to the automatic corrections implemented by DECTRIS.
The DQE trend for the 80 keV energy at low flux, reported in Figure 5.12, reflects the considerations just made. Comparing it with the DQEs in the energy range 26-50 keV at low flux, it is lower.

In the light of these results, it becomes clear that it is worth working with fluxes of the order of the low ones identified in this thesis (counts around 1M counts/pixel/s), thanks to which higher DQE values can be achieved. Moreover, higher DQE values would be of particular importance for example for in vivo imaging, where the dose delivered to the sample must be as low as possible.

6.2. EIGER2 stability

6.2.1. At startup

The stability of the detector at its startup has been studied with the purpose of understanding after how long the detector reaches stability after being initialized through an HV reset. In detail, 8 HV resets were performed one hour apart. The leakage current values of the sensor has been recorded and the result of the measurement is shown in Figure 5.13. From this measurement it was observed that at least 1 hour has to elapse before starting to acquire data with the detector. Furthermore, the repeatability of this action was noted: following an HV reset the current shows the same trend. These results are very important for the purposes of a medical imaging experiment since this leakage current generally results in unwanted electronic noise which can affect the resultant energy and quantum efficiency of the detector.

6.2.2. During a CT scan

The aim of this experiment is to check whether the detector reaches stability during irradiation in a time compatible with a tomographic scan and to find out if repeated tomographic scans, a typical medical imaging experiment, are reproducible or not. The procedure, which has been deeply explained in Section 4.2.2, briefly consists of performing an HV reset of the detector and waiting one hour for the detector to stabilise, then irradiating the detector three times and waiting a certain period of time between irradiations (T_{sleep}). The latter parameter simulates a dead time between consecutive tomographic scans. In order to determine what was intended, average counts normalised for the current at the initial instant of irradiation have been reported for each CT in the previous chapter. This current normalization has been necessary to correctly interpret the time dependency of the counts of the detector since the ring current, and therefore the intensity of the impinging flux, changes with time. Actually, the initial idea was to acquire for each flat-field image the corresponding ring current so as to have a more accurate normalisation. However, due to an error in the acquisition macro this has not been possible and just the current at the beginning and at the end of the radiation minute have been acquired. The percentage variation between the two current values has been found of the order of 1-2$^{o}/_{oo}$ for all the conditions studied.
In particular, two different energies have been studied, 33 keV and 50 keV, and for each energy two flux conditions (high and low) have been considered. In particular, the values of the flux have been chosen from the results of the previous experimental set of measurements. In this experiment, which as already mentioned reflects a typical tomography experiment, the high flux represents the white-field while the low flux the transmission through a sample. In Figure 5.14 are reported the results for the energy of 33 keV, while in Figure 5.15 those for the energy of 50 keV. These results have been obtained for values of T_{sleep} of 1 and 5 minutes.
The discussion of these results, reported below, is not intended as a rigorous treatment since it would require a very thorough knowledge of solid state, which the writer of this thesis does not possess. Therefore, an attempt has been made to give a possible interpretation of what has been observed experimentally by means of the knowledge acquired during the period of this thesis work. For the interpretation of the results, reference will be made primarily to the electron-generated signal, since according to Barrett et al. [23] if the pixel size is small compared to the detector thickness, the signal is almost all given by electron transport. For the first CT (red one), for all the energies and fluxes, an initial increase phase of the normalized mean counts has been observed. At this stage, the detector has just been reset and hence almost all its traps are free. By irradiating

the detector, there is a good chance that the electrons created at the beginning will be trapped in deep trap states, which according to the literature can have detrapping times in the order of minutes if not hours. It is therefore clear that at the beginning, due to this phenomenon of trapping of the charge, less charge will arrive at the collecting electrode and therefore a lower signal will be obtained. For the energy of 33 keV (Figure 5.14), this initial increase is not observed for the subsequent irradiations, CT2 and CT3, as the hostile traps may still be full. It is possible to start observing the initial growth in the consecutive CTs if longer T_{sleep} times (5 minutes) are waited, since these traps may start to be freed (Figure 5.14b).
For low fluxes (Figure 5.14a and 5.14b) a fairly stable zone is reached after a certain transient for all the CTs, while for higher fluxes (Figure 5.14c and 5.14d) a much more pronounced decrease is observed. One hypothesis for this decrease in the average counts is that this is due to a slight onset of polarization (refer to Section 2.1.4). At high fluxes, in fact, the number of charge generated is higher than at low fluxes and therefore, with the same number of traps present in the material, these traps will fill earlier and in higher quantity. When all traps are filled, the charges generated by the incident photon could start to accumulate in the sensor material distorting the electric field, hence the possible beginning of polarization of the sensor itself. This surplus of charge could occur already starting from the first irradiation when dealing with high fluxes and will be present for the following CTs.
Globally, in all the graphs obtained for the energy of 33 keV very small variations in the mean normalized counts have been observed. The largest variation noted is on the order of $6^o/_{oo}$. Therefore, the detector can be considered stable on average for this energy.

Similar results have been obtained for the energy of 50 keV (Figure 5.15). In general, the initial growth is observed for the first CT (red one), consistent with the fact that the detector has just been reset and the traps are almost all free. For low fluxes (Figure 5.15a and 5.15b) the plateau of counts, corresponding to a zone of stability, is reached in a longer time than at the energy of 33 keV. In particular, this is not completely reached within one minute of irradiation. Instead, for the high fluxes (Figure 5.15c and 5.15d) a slight decrease in counts is visible, most likely also here caused by an onset of polarization due to an accumulation of charges in the sensor. An interpretation of what happens at 50 keV is however more difficult than at 33 keV. In this case, in fact, unlike what happens for the energy of 33 keV, where the charge is created in the surface layer of the sensor, there is the creation of electron-hole pairs in almost the entire thickness of the sensor. It would also be appropriate to investigate the behavior of the holes since, in this case, they could give a greater contribution to the signal than in the case of 33 keV or give rise

to greater phenomena of recombination since, being created deeper, must cross a greater thickness of material to reach the cathode (in our case near the surface of the detector). A Monte Carlo simulation might be a good way to study in detail the behavior of the charge inside the sensor. Moreover, in order to compare the results at the two energies in a more accurate way, it would be appropriate to compare them in terms of dose, analyzing how many electrons are created per incident photon.
However, also for this energy, variations very small, at most 1% in the mean normalized counts, have been observed. Thus, on average, the detector can be considered stable also at this energy.

In light of the results just presented, it has been decided to see whether stable average counts correspond to a stable image. Thus, the idea was to observe whether or not in the wf images acquired changes occurred during an irradiation, i.e., to see if any structures appear within the image or not. To study this, the ratio between the wf image at the end of the 1 minute irradiation for one CT and the wf image at time 0 (beginning of irradiation) for the same CT has been performed. In Figures 5.16 and 5.17 the results for the energy of 33 keV and 50 keV, respectively, are shown. Again, as with the previous analysis, the high and low flux conditions, various T_{sleep} times, and three consecutive irradiations (CT1, CT2, and CT3) have been analyzed for each energy.
For the low flux condition for both energies, no distinctive structures have been observed in the wf images. This reflects the fact that not all traps have been filled yet. This is in accordance with the previous assumption: the distortion of the electric field in the sensor occurs when all or most of the traps have been filled and an accumulation of fixed charge in the material begins. At high fluxes, where it is expected to have filled all the traps and therefore to have fixed charge in the material, leading to a distortion of the electric field, the appearance of structures around the edges between the grains is observed. In particular, various lines with increased count rate, surrounded by lines of decreased count rate have been observed. This is in agreement with what Ruat et Ponchut [31] noted by irradiating continuously their CdTe sensor. Investigating in more detail, it has been found that there is a prevalent accumulation of charge around these structures but also randomly in regions of the sensor where these structures are not present. An attempt has been made to quantify these local variations in pixel counts and came-up with a value of about 5-6%. This observed intrinsic variability of the sensor could lead to problems in a typical K-edge subtraction experiment for which the detector was mainly intended. In fact, when a normalisation has to be made for the initial value of a pixel, if it has undergone a higher or lower variation of, for example, 5%, it will lead to conclude that in that pixel there is a concentration of the contrast agent of more or less than 5% compared

to the average. In addition, this strong local variability could also lead to artefacts in the images.

In order to complete this stability study and verify the hypotheses formulated above, the dataset has been enlarged by considering longer T_{sleep} times: 10 and 20 minutes. This has been done just for the energy of 33 keV due to timing issues. The final results are reported in Figures 5.18 and 5.19. As expected, an early growth phase in the normalized mean counts has been observed for all CTs at all conditions studied, indicating that by waiting longer times between successive irradiations the traps have time to release the previously trapped charge. Again, for low fluxes a region of stability of counts is observed after a certain period of time while for high fluxes a decreasing of counts is observed, most likely related to an onset of polarization. The largest variation noted in this case for the mean counts is on the order of $6^o/_{oo}$. Therefore, the detector can be considered stable on average for this energy for the conditions studied. Consistent with previous observations, the appearance of structures around the grains has been noted for high fluxes, around which local variations in pixel counts of the order of 5-6% have been observed. These local variations in pixel counts have been observed randomly even in regions where such structures are not present, thus leading to findings of intrinsic sensor variability.

7 | Conclusions and future developments

The ID17 biomedical beamline of the ESRF has been recently equipped with a DECTRIS EIGER2 CdTe 1M X detector, in the frame of a beamline instrumentation upgrade project. Although this new family of hybrid single-photon counting detectors is primarily designed for X-ray diffraction, X-ray scattering and spectroscopy experiments, the goal of ID17 is to use the detector for biomedical imaging. Hence, an accurate characterization became necessary to understand both its performances and its compatibility in typical experiments, such as tomographic scans and K-edge subtraction. This characterization was the purpose of the thesis work. In particular, the study has been split into two main parts: the determination of the performances of the detector in terms of linearity, MTF, NPS and DQE and the determination of the detector stability at its startup and during a typical CT experiment. Due to some limitations encountered, fully explained in the various chapters, it was often not possible to follow standard and well-established methods in the literature but readjustments of these were necessary.

Concerning the first part of the characterization, related to the determination of the detector performance, all measurements were performed for the energy range 26-51 keV, which is a typical range used for medical imaging experiments. In particular, two flux conditions, high (3M counts/pixel/s) and low (1M counts/pixel/s), were studied. The characterization was then partially extended to high energies, in particular to the energy of 80 keV, in view of possible medical imaging applications related for example to the presence of the gold K-edge at this energy. However, at 80 keV only low fluxes were analyzed, to avoid sensor polarization.
As far as the study of the linearity of the detector is concerned, it has been observed that, enabling the automatic count-rate correction of DECTRIS, the detector shows a deviation from the ideal behavior around 30 keV, attributable to the presence of the K-edges of Cd and Te. Disabling instead the automatic count-rate correction, there is a deviation from linearity greater than or equal to 5% from a flux of the order of $3x10^8$, especially for the energy range 28-51 keV. In view of a medical imaging experiment, it is advisable

to keep the count-rate correction enabled, so as to take advantage of a linear behavior of the detector.
The determination of the MTF was performed using the slanted-edge method and the results obtained led to the conclusion that, in order to have a correct characterization of the detector in frequency, it is necessary to refer to the MTF, rather than the LSF. In fact, the LSF gives for all the energies analyzed a value of FWHM of about 75 µm, which is required by DECTRIS, although an alteration of the frequency response is observed especially for energies where the contribution of fluorescence becomes important. In addition, a weak flux dependence was observed for the MTF. A new fit model for the ESF, resulting from an internal collaboration with the ESRF Detector group, has been tested. This fit model for the ESF, compared to those found in the literature, considers the phenomenon of fluorescence. For the energies where this phenomenon is present, the inclusion of fluorescence in the model has led to improved results. In addition, through a study of the fit parameters, it was found that they exhibit reasonable physical significance. Regarding the NNPS, a degradation of it was observed as the energy increases for the same flux. Deviation from the ideal trend also occurs for flux values (at the same energy) for which the DECTRIS correction of count-rate becomes important.
To conclude this first part, the DQE has been calculated. This is a key parameter for digital X-ray detectors as it provides a measure of the efficiency of the system in reproducing the information contained in the incident X-ray signal. It was found that the DQE decreases with increasing energy at the same flux and especially for energies where the contribution of fluorescence becomes important. Instead, at the same energy the DQE degrades with increasing flux probably due to the importance that the count-rate correction begins to assume. In light of these results, it becomes clear that it is convenient to operate this detector for medical imaging purposes at relatively low fluxes, on the order of 1M counts/pixel/s.

The second part of the characterization of the detector involved the study of its stability. In the light of the results obtained, it was found that it is appropriate to perform an HV reset before starting to acquire data and that it is necessary to wait at least one hour for the detector to stabilize. During this hour, the leakage current of the detector decreases until it reaches an asymptotic value according to a repeatable trend over time. Having a leakage current as low as possible during an imaging experiment is very important because this current generally results in unwanted electronic noise, which can have consequences on the quantum efficiency of the detector. Finally, regarding the study of the stability of the detector during a typical CT experiment, it was observed that for low fluxes and for both energies studied, 33 keV and 50 keV, a plateau of the average counts is reached after

about 30 seconds from the beginning of the irradiation (detector reset at the beginning). In light of this, since it is very important to have a stable detector during a CT experiment, also to avoid artifacts in the image that can lead to misinterpretation, it is advisable to pre-irradiate the detector before starting to acquire images. For high fluxes the plateau of the counts is observed only for a short time interval, followed by a slight decrease in counts most likely due to an onset of polarization. Considering the results obtained, it can be concluded that tomographic scans repeated in time are reproducible, especially when relatively long times (10-20 minutes) are waited between consecutive irradiations. With this analysis, it has also been observed that the detector can be considered on average stable (global variations of counts between $6^o/_{oo}$ and 1%) at the energies studied while locally larger variations, of the order of 5%, were found in accordance with the appearance of structures in the wf images. The global stability of the detector plays in favor of CT experiments while the local variability of the detector leads to difficulties in applying the technique of KES.

This detailed characterization has allowed to begin to understand the limitations of the detector relative to typical medical imaging experiments performed in ID17. Important results have been obtained but further investigations are needed to have a complete understanding of the detector operation. For example, it would be worthwhile to study in more detail the corrections applied by DECTRIS and understand how these may affect the measurements. As mentioned earlier, in this thesis the study of the behavior of the detector at 80 keV for low fluxes was started, but, due to time issues, the work was not completed. It is therefore of great importance to conclude this study both to have a complete characterization dataset of the detector but also in view of medical applications related to the presence of the K-edge of gold nano-particles.

Bibliography

[1] S. Hulbert and G. Williams, "1. synchrotron radiation sources," in *Vacuum Ultraviolet Spectroscopy I* (J. Samson and D. Ederer, eds.), vol. 31 of *Experimental Methods in the Physical Sciences*, pp. 1–25, Academic Press, 1998. https://www.sciencedirect.com/science/article/pii/S0076695X08600356.

[2] F. R. Elder, A. M. Gurewitsch, R. V. Langmuir, and H. C. Pollock, "Radiation from electrons in a synchrotron," *Phys. Rev.*, vol. 71, pp. 829–830, Jun 1947.

[3] ESRF, "What is a synchrotron?," 2019. https://www.esrf.fr/about/synchrotron-science/synchrotron.

[4] A. Bharti and N. Goyal, "Synchrotron radiation - useful and interesting applications: Fundamental of synchrotron radiations," 2019.

[5] P. Raimondi, "Esrf-ebs: The extremely brilliant source project," 2016.

[6] ESRF, "Esrf-ebs opens to users," 2020.

[7] D.Morel/ESRF, "Aerial view of esrf." 2005.

[8] ESRF, "Filling modes," Jan 2017.

[9] G. E. Barbone, A. Bravin, P. Romanelli, A. Mittone, D. Bucci, T. Gaaβ, G. Le Duc, S. Auweter, M. F. Reiser, M. J. Kraiger, and et al., "Micro-imaging of brain cancer radiation therapy using phase-contrast computed tomography," *International Journal of Radiation Oncology*Biology*Physics*, vol. 101, no. 4, p. 965–984, 2018.

[10] L. Porra, L. Broche, L. Dégrugilliers, G. Albu, I. Malaspinas, C. Doras, M. Wallin, M. Hallbäck, W. Habre, S. Bayat, and et al., "Synchrotron imaging shows effect of ventilator settings on intrabreath cyclic changes in pulmonary blood volume," *American Journal of Respiratory Cell and Molecular Biology*, vol. 57, no. 4, p. 459–467, 2017.

[11] A. Horng, E. Brun, A. Mittone, S. Gasilov, L. Weber, T. Geith, S. Adam-Neumair,

S. D. Auweter, A. Bravin, M. F. Reiser, and et al., "Cartilage and soft tissue imaging using x-rays," *Investigative Radiology*, vol. 49, no. 9, p. 627–634, 2014.

[12] H. Smilowitz, H. Blattmann, E. Bräuer-Krisch, A. Bravin, M. D. Michiel, J.-O. Gebbers, A. L. Hanson, N. Lyubimova, D. N. Slatkin, J. Stepanek, and et al., "Synergy of gene-mediated immunoprophylaxis and microbeam radiation therapy for advanced intracerebral rat 9l gliosarcomas," *Journal of Neuro-Oncology*, vol. 78, no. 2, p. 135–143, 2006.

[13] E. Bräuer-Krisch, H. Requardt, P. Régnard, S. Corde, E. Siegbahn, G. LeDuc, T. Brochard, H. Blattmann, J. Laissue, A. Bravin, and et al., "New irradiation geometry for microbeam radiation therapy," *Physics in Medicine and Biology*, vol. 50, no. 13, p. 3103–3111, 2005.

[14] I. Martínez-Rovira, J. Sempau, and Y. Prezado, "Development and commissioning of a monte carlo photon beam model for the forthcoming clinical trials in microbeam radiation therapy," *Medical Physics*, vol. 39, no. 1, p. 119–131, 2012.

[15] A. Mittone, L. Fardin, F. Di Lillo, M. Fratini, H. Requardt, A. Mauro, R. A. Homs-Regojo, P.-A. Douissard, G. E. Barbone, J. Stroebel, M. Romano, L. Massimi, G. Begani-Provinciali, F. Palermo, S. Bayat, A. Cedola, P. Coan, and A. Bravin, "Multiscale pink-beam microCT imaging at the ESRF-ID17 biomedical beamline," *Journal of Synchrotron Radiation*, vol. 27, pp. 1347–1357, Sep 2020.

[16] ESRF, "Overview," 2017.

[17] H. Elleaume, A. Charvet, P. Berkvens, G. Berruyer, T. Brochard, Y. Dabin, M. Dominguez, A. Draperi, S. Fiedler, G. Goujon, and et al., "Instrumentation of the esrf medical imaging facility," *Nuclear Instruments and Methods in Physics Research Section A: Accelerators, Spectrometers, Detectors and Associated Equipment*, vol. 428, no. 2-3, p. 513–527, 1999.

[18] N. Wermes, "Pixel detectors for particle physics and imaging applications," *Nuclear Instruments and Methods in Physics Research Section A: Accelerators, Spectrometers, Detectors and Associated Equipment*, vol. 512, no. 1-2, p. 277–288, 2003.

[19] N. Wermes, "Pixel detectors for tracking and their spin-off in imaging applications," *Nuclear Instruments and Methods in Physics Research Section A: Accelerators, Spectrometers, Detectors and Associated Equipment*, vol. 541, no. 1-2, p. 150–165, 2005.

[20] R. W. Rossi, Fischer, *Pixel Detectors*. Springer, 2006.

[21] G. F. Knoll, *Radiation Detection and Measurement - 4th edition.* John Wiley & Sons Inc, 2010.

[22] Spieler, *Semiconductor Detector Systems.* Oxford University Press, 2005.

[23] H. H. Barrett, J. D. Eskin, and H. B. Barber, "Charge transport in arrays of semiconductor gamma-ray detectors," *Physical Review Letters*, vol. 75, no. 1, p. 156–159, 1995.

[24] J. Noras, M. Raad, and M. Deriche, "Pile-up free parameter estimation and digital online peak localization algorithms for gamma ray spectroscopy."

[25] K. Taguchi, M. Zhang, E. C. Frey, X. Wang, J. S. Iwanczyk, E. Nygard, N. E. Hartsough, B. M. Tsui, and W. C. Barber, "Modeling the performance of a photon counting x-ray detector for ct: Energy response and pulse pileup effects," *Medical Physics*, vol. 38, no. 2, p. 1089–1102, 2011.

[26] Z. Zhang, Y. Ma, S. Li, P. Zhao, Y. Xiang, X. Liu, and W. Zhang, "Ranging performance model considering the pulse pileup effect for pmt-based photon-counting lidars," *Optics Express*, vol. 28, no. 9, p. 13586, 2020.

[27] E. Kalemci and J. Matteson, "Investigation of charge sharing among electrode strips for a cdznte detector," *Nuclear Instruments and Methods in Physics Research Section A: Accelerators, Spectrometers, Detectors and Associated Equipment*, vol. 478, no. 3, p. 527–537, 2002.

[28] D. Pennicard and H. Graafsma, "Simulated performance of high-z detectors with medipix3 readout," *Journal of Instrumentation*, vol. 6, no. 06, 2011.

[29] A. Förster, S. Brandstetter, and C. Schulze-Briese, "Transforming x-ray detection with hybrid photon counting detectors," *Philosophical Transactions of the Royal Society A: Mathematical, Physical and Engineering Sciences*, vol. 377, no. 2147, p. 20180241, 2019.

[30] L. Ren, B. Zheng, and H. Liu, "Tutorial on x-ray photon counting detector characterization," *Journal of X-Ray Science and Technology*, vol. 26, no. 1, p. 1–28, 2018.

[31] M. Ruat and C. Ponchut, "Characterization of a pixelated cdte x-ray detector using the timepix photon-counting readout chip," *IEEE Transactions on Nuclear Science*, vol. 59, pp. 2392–2401, 2012.

[32] D. Pennicard, S. Sengelmann, S. Smoljanin, H. Hirsemann, and H. Graafsma, "De-

velopment of High -Z Sensors for Pixel Array Detectors," *PoS*, vol. VERTEX 2010, p. 027, 2011.

[33] L. Tlustos, M. Campbell, E. H. M. Heijne, and X. Llopart, "Signal variations in high-granularity si pixel detectors," *IEEE Transactions on Nuclear Science*, vol. 51, pp. 3006–3012, 2004.

[34] D. Pennicard, S. Smoljanin, B. Struth, H. Hirsemann, A. Fauler, M. Fiederle, O. Tolbanov, A. Zarubin, A. Tyazhev, G. Shelkov, and et al., "The lambda photon-counting pixel detector and high-z sensor development," *Journal of Instrumentation*, vol. 9, no. 12, 2014.

[35] NIST, "Energies of elemental K-edges."

[36] X. Wang, D. Meier, S. Mikkelsen, G. E. Maehlum, D. J. Wagenaar, B. M. W. Tsui, B. E. Patt, and E. C. Frey, "MicroCT with energy-resolved photon-counting detectors," *Physics in Medicine and Biology*, vol. 56, pp. 2791–2816, apr 2011.

[37] DECTRIS, "EIGER2 for Synchrotrons."

[38] DECTRIS, "EIGER2 for Laboratories."

[39] DECTRIS, "ID15B at ESRF for high-pressure experiments," 2021.

[40] DECTRIS, "A DECTRIS, EIGER2 X CdTe 4m at the ESRF beamline ID11," 2021.

[41] DECTRIS, "Technical specifications DECTRIS EIGER2 X CdTe 1M-W," 2021.

[42] R. et al., "Eiger2 x 1m-w cdte detector for id17: Report on site acceptance tests," 2020.

[43] DECTRIS, "EIGER2 X CdTe," 2018.

[44] M. Bochenek, S. Bottinelli, C. Broennimann, P. Livi, T. Loeliger, V. Radicci, R. Schnyder, and P. Zambon, "Ibex: Versatile readout asic with spectral imaging capability and high count rate capability," *IEEE Transactions on Nuclear Science*, vol. 65, pp. 1285–1291, 2018.

[45] T. Loeliger, C. Brönnimann, T. Donath, M. Schneebeli, R. Schnyder, and P. Trüb, "The new pilatus3 asic with instant retrigger capability," in *2012 IEEE Nuclear Science Symposium and Medical Imaging Conference Record (NSS/MIC)*, pp. 610–615, 2012.

[46] DECTRIS, "SIMPLON 1.8 API reference," 2020.

[47] "Lima: Acquiring data with imaging detectors," Jan 2017.

[48] DECTRIS, "SIMPLON 1.6 API reference," 2018.

[49] R. Bourne, *Fundamentals of Digital Imaging in Medicine*. Springer, 2010.

[50] M. J. Willemink, M. Persson, A. Pourmorteza, N. J. Pelc, and D. Fleischmann, "Photon-counting ct: Technical principles and clinical prospects," *Radiology*, vol. 289, no. 2, p. 293–312, 2018.

[51] S. N. Ahmed, "Position-sensitive detection and imaging," *Physics and Engineering of Radiation Detection*, p. 435–475, 2015.

[52] M. Muñoz, *Digital radiography: image acquisition and scattering reduction in x-ray imaging*. PhD thesis, 2019.

[53] M. J. Yaffe and J. A. Rowlands, "X-ray detectors for digital radiography," *Physics in Medicine and Biology*, vol. 42, pp. 1–39, jan 1997.

[54] H. Fujita, D.-Y. Tsai, T. Itoh, K. Doi, J. Morishita, K. Ueda, and A. Ohtsuka, "A simple method for determining the modulation transfer function in digital radiography," *IEEE Transactions on Medical Imaging*, vol. 11, no. 1, p. 34–39, 1992.

[55] I. A. Cunningham and A. Fenster, "A method for modulation transfer function determination from edge profiles with correction for finite-element differentiation," *Medical Physics*, vol. 14, no. 4, p. 533–537, 1987.

[56] E. Samei, M. J. Flynn, and D. A. Reimann, "A method for measuring the presampled MTF of digital radiographic systems using an edge test device," *Medical Physics*, vol. 25, no. 1, p. 102–113, 1998.

[57] "International Standard - Medical electrical equipment – Characteristics of digital X-ray imaging devices – Part 1: Determination of the detective quantum efficiency," 2003.

[58] "10. Spatial Resolution in CT," *Journal of the ICRU*, vol. 12, no. 1, pp. 107–120, 2012.

[59] M. B. Williams, P. A. Mangiafico, and P. U. Simoni, "Noise Power Spectra of images from Digital Mammography detectors," *Medical Physics*, vol. 26, no. 7, p. 1279–1293, 1999.

[60] R. B. Blackman and J. W. Tukey, "The measurement of power spectra from the point of view of communications engineering — part i," *The Bell System Technical Journal*, vol. 37, no. 1, p. 185–282, 1958.

[61] S. Dolly, H.-C. Chen, M. Anastasio, S. Mutic, and H. Li, "Practical considerations for noise power spectra estimation for clinical ct scanners," *Journal of Applied Clinical Medical Physics*, vol. 17, no. 3, p. 392–407, 2016.

[62] H. Illers, D. Vandenbroucke, and E. Buhr, "Measurement of correlated noise in images of computed radiography systems and its influence on the detective quantum efficiency," *SPIE Proceedings*, 2004.

[63] P. J. Withers, C. Bouman, S. Carmignato, V. Cnudde, D. Grimaldi, C. K. Hagen, E. Maire, M. Manley, A. Du Plessis, S. R. Stock, and et al., "X-ray computed tomography," Feb 2021.

[64] W. Maire, "Quantitative x-ray tomography," 2013.

[65] Z. Messali, "A comparative study of analytical, iterative and Bayesian reconstruction algorithms in Computed Tomography (CT)," *International Journal of Computer and Communication Engineering*, p. 222–226, 2012.

[66] P. P. Bruyant, "Analytic and iterative reconstruction algorithms in SPECT," *Journal of nuclear medicine : official publication, Society of Nuclear Medicine*, vol. 43 10, pp. 1343–58, 2002.

[67] A. Kak and M. Slaney, *Principles of computerized tomographic imaging*. IEEE PRESS, 2001.

[68] "X-ray Computed Tomography," 2019.

[69] "Dichromatic absorption radiography. Dichromography."

[70] S. Bayat, L. Porra, H. Suhonen, C. Nemoz, P. Suortti, and A. R. Sovijärvi, "Differences in the time course of proximal and distal airway response to inhaled histamine studied by synchrotron radiation ct," *Journal of Applied Physiology*, vol. 100, no. 6, p. 1964–1973, 2006.

[71] S. Bayat, L. Porra, P. Suortti, and W. Thomlinson, "Functional lung imaging with synchrotron radiation: Methods and preclinical applications," *Physica Medica*, vol. 79, pp. 22–35, 2020.

[72] H. Elleaume, S. Fiedler, F. Estève, B. Bertrand, A. M. Charvet, P. Berkvens, G. Berruyer, T. Brochard, G. L. Duc, C. Nemoz, M. Renier, P. Suortti, W. Thomlinson, and J. F. L. Bas, "First human transvenous coronary angiography at the European Synchrotron Radiation Facility," *Physics in Medicine and Biology*, vol. 45, pp. L39–L43, aug 2000.

[73] P. Suortti and W. Thomlinson, "Medical applications of synchrotron radiation," *Physics in Medicine and Biology*, vol. 48, pp. R1–R35, jun 2003.

[74] S. Bayat, G. L. Duc, L. Porra, G. Berruyer, C. Nemoz, S. Monfraix, S. Fiedler, W. Thomlinson, P. Suortti, C. G. Standertskjöld-Nordenstam, and A. R. A. Sovijärvi, "Quantitative functional lung imaging with synchrotron radiation using inhaled xenon as contrast agent," *Physics in Medicine and Biology*, vol. 46, pp. 3287–3299, nov 2001.

[75] A. Bravin, P. Coan, and P. Suortti, "X-ray phase-contrast imaging: from pre-clinical applications towards clinics," *Physics in Medicine and Biology*, vol. 58, pp. R1–R35, dec 2012.

[76] W. Thomlinson, H. Elleaume, L. Porra, and P. Suortti, "K-edge subtraction synchrotron x-ray imaging in bio-medical research," May 2018.

[77] ROOT, "Analyzing petabytes of data, scientifically."

[78] PTW, "Detectors for Ionizing Radiation."

[79] PTW, "Semiflex Ionization Chamber 31010."

[80] Y. Prezado, M. Vautrin, I. Martínez-Rovira, A. Bravin, F. Estève, H. Elleaume, P. Berkvens, and J. F. Adam, "Dosimetry Protocol for the forthcoming clinical trials in Synchrotron Stereotactic Radiation Therapy (SSRT)," *Medical Physics*, vol. 38, no. 3, p. 1709–1717, 2011.

[81] NIST, "X-ray mass attenuation coefficients - water, liquid."

[82] NIST, "X-ray mass attenuation coefficients - air, dry."

[83] M. Estribeau and P. Magnan, "Fast MTF measurement of CMOS imagers using ISO 12333 slanted-edge methodology," in *SPIE Optical Systems Design*, 2004.

[84] P. Zambon, V. Radicci, M. Rissi, and C. Broennimann, "A fitting model of the pixel response to monochromatic x-rays in photon counting detectors," *Nuclear Instruments and Methods in Physics Research Section A: Accelerators, Spectrometers, Detectors and Associated Equipment*, vol. 905, pp. 188–192, 2018.

[85] A. Savitzky and M. J. Golay, "Smoothing and differentiation of data by simplified least squares procedures.," *Analytical Chemistry*, vol. 36, no. 8, p. 1627–1639, 1964.

[86] R. W. Schafer, "What Is a Savitzky-Golay Filter? [Lecture Notes]," *IEEE Signal Processing Magazine*, vol. 28, no. 4, pp. 111–117, 2011.

[87] S. Hargittai, "Savitzky-Golay least-squares polynomial filters in ECG signal processing," in *Computers in Cardiology, 2005*, pp. 763–766, 2005.

[88] D. Acharya, A. Rani, S. Agarwal, and V. Singh, "Application of adaptive Savitzky–Golay filter for EEG signal processing," *Perspectives in Science*, vol. 8, pp. 677–679, 2016. Recent Trends in Engineering and Material Sciences.

[89] J. Li, H. Deng, P. Li, and B. Yu, "Real-time infrared gas detection based on an Adaptive Savitzky–Golay algorithm," *Applied Physics B*, vol. 120, no. 2, p. 207–216, 2015.

[90] J. T. *et al.*, "Decimo: A simulation tool to explore next generation of detectors for synchrotron radiation applications," *IEEE*, pp. 1–7, 2016.

[91] NIST, "X-ray mass attenuation coefficients - cadmium telluride."

[92] NIST, "X-ray mass attenuation coefficients - table 2."

A | Appendix A

Linearity

In this section are reported the plots related to the study of the intrinsic linearity of the detector. In Figure A.1 are shown the data flux for the count-rate correction on and off for the energy of 26 keV (A.1a), 28 keV (A.1b), 51 keV (A.1d) and 80 keV (A.1e). The trendlines added to the two datasets have been introduced just to help the reader with the visualization.

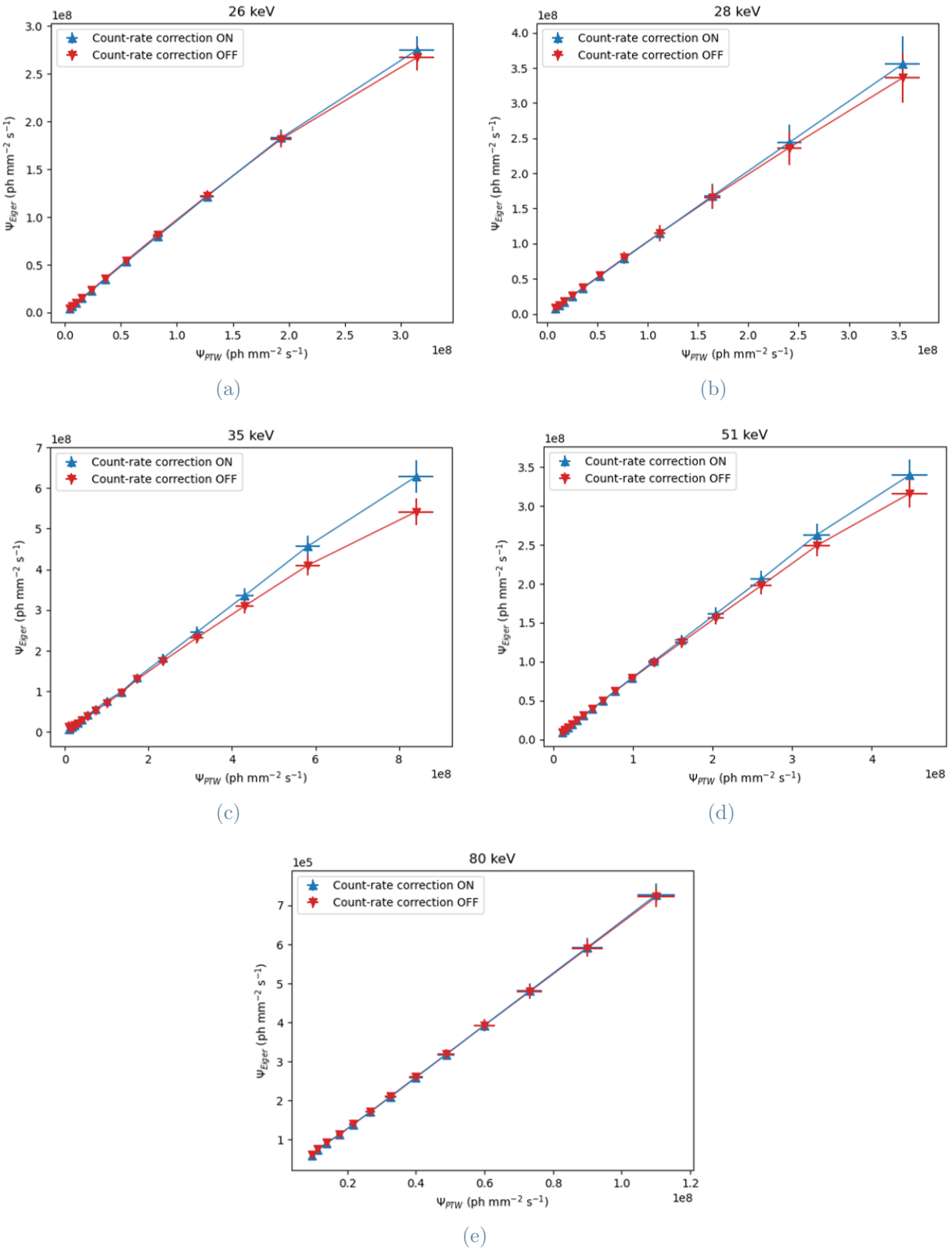

Figure A.1: Flux recorded by the EIGER2 detector vs the flux measured by a PTW ionization chamber placed upstream the detector for the energy of (a) 26 keV, (b) 28 keV, (c) 35 keV, (d) 51 keV and (e) 80 keV. In blue, the recorded values with the count-rate correction applied; in red the recorded values once the correction was switched off.

Vertical MTF

In this section are reported the graphs related to the determination of the vertical MTF of the EIGER2 detector. Figure A.2 shows the vertical ESF, LSF and MTF at 33 keV for the high flux condition. The vertical ESF, LSF and MTF for the energy of 26 keV (Figure A.3), 30 keV (Figure A.4) and 50 keV (Figure A.5), for the low and high flux condition, are also presented.

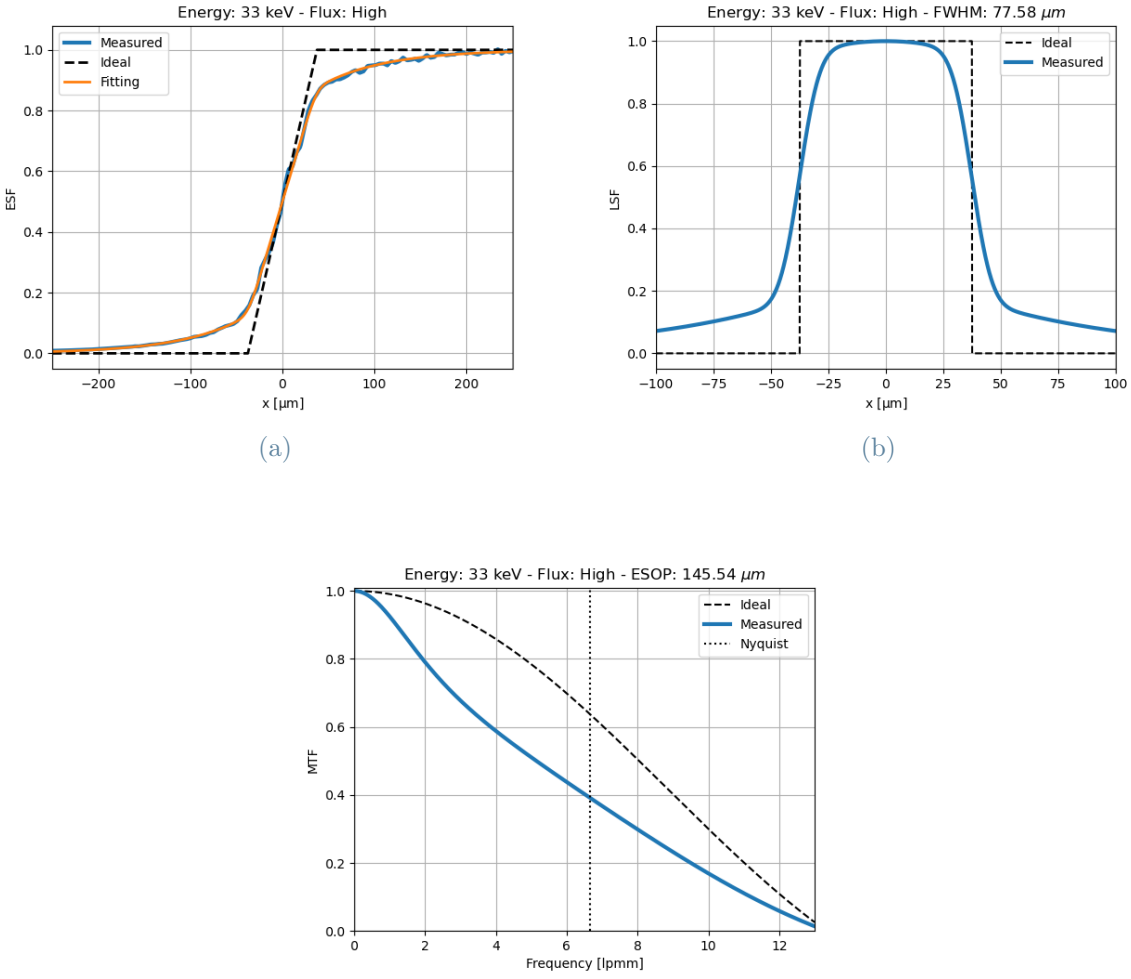

(a) (b)

(c)

Figure A.2: Vertical ESF, LSF and MTF for the energy of 33 keV for the high flux condition. For each function the measured and the ideal curves are plotted. For the ESF the fitting model is reported while for the MTF plot the Nyquist frequency is highlighted. Fluorescence is not included in the model.

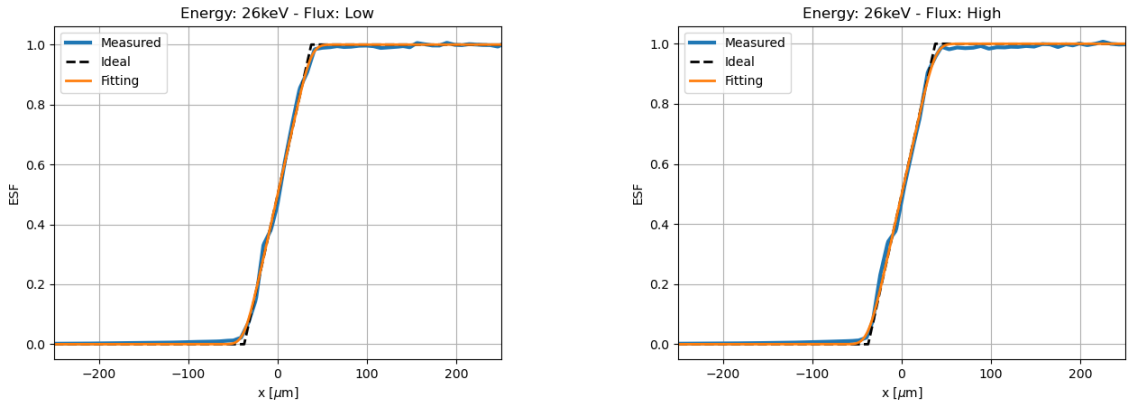

(a)

(b)

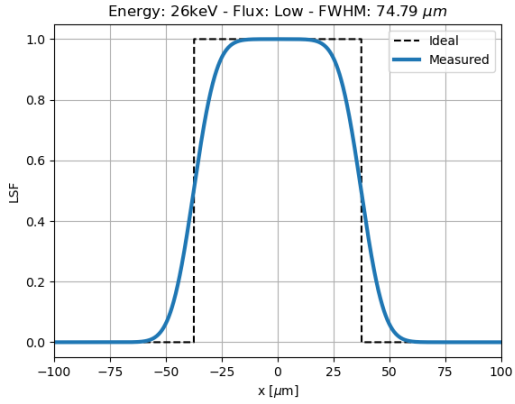

(c)

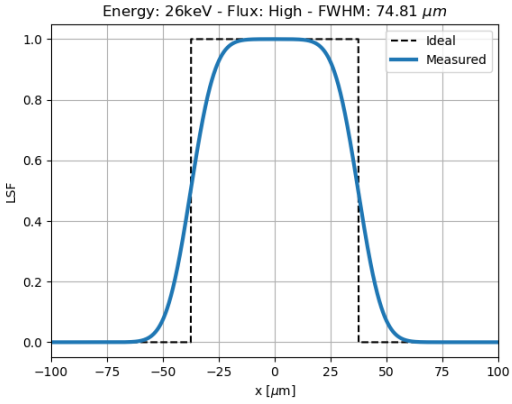

(d)

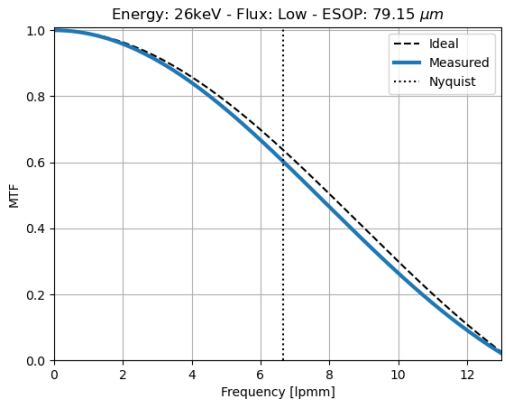

(e)

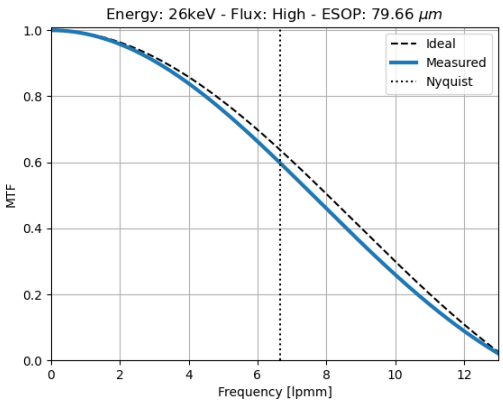

(f)

Figure A.3: Vertical ESF, LSF and MTF for the energy of 26 keV for the low (A.3a, A.3c, A.3e) and high (A.3b, A.3d, A.3f) flux condition. For each function the measured and the ideal curves are plotted. For the ESF the fitting model is reported while for the MTF plot the Nyquist frequency is highlighted. Fluorescence is not included in the model.

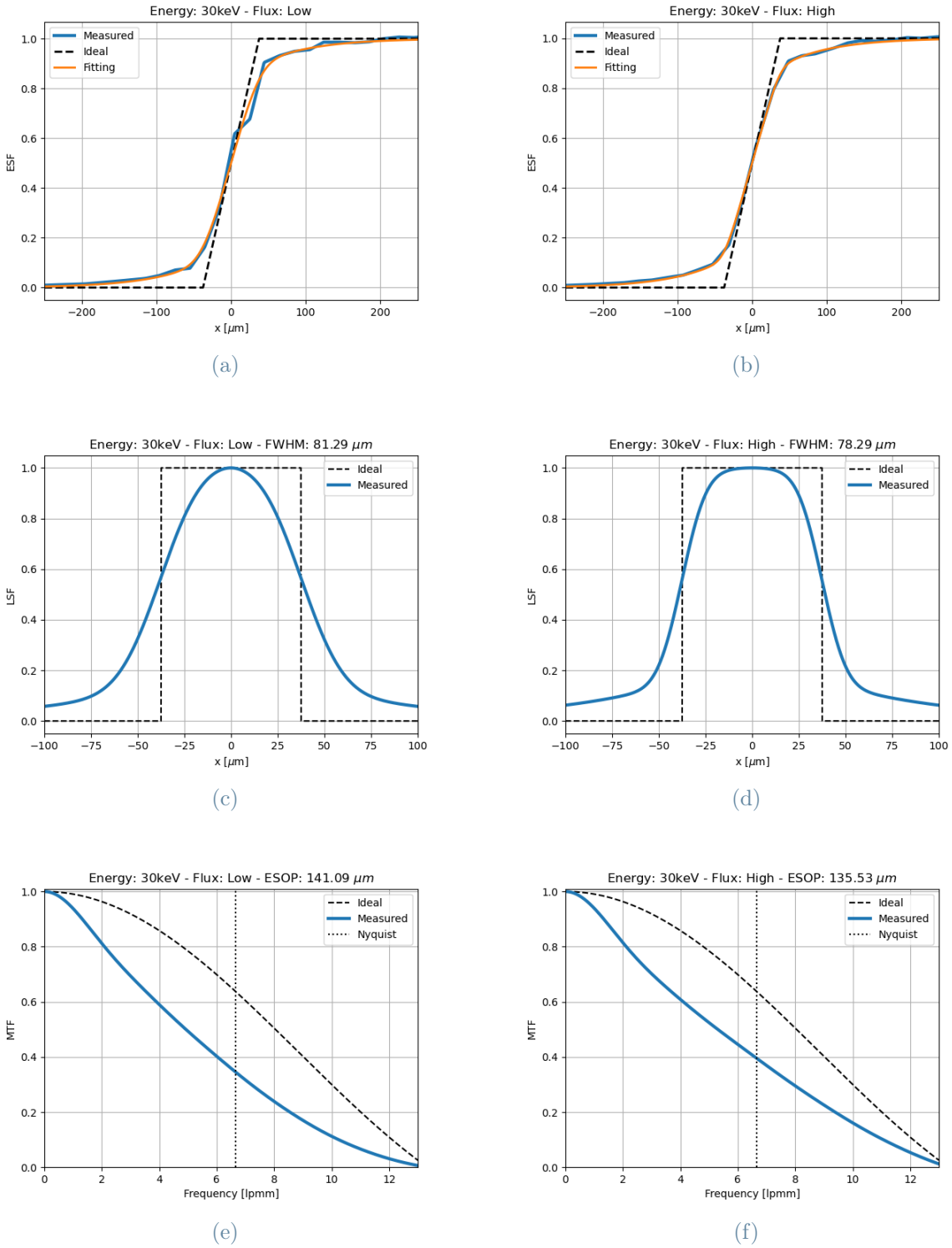

Figure A.4: Vertical ESF, LSF and MTF for the energy of 30 keV for the low (A.4a, A.4c, A.4e) and high (A.4b, A.4d, A.4f) flux condition. For each function the measured and the ideal curves are plotted. For the ESF the fitting model is reported while for the MTF plot the Nyquist frequency is highlighted. Fluorescence is included in the model.

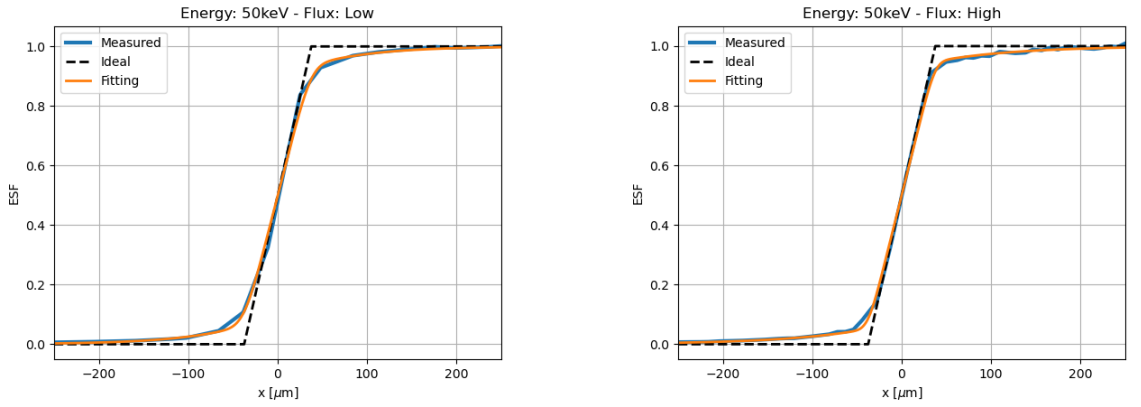

(a)

(b)

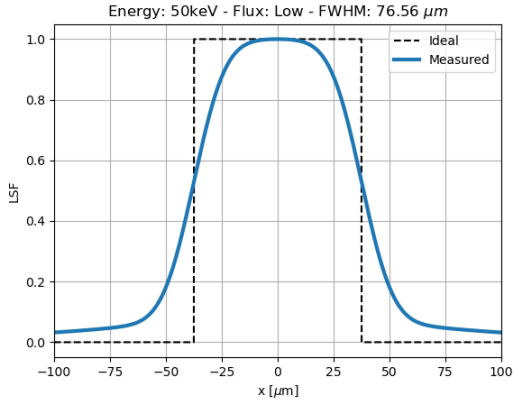

(c)

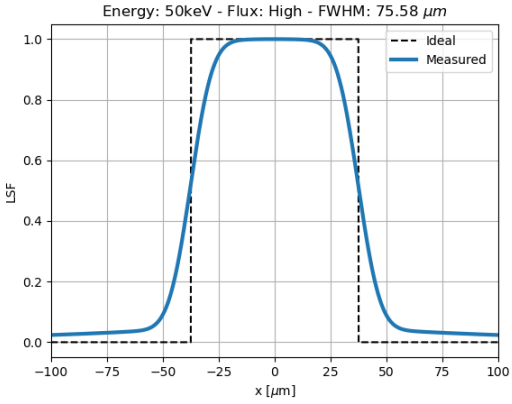

(d)

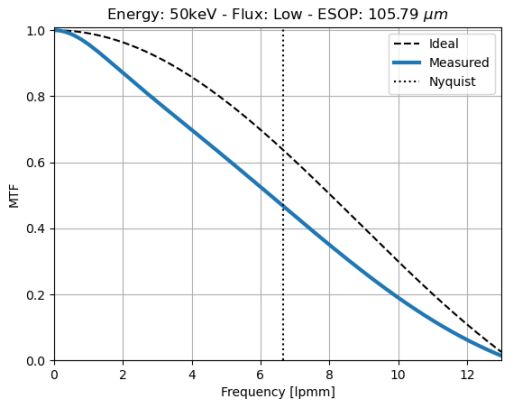

(e)

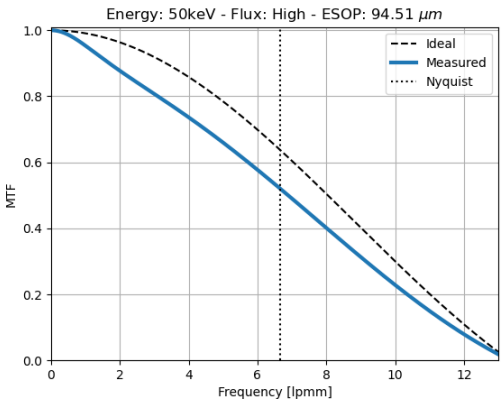

(f)

Figure A.5: Vertical ESF, LSF and MTF for the energy of 50 keV for the low (A.5a, A.5c, A.5e) and high (A.5b, A.5d, A.5f) flux condition. For each function the measured and the ideal curves are plotted. For the ESF the fitting model is reported while for the MTF plot the Nyquist frequency is highlighted. Fluorescence is included in the model.

Horizontal MTF

In this section are reported the graphs related to the determination of the horizontal MTF of the EIGER2 detector. As already explained in Chapter 4, it was not possible to get enough statistics for the horizontal MTF due to the limited vertical beam size. Therefore, the analysis performed in this thesis work was limited to the vertical MTF only. Nevertheless, the author wanted to report the graphs obtained.
The main results are summarised in Table A.1. For each condition of energy and flux the FWHM of the LSF and the ESOP are reported. The theoretical FWHM of the LSF should be equal to 75 µm, corresponding to the physical dimension of the pixel (75 µm). Nevertheless, in order to quantify the observed altered frequency response of the detector, especially for those energies where the fluorescence contribution is important, the ESOP parameter was introduced.

The horizontal ESF, LSF and MTF for the energy of 26 keV (Figure A.6), 30 keV (Figure A.7), 33 keV (Figure A.8), and 50 keV (Figure A.9), for the low and high flux condition, are reported. The horizontal ESF, LSF and MTF at 80 keV for the low flux condition are also presented in Figure A.10.

E [keV]	Flux [ph mm^{-2} s^{-1}]	LSF FWHM [µm]	ESOP [µm]
26	1.58×10^{8}	78.09	99.10
	5.56×10^{8}	77.10	96.06
30	2.41×10^{8}	81.56	145.84
	6.99×10^{8}	80.81	146.49
33	2.02×10^{8}	82.81	173.24
	7.25×10^{8}	82.06	163.30
50	1.95×10^{8}	76.56	105.79
	6.58×10^{8}	75.82	96.30
80	3.98×10^{7}	74.86	80.99

Table A.1: Final results obtained for the horizontal MTF. The values of the FWHM of the LSF and the values of the ESOP are reported for each energy value studied and for each flux condition. Around 1M counts/pixel/s and 3M counts/pixel/s have been considered to set the low and high flux condition for each energy respectively.

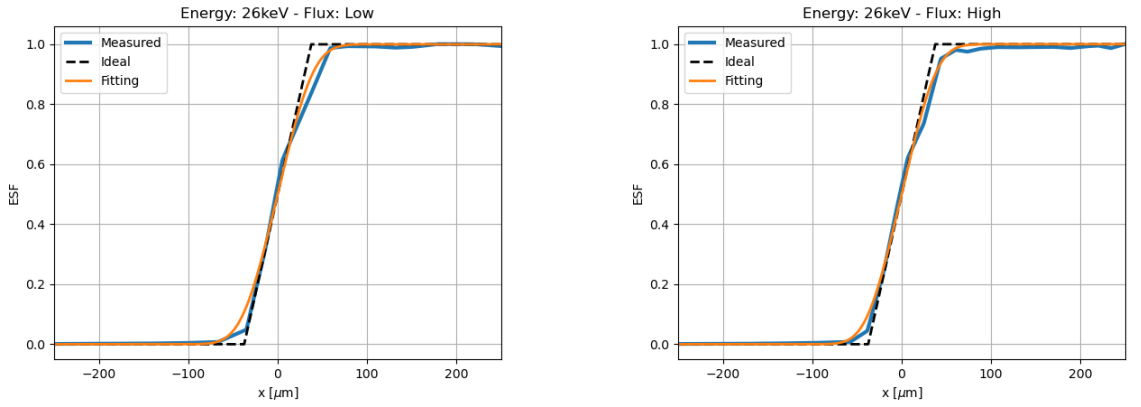

(a)

(b)

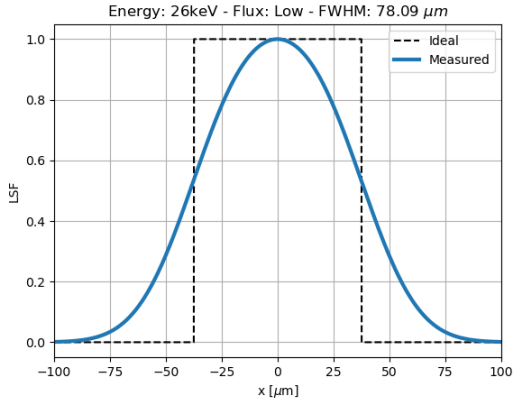

(c)

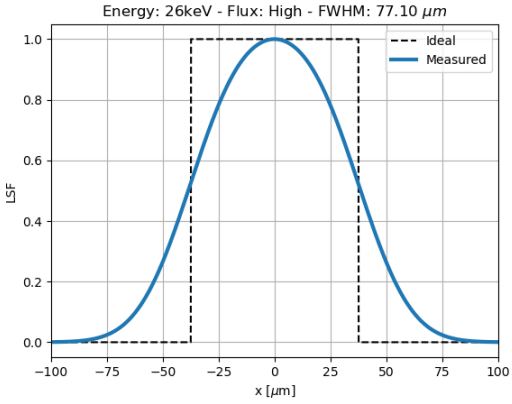

(d)

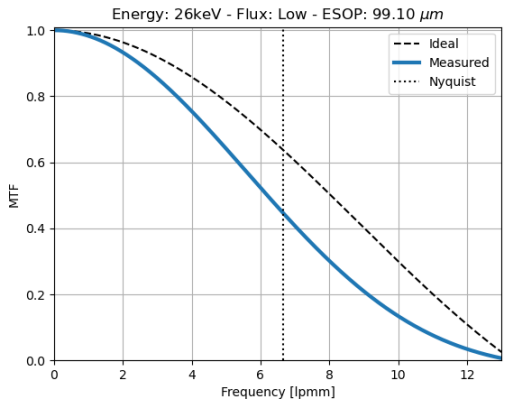

(e)

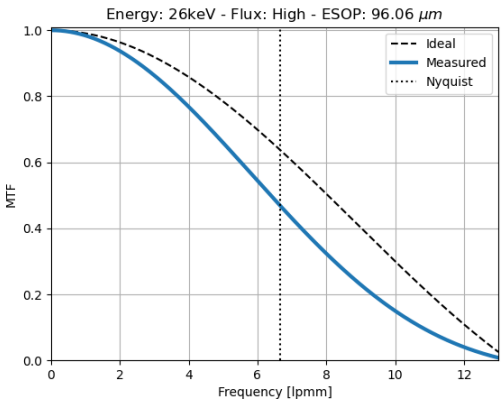

(f)

Figure A.6: Horizontal ESF, LSF and MTF for the energy of 26 keV for the low (A.6a, A.6c, A.6e) and high (A.6b, A.6d, A.6f) flux condition. For each function the measured and the ideal curves are plotted. For the ESF the fitting model is reported while for the MTF plot the Nyquist frequency is highlighted. Fluorescence is not included in the model.

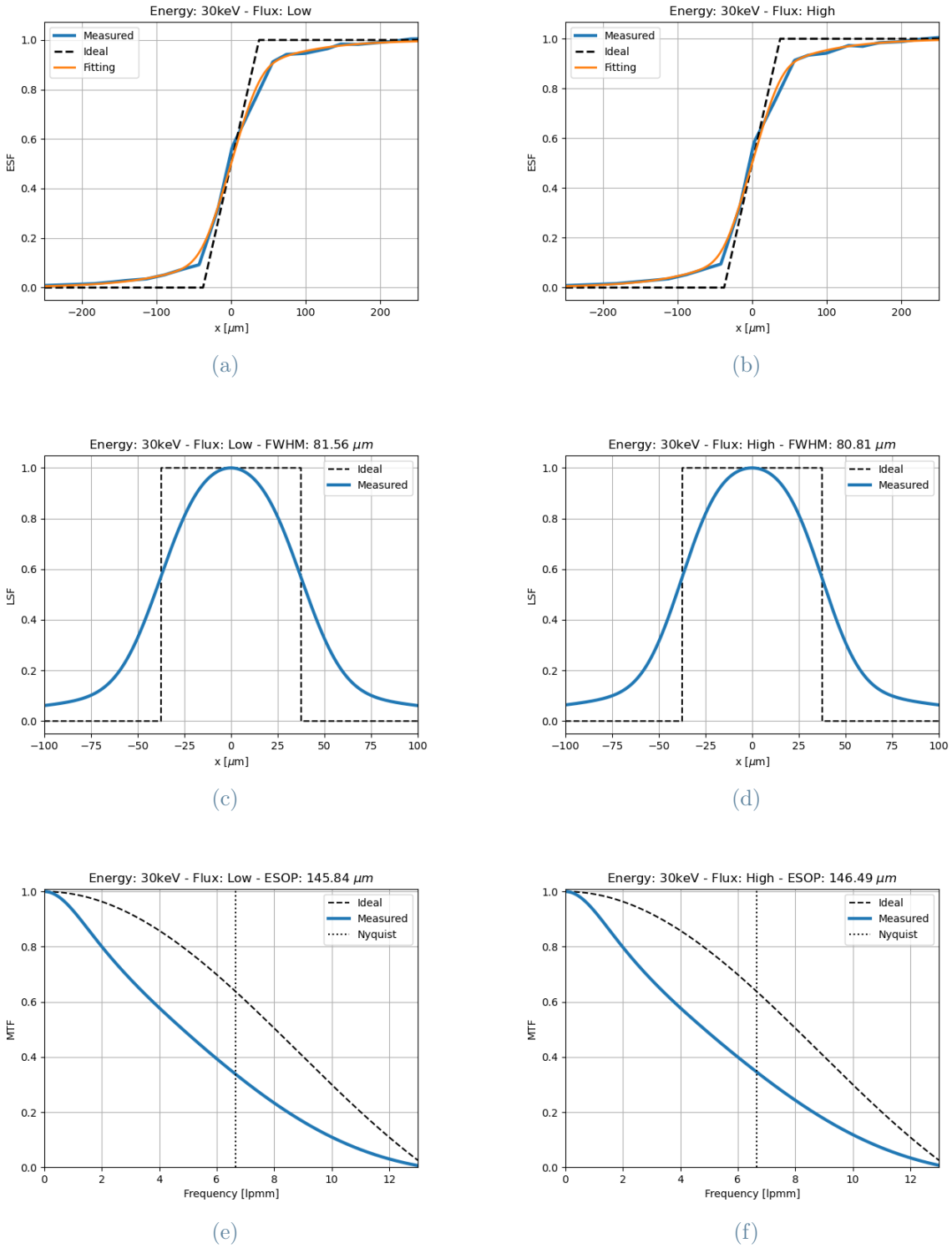

Figure A.7: Horizontal ESF, LSF and MTF for the energy of 30 keV for the low (A.7a, A.7c, A.7e) and high (A.7b, A.7d, A.7f) flux condition. For each function the measured and the ideal curves are plotted. For the ESF the fitting model is reported while for the MTF plot the Nyquist frequency is highlighted. Fluorescence is included in the model.

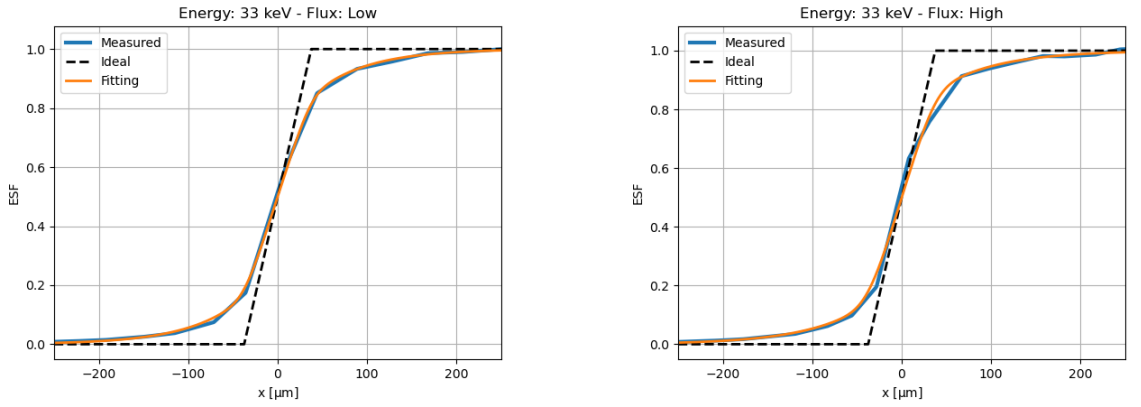

(a)

(b)

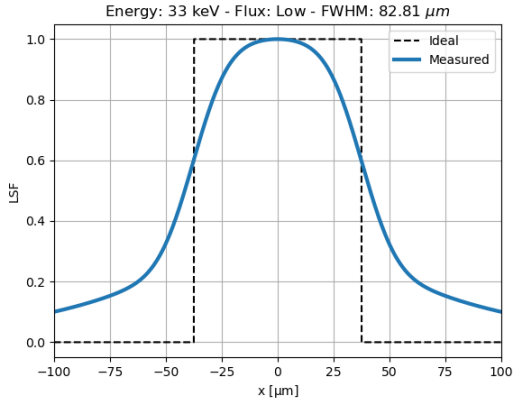

(c)

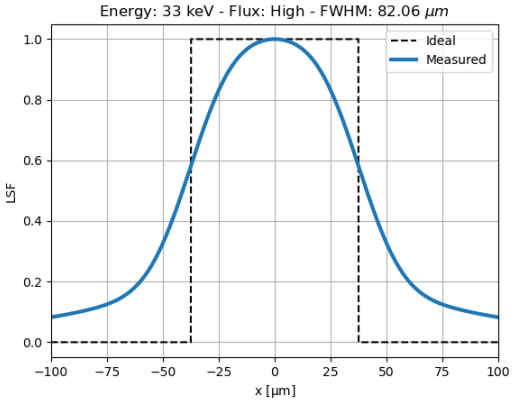

(d)

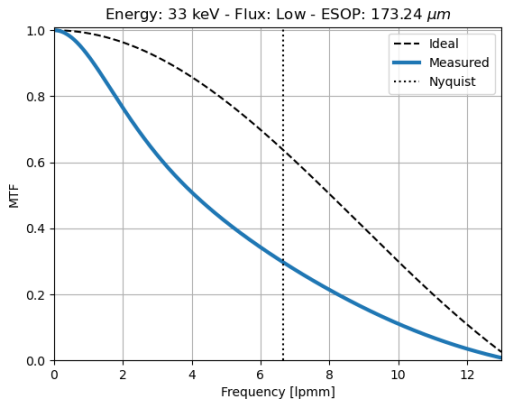

(e)

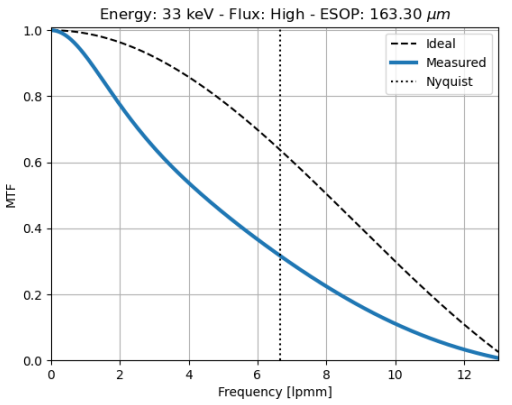

(f)

Figure A.8: Horizontal ESF, LSF and MTF for the energy of 33 keV for the low (A.8a, A.8c, A.8e) and high (A.8b, A.8d, A.8f) flux condition. For each function the measured and the ideal curves are plotted. For the ESF the fitting model is reported while for the MTF plot the Nyquist frequency is highlighted. Fluorescence is included in the model.

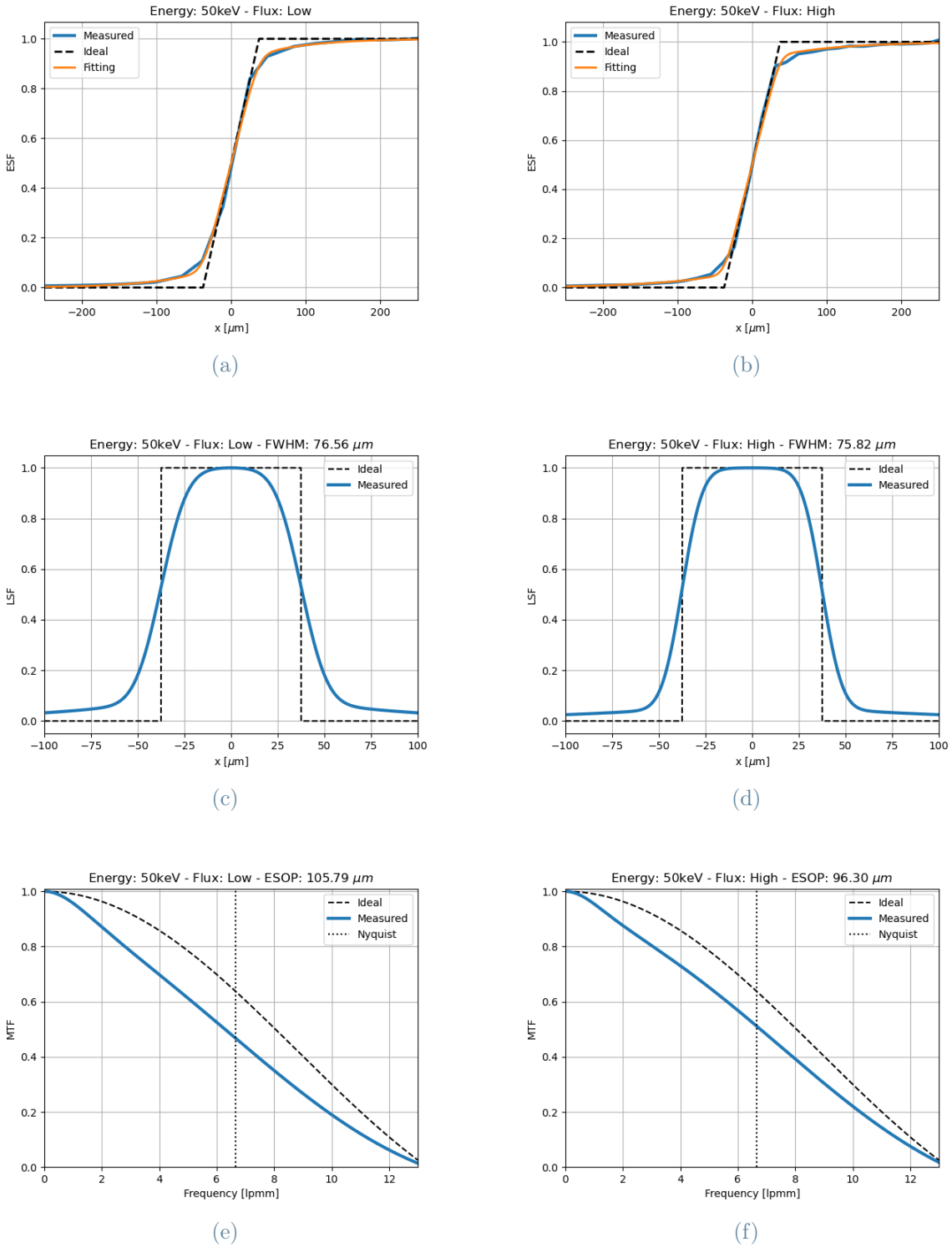

Figure A.9: Horizontal ESF, LSF and MTF for the energy of 50 keV for the low (A.9a, A.9c, A.9e) and high (A.9b, A.9d, A.9f) flux condition. For each function the measured and the ideal curves are plotted. For the ESF the fitting model is reported while for the MTF plot the Nyquist frequency is highlighted. Fluorescence is included in the model.

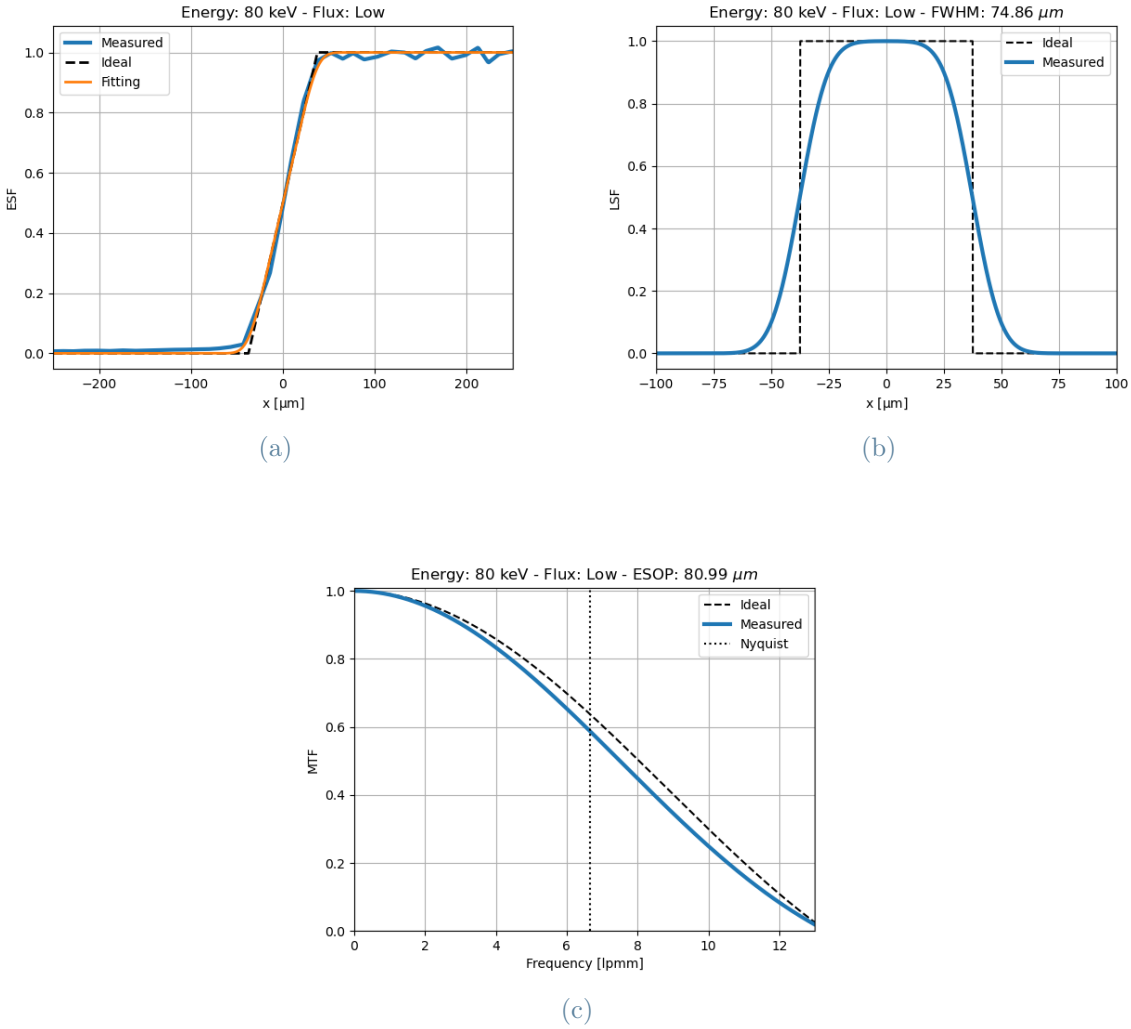

Figure A.10: Horizontal ESF, LSF and MTF for the energy of 80 keV for the low flux condition. For each function the measured and the ideal curves are plotted. For the ESF the fitting model is reported while for the MTF plot the Nyquist frequency is highlighted. Fluorescence is not included in the model.

List of Figures

List of Tables

List of Abbreviations

Abbreviation	Description
1D	One Dimensional
2D	Two Dimensional
Al	Aluminum
API	Application Program Interface
ASIC	Application Specific Integrated Circuits
C	Carbon
CBF	Crystallographic Binary File
CdTe	Cadmium-Telluride
CMOS	Complementary Metal-Oxide-Semiconductor
CMP	CoMParator
CSP	Charge-Sensitive Preamplifier
CT	Computed Tomography
Cu	Copper
DAQ	Data-AcQuisition
DCU	Detector Control Unit
DQE	Detective Quantum Efficiency
EBS	Extremely Brilliant Source
EH	Experimental Hutch
ERF	ERror Function
ESF	Edge Spread Function
ESOP	Equivalent Size Of Pixel
ESRF	European Synchrotron Radiation Facility
FBP	Filtered Back Projection
FFT	Fast Fourier transform

Abbreviation	Description
FWHM	Full Width at Half Maximum
GaAs	Gallium-Arsenide
Ge	Germanium
HPCD	Hybrid Photon Counting Detector
HPD	Hybrid Pixel Detector
HV	High Voltage
IC	Ionization Chamber
ID	Insertion Device
IEC	International Electrotechnical Commission
KES	K-Edge Subtraction Imaging
LIMA	Library for Image Acquisition
LINAC	LINear ACcelerator
LSF	Line Spread Function
MRT	Microbeam Radiation Therapy
MTF	Modulation Transfer Function
NNPS	Normalized Noise Power Spectrum
NPS	Noise Power Spectrum
OH	Optic Hutch
PCD	Photon Counting Detector
PMMA	PoliMethyl MethAcrylate
PSF	Point Spread Function
QE	Quantum Efficiency
ROI	Region Of Interest
Si	Silicon
SNR	Signal-to-Noise Ratio
SR	Synchrotron Radiation
SSRT	Synchrotron Stereotactic Radiation Therapy
URL	Uniform Resource Locator
W	Tungsten

Acknowledgements

It is dutiful and a pleasure for me to thank all who have contributed in different ways to the completion of this Master Thesis, since without their support and encouragement this work would not have been possible.

I firstly wish to express my full gratitude to my supervisor Dr. Luca Fardin; much of this work is due to his teachings and the passion for research he has been able to convey to me by working together. I also thanks him for the patience in correcting my writings.

I would like to acknowledge the European Synchrotron Radiation Facility for the provision of beam time and laboratory facilities.

I thank Dr. Alberto Bravin and Prof. Dr. Carlo Ettore Fiorini very much for rendering this external diploma thesis possible at all.

I would also like to thank Dr. Paolo Busca, of the Detector Group of ESRF, for helping me in the interpretation of the results, for the fruitful discussions and his teachings on detectors and for sharing the ESF fit model.

I would like to thank also the ID17 beamline staff for their support during the experiments: the beamline responsible Dr. Michael Krisch, Dr. Herwig Requardt, Dr. Paolo Pellicioli and Benjamin Restaut.

A special thanks goes to my whole family, whose support has been crucial to the success of this work and to getting to where I am now.

A special thanks goes finally to all my friends who were at my side during these six months.